Stony Brook University

Tailored synthesis and characterization of selective metabolite-detecting nanoprobes for handheld breath analysis

A Dissertation Presented

by

Lisheng Wang

to

The Graduate School

in Partial fulfillment of the

Requirements

for the Degree of

Doctor of Philosophy

In

Materials Science and Engineering

Stony Brook University

December 2008

Stony Brook University

The Graduate School

Lisheng Wang

We, the dissertation committee for the above candidate for the

Doctor of Philosophy degree, hereby recommend

acceptance of this dissertation.

Pelagia-Irene (Perena) Gouma - Dissertation Advisor
Associate Professor, Materials Science and Engineering

Gary Halada - Chairperson of Defense
Professor, Materials Science and Engineering

Albert Tobin
Assistant Professor, Materials Science and Engineering

Milutin Stanacevic
Assistant Professor, Electrical and Computer Engineering

This dissertation is accepted by the Graduate School

Lawrence Martin
Dean of the Graduate School

Abstract of the Dissertation

Tailored synthesis and characterization of selective metabolite-detecting nanoprobes for handheld breath analysis

By

Lisheng Wang

Doctor of Philosophy

In

Materials Science and Engineering

Stony Brook University

2008

The abnormality in the concentration of certain trace gases in human breath, so-called biomarkers, could provide clues to diagnose corresponding diseases. For example, elevated isoprene is a result of cholesterol metabolic disorders, acetone is the biomarker of type-1 diabetes and NO is related to asthma. Non-invasive human breath analysis for disease diagnostics requires selective sensors that respond rapidly and with extreme sensitivity to specific biomarker gases.

On the other side, tungsten trioxide (WO_3) is a very important semiconducting metal oxide which has shown great potential in gas

sensing applications. WO_3 exists in a series of stable solid phases at different temperatures from *α* phase to *ε* phase and an unstable hexagonal phase (*h*-WO_3). However, except extensively studied *γ*-WO_3, the properties of other phases are still not fully known, esp. *ε*-WO_3 and *h*-WO3 whose structures are different from other phases.

This dissertation discusses the development of several selective biomarker sensors based on room temperature (RT) stable *ε*-WO_3 and *h*-WO_3 nanostructured materials.

Ferroelectric *ε*-WO_3 nanoparticles were synthesized using the flame spray pyrolysis method. Although the *ε*-WO_3 polymorph vanishes during heat treatment in pure WO_3 products, chromium dopants were utilized to stabilize this phase. The resistive sensor based on 10at%Cr doped *ε*-WO_3 nanoparticles was found to be very sensitive and selective to low concentrations of acetone (0.2-1ppm) compared to a series of interfering gases at 400°C. The proposed explanation for the materials selectivity to acetone is the likely interaction between the surface dipole of ferroelectric *ε*-WO3 nanoparticles and the highly polar acetone gas molecules.

Open structured *h*-WO_3 nanoparticles were produced by acid precipitation method. It was found that *h*-WO_3 is very sensitive to NO_x compared to other gases at 150 °C due to the open tunnel structure of *h*-WO_3. Such selectivity is lost at 350°C. Instead, the material is very

sensitive and selective to isoprene gas at 350°C. A p-n transition was found when the working temperature of the sensor increased from RT to 350 °C which could be related to the excessive surface oxygen of the product.

Finally, a handheld exhaled breath analyzer prototype has been developed for non-invasive disease diagnosis. Real-time monitoring of the gas concentration is demonstrated, making this invention a revolutionary, non-invasive, diabetes diagnostic tool.

Table of Contents

List of Symbols and Abbreviations

VOC: Volatile Organic Compound

GC-MS: Gas chromatograph mass spectrometry

SIFT-MS: Selected ion flow tube mass spectrometry

QCM: Quartz crystal microbalance

CL: Chemiluminescence

1D: One-dimensional

FSP: Flame-spray pyrolysis

XRD: X-ray diffraction

SEM: Scanning electron microscopy

EDS: Energy dispersive spectrum

TEM: Transmission electron microscopy

SAED: Selected-area electron diffraction

HRTEM: High-resolution transmission electron microscopy

BET: Brunauer-Emmett-Teller

SA: Surface area

XPS: X-ray photoelectron spectroscopy

TGA: Thermo Gravimetric Analysis

DTA: Differential Thermal Analysis (DTA)

DSC: Differential Scanning Calorimetry

RT: Room temperature

JCPDS- Joint Committee on Powder Diffraction Standards

LED: Light emitting diode

TO: Transistor outline

E_C: Conduction band edge

E_V: Valence band edge

E_F: Fermi energy level

E_t: Surface state energy

χ: electron affinity

E_{C0}: Conduction band edge before charge transfer from the surface states

E_{V0}: Valence band edge before charge transfer from the surface states

E_{F0}: Fermi energy level before charge transfer from the surface states

L_D: Debye length

d_{BET}: BET equivalent average diameter

R_0: Baseline resistance

R_g: Gas-responding resistance.

S: Sensitivity

List of Figures

List of Tables

Acknowledgements

I would like to express my most sincere gratitude to my supervisor, Prof. P.I. Gouma. She has been providing great guidance and support throughout the whole period of my Ph.D. study in all aspects. Her enthusiasm, her inspiration as well as her deep thinking have been of great value for me. Her encouragement, her good teaching and her sound advice have enabled me to carry on the research smoothly and rewardingly. With her support, I had numerous opportunities to present my work in conferences or visit other research groups, which benefit me a lot.

Many thanks to Prof. Milutin Stanacevic and his student Xiao Yun, for their great help during the collaborated research. The electronic circuit of the breath analyzer was developed by his group based on our design and specifications. Prof. Stanacevic and Xiao also provided important technical supports during the follow-up utilization of the device.

I am very grateful to Prof. Albert Tobin He was instructor of my two courses and one of the best teachers that I have ever seen. In addition, as my preliminary examination and defense committee member, his valuable insights played a very important role in solidifying my research focus. I would also like to thank Prof. Gary Halada for serving on my defense committee chair.

Special thanks to Dr. Judit Pfeifer and Dr. Csaba Balazsi (Research Institute for Technical Physics and Materials Science, the Hungarian Academy of Sciences) for many fruitful discussions during the collaboration and being very friendly hosts during my visit in Hungary. I also deeply appreciate the enlightening guidance from Prof. Sotiris E. Pratsinis (Particle Technology Laboratory, Swiss Federal Institute of Technology Zürich) as the supervisor during my three months' stay in his group, as well as the great help from his students, esp. Dr. Alexandra Teleki, who taught me everything there.

I spent a wonderful life during my Ph.D. study in USA. Appreciation is expressed to Krithika Kalyanasundaram, Smita Gadre, Aisha Bishop, Koushik Ramachandran, Ruipeng Xue for being wonderful labmates and great mentors in Rooms 201 and 203 in Old Engineering.

Finally, I would like to address my deepest gratitude to my beloved parents, my sisters and my dear fiancée for their continuous support and love throughout my study.

I acknowledge the support provided by the National Science Foundation through an NSF-NIRT grant (DMR-0304169).

Vita, Publications and Field of Study

EDUCATION

1. Ph.D., Materials Sci. Eng., SUNY Stony Brook, New York, USA. 2008.12

2. M. Eng., Materials Sci. Eng., Tsinghua Univ., Beijing, China, 2005.7

3. B. Eng., Materials Sci. Eng., Tsinghua Univ., Beijing, China, 2003.7

SELECTED PUBLICATIONS

1. **L. Wang**, A. Teleki, S.E. Pratsinis, P.I. Gouma, Ferroelectric WO_3 nanoparticles for acetone selective detection, Chemistry of Materials, 20(15), 2008: 4794-4796.

2. I.M. Szilágyi, **L. Wang**, *et al.*, Preparation of hexagonal WO_3 from hexagonal ammonium tungsten bronze for sensing NH_3, Materials Research Bulletin, 2008, doi:10.1016/j.materresbull.2008.08.003.

3. C. Balazsi, **L. Wang**, *et al.*, Nanosize hexagonal tungsten oxide for gas sensing applications, Journal of the European Ceramic Society, 28(5), 2008: 913-917.

4. **L. Wang**, J. Pfeifer, C. Balazsi, I.M. Szilágyi, P.I. Gouma, Nanostructured hexagonal tungsten oxides for ammonia sensing, Proceedings of SPIE, 6769, 2007: 67690E

5. **L. Wang**, J. Pfeifer, C. Balazsi, P.I. Gouma, Synthesis and sensing property of metastable hexagonal WO_3 nanopowders, Materials and Manufacturing Processes, 22(6), 2007: 773-776.

6. **L. Wang**, X. Zhang, *et al.*, Synthesis of well-aligned ZnO nanowires by simple physical vapor deposition on c-oriented ZnO thin films without catalysts or additives, Applied Physics Letters, 86(2), 2005: 024108.

7. **L. Wang**, X. Zhang, X. Liao, W. Yang, A simple method to synthesize single-crystalline Zn_2SnO_4 (ZTO) nanowires and their photoluminescence properties, NANOTECHNOLOGY, 16(12), 2005: 2928-2931

8. Y. Zhang, **L. Wang**, *et al.*, Synthesis of nano/micro zinc oxide rods and arrays by thermal evaporation approach on cylindrical shape substrate, Journal of Physical Chemistry B, 109(27), 2005: 13091-13093.

9. X. Zhang, **L. Wang**, G. Zhou, Synthesis of well-aligned ZnO nanowires without catalysts, Reviews on Advanced Materials Science, 10(1), 2005: 69-72.

10. **L. Wang**, X. Zhang *et al.*, Synthesis of well-aligned ZnO nanowires using simple physical vapor deposition without catalysts or additives, MRS Proceedings, 879E, 2005: Z3.21

11. **L. Wang**, X. Zhang, F. Zeng, Synthesis and characterization of ZnO nanowires using a simple PVD approach without catalysts, Materials Science Forum, 475-479(1-5), 2004: 3535-3538.

AWARDS AND HONORS

1. Presidential Fellowship, Stony Brook Univ., 2005 – 2006

2. Outstanding Thesis for Masters' Degree, Tsinghua Univ., 2005

3. Friends Scholarship, Tsinghua Univ., 1999 – 2000, 2000 – 2001, 2001 – 2002, 2003 – 2004

CHAPTER 1 Introduction

1.1 Biomarkers in human breath

Breathing is one of the most common and the most important functions of human organisms. Most simply speaking, Breathing takes oxygen in and carbon dioxide out of the body. However, this does not reflect the complexity of human breath at all. Our exhaled breath is a mixture of N_2, O_2 CO_2, H_2O, inert gases and thousands of other trace gases. These gases include inorganic molecules such as NO, NH_3 or CO and volatile organic compounds (VOCs) such as acetone, methanol or isoprene, with concentrations ranging from ppb to ppm. The composition of breath varies a lot from person to person, both qualitatively and quantitatively, particularly for those trace gases. Generally speaking, common VOCs are products of core metabolic processes while inorganic molecules are related to health conditions and can reflect a potential disease of the individual or a recent exposure to a drug or an environmental pollutant. Therefore, the abnormality in the concentration of certain trace gases, so-called biomarkers, could provide clues to diagnose corresponding diseases.

In spite of a most advance technology, breath testing for disease diagnosis could date back to at least two thousand years ago. Ancient Greeks physicians already knew the odor of a patient's breath is associated with some diseases.[1] For example, the sweet smell of acetone in breath accompanies uncontrolled diabetes, a fishy smell is a result of liver disease, a urine-like smell is related to kidney failure and the putrid stench results from a lung abscess. Modern breath

analysis started in the 1970s when Pauling *et al.* determined more than 200 components in human breath using gas chromatography.[2] [3]. During the next 30 years, more and more biomarkers were identified and separated. Table 1-1 shows some samples of biomarkers and their related diseases. Some types of human breath tests have successfully applied in clinic diagnosis. The values listed in the table come from healthy human bodies. The concentrations of certain biomarkers exceed these values in patients' exhaled breath.

Table 1-1 Examples of biomarkers and their respective physiological concentration ranges in the human breath as measured by other workers [4, 5].

Biomarkers	**Physiological origin**	**Related diseases**	**Physiological ranges in human breath**
Ethane	Lipid peroxidation	Oxidative stress	1-11 ppb
Pentane	Lipid peroxidation	Oxidative stress	Less than ethane
Isoprene	Cholesterol biosynthesis	Cholesterol metabolic disorder	55-121 ppb; 12-580 ppb;
Acetone	Decarboxylation of acetoacetate and acetyl-CoA	Diabetes mellitus, ketonemia	293-870 ppb; 1.2-1880 ppb
Ethanol	Alcohol ingestion	Alcohol poisoning	27-153 ppb; 13-1000 ppb
Methanol	Degradation of natural pectin from plants; ingestion	Methanol intoxication	160-2000 ppb
NH_3	Metabolic product of amino acid deamination	Uremia, kidney impairment	422-2389 ppb; 200-1750 ppb
CO	Inhalation from In-complete burning of carbon containing fuels, e.g. smoking	Lung diseases	<6 ppm
NO	L-arginine oxidation	Asthma, lung diseases	1-9 ppb, lower respiratory; 0.2-1 ppm upper respiratory; 1-30 ppm, nasal level.

The following sections will introduce several well-known biomarkers and discuss their origins in our human bodies.

1.1.1 Acetone

Acetone (also known as propanone, $(CH_3)_2C=O$) is one of the most abundant VOCs in human exhaled air.

Generally speaking, acetone is produced by hepatocytes via decarboxylation of excess Acetyl–CoA (Figure 1-1) [3], which comes from fatty acid *β*-oxidation. In detail, it is formed by decarboxylation of acetoacetate, which derives from lipolysis or lipid peroxidation. Ketone bodies like acetone are oxidized via the Krebs cycle in peripheral tissue. Ketone bodies in blood (including acetoacetate and hhydroxybutyrate) are increased in ketonemic subjects in times of fasting or starving or during diet.

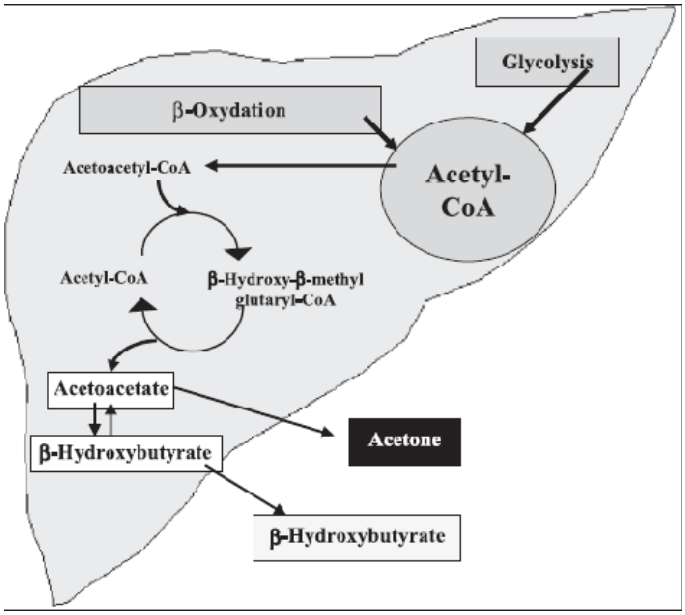

Figure 1-1 Generation of ketone bodies via decarboxylation of acetyl-CoA.*

In patients with diabetes, the combination of insulin deficiency and counterregulatory hormone increase accelerates the movement of free fatty acids in adipose tissues. As a result, intrahepatic metabolism in the body shifts from fat

* Reprinted from Clinica Chimica Acta, 2004, 347(1-2): p. 25-39, copyright 2004, with permission from Elsevier.

synthesis to fat oxidation and ketogenesis. Excessive ketone body acetoacetates are spontaneously decarboxylated to form acetone [6]. The ‘sweet odor’ of the breath of ketotic individuals is due to acetone. The average concentration of acetone in the breath from a healthy human body is believed to be lower than 0.8ppm while that from a diabetic patient is higher than 1.8ppm [7]. Therefore, acetone has been widely accepted as the biomarker of type-1 diabetes.

1.1.2 Isoprene

Isoprene formally called 2-methylbuta-1,3-diene, (CH_2=C(CH_3)-CH=CH_2) is an important biological material. Although more than 1,000 kinds of VOCs have been found in human breath, only a few exist in all human bodies. Among them, isoprene is the most common one, which is always present as a precursor of many important organic compounds during the metabolic process. The estimated production rate of isoprene in the human body is .15 μmol/kg/h, equivalent to approximately 17 mg/day for a 70 kg person. This value is time and age dependent. In a whole day, the maximum concentration appears at 6am while the minimum at 6pm [3]. In a whole life, isoprene concentration is significantly lower in children and it increases up to 25 years old [5].

Most isoprene is formed along the mevalonic pathway of cholesterol synthesis (Figure 1-2) [3, 5]. The formation of mevalonate from acetic acid is a very important step during cholesterol biosynthesis, catalyzed by hydroxymethylglutaryl (HMG)–CoA. Mevalonate is then converted in the cytosol to isopentenyl pyrophospate, undergoing isomerization to dimethylallyl pyrophosphate (DMPP), which finally converts to isoprene.

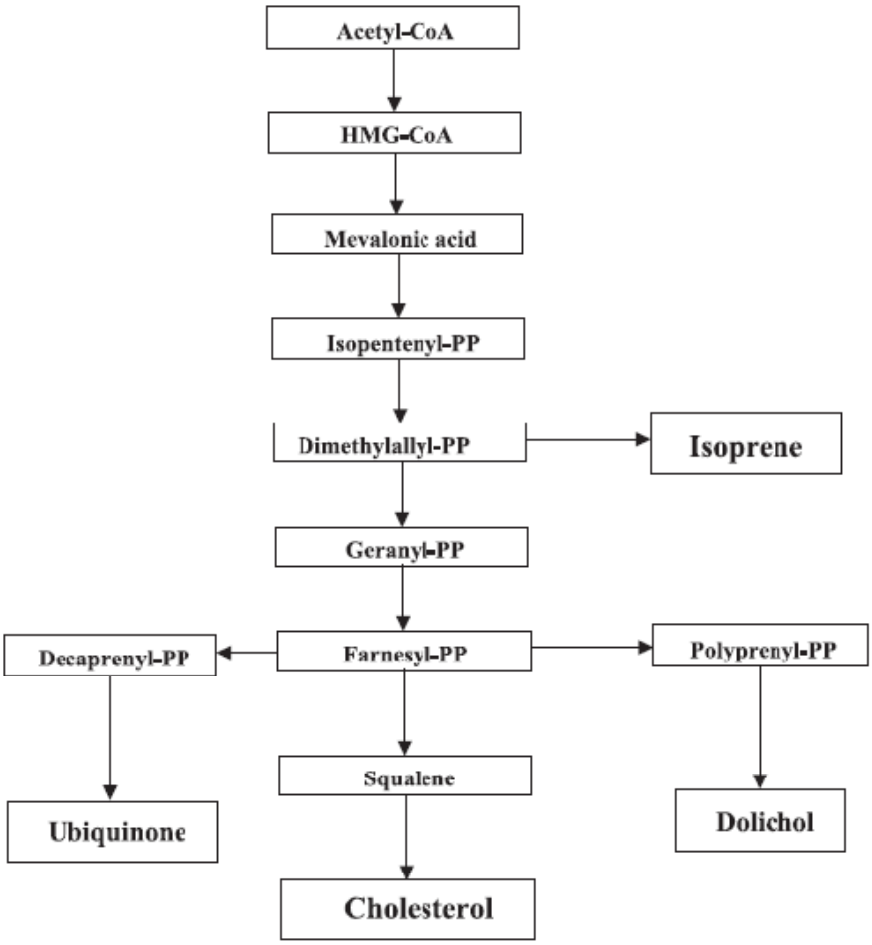

Figure 1-2 Biochemical pathway of isoprene generation.*

In rat liver cytosol, this step is rapidly accomplished via an acid-catalyzed elimination reaction; while in certain plants, this reaction is catalyzed an enzyme containing Mg^{2+}. In mammalian tissue, evidence shows that a similar enzyme, Mg^{2+}-dependent isopentenyl pyrophosphate isomerase, may play the same role. It catalyzes the interconversion of isopentenyl pyrophosphate and DMPP.

In this way, isoprene has been identified as biomarker of cholesterol metabolic disorders such as hypercholesterolemia.

* Reprinted from Clinica Chimica Acta, 2004, 347(1-2): p. 25-39, copyright 2004, with permission from Elsevier.

1.1.3 Nitric oxide

Different from isoprene and acetone, nitric oxide is a kind of inorganic gases with small molecules and simple structure (N=O). In fact, nitric oxide is one of the smallest known biologically active messenger molecules. In spite of an evanescent gas, which is rapidly oxidized into NO_2, nitrites and nitrates by O_2, it is fairly stable at low concentrations, even O_2 is present [8].

The oxidation of L-arginine to L-citrulline yields NO as a byproduct, which is the origin of NO in human bodies. Such reaction is catalyzed by enzymes called NO synthase (NOS). (Figure 1-3) Three isoforms of NOS exist, with constitutively expressed nNOS (NOS1), eNOS (NOS3) and inducibly expressed iNOS (NOS2) [9]. nNOS and eNOS produce small picomolar concentrations of NO, are steroid resistant, and are thought to play a role in the regulation of respiratory function.

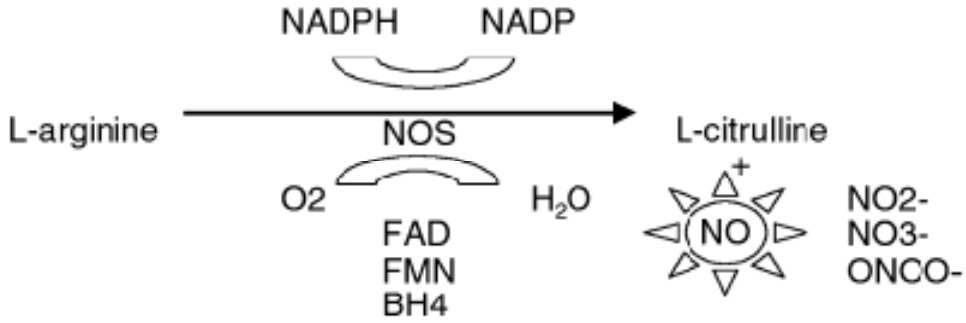

Figure 1-3 Synthesis of nitric oxide (NO) from L–arginine. *

In contrast, inducible iNOS produces nanomolar concentrations of NO and is steroid sensitive. iNOS is also believed to be responsible for the high levels of NO concentration measured in the expired breath of patients with asthma, and is involved with airway inflammation. iNOS is expressed in airway epithelium,

* Reprinted by permission from Macmillan Publishers Ltd: Immunology and Cell Biology, 2001, 79(2): p. 178-190. Copyright 2001.

airway and vascular smooth muscle, macrophages, and mononuclear cells [9].

Asthma is a chronic inflammatory disorder of the airways that produces airway hyperresponsiveness, reversible airway obstruction, and symptoms such as wheezing, cough, and shortness of breath. An increase in exhaled NO is not specific for asthma, but an increased concentration may be useful in differentiating asthma from other causes of chronic cough [4]. The diagnostic value of exhaled NO measurements to differentiate between healthy persons with or without respiratory symptoms and patients with confirmed asthma has been analyzed by Dupont *et al.* showing that >16 ppb of NO in lower respiratory tract could be treated as a cutoff for asthma with a 90% specificity and 90% positive predictive value [10]. This suggests that a simple and non-invasive measurement of exhaled NO is good candidate for asthma diagnosis.

1.2 Current techniques for breath analysis

Since it is a non-invasive technology and easy to comprehend and operate, esp. for those patients who needs everyday monitoring and controls, breath analysis has great application potentials for human disease diagnosis. Therefore, it has been paid more and more attention to in recent years.

We already know there are more than 1,000 trace gases in human breath and the concentrations of most gases are on ppb-ppm levels, including those labeled as “biomarkers”. To satisfy diagnostic requirements, any kind of breath analysis should be sensitive, which means down to ppm or sub ppm concentration levels of a certain biomarker are able to be detected, and selective, which means other interfering gas molecules won’t influence the detection.

Different techniques and methods have been developed to measure the concentrations of specific biomarkers in human exhaled breath. In general, they can be classified into two groups. This section will have a brief review on these techniques.

1.2.1 Spectrometry/spectroscopy-based techniques

Gas chromatograph mass spectrometry (GC-MS) is a technique that combines both gas chromatographs (GC) and mass spectrometers (MS) to accurately identify different substance in a single sample (shown in Figure 1-4).

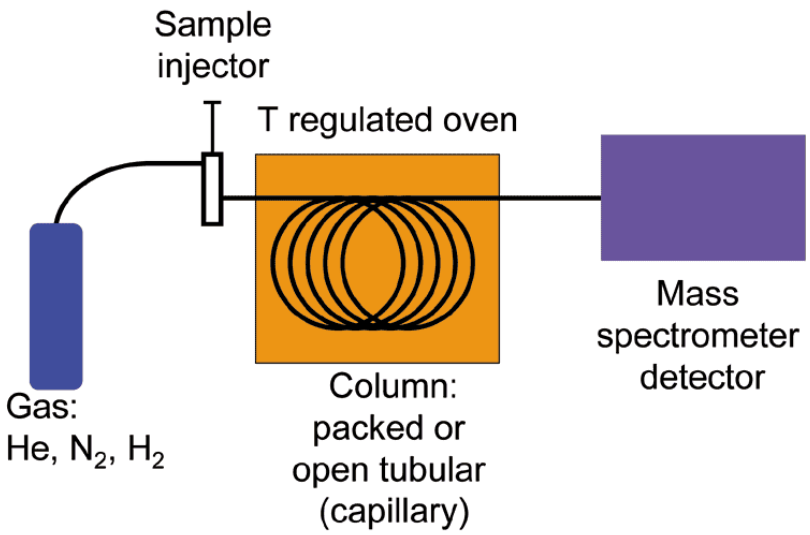

Figure 1-4 Schematic illustration of GC-MS technique.

In gas chromatograph, first of all, the sample is injected onto the head of the chromatographic capillary column and then transported through the column by the flow of inert, gaseous mobile phase. Different molecules in the sample separate in this period according to their respective properties (boiling points, polarity, etc), and then come out asynchronously, captured by an MS detector downstream. This detector quantitatively analyzes these molecules by breaking

each one into ionized fragments and detecting these fragments using their mass to charge ratio. The combination of GC and MS enables a much finer degree of substance identification than either unit used separately. Therefore, GC-MS is currently the standard technique for determining the composition of VOCs in breath [11]. For example, Leone *et al.* [12] confirmed the existence of NO and Deng *et al.* [7] determined the concentration of acetone in human breath.

Selected ion flow tube mass spectrometry (SIFT-MS) is a new analytical technique for real-time quantification of several trace gases simultaneously in air and breath [13]. It relies on chemical ionization of the trace gas molecules in air/breath samples introduced into helium carrier gas using H_3O^+, NO^+, and $O_2^{+\cdot}$ precursor ions. Reactions between the precursor ions and trace gas molecules proceed for an accurately defined time, the precursor and product ions being detected and counted by a downstream mass spectrometer, thus effecting quantification. Absolute concentrations of trace gases in single breath exhalation can be determined by SIFT-MS down to ppb levels, obviating sample collection and calibration [13]. By utilizing this technique, Spanel *et al.* [14] studied the isoprene levels in the breath for 29 healthy volunteers in 6 months. Diskin *et al.* [15] investigated time variation in concentration of several biomarkers including acetone, isoprene, ammonia and ethanol etc.

Optical absorption spectroscopy systems for gas analysis have created new opportunities in recent years, while the increased sensitivity available with modulation techniques offers particular potential for trace species measurement [16]. Compared to previously discussed techniques, this kind of method offers

much faster evaluation of samples with advantage of real-time use. In addition, its detection limit is significantly low, down to ppb-ppt levels. For example, Roller *et al.* [17, 18] used a high-resolution mid-IR tunable-laser absorption spectroscopy system with a single IV–VI laser measure exhaled nitric oxide and carbon dioxide (CO_2) simultaneously in human breath over a single exhalation. The detection limit for NO was estimated to be 1.5 ppb for a 4-second integration time. Moreover, simultaneous CO_2 measurement provides an internal calibration parameter that accounts for any variation in flow.

Other spectroscopy or spectrometry-based techniques include proton transfer reaction mass spectrometry (PTR-MS) [19], gas chromatograph ion mobility spectrometry (GC-IMS) [20] and cavity ringdown spectroscopy [21] etc.

In general, the above techniques are able to provide very accurate (down to ppb levels) and selective detections on target biomarkers in our human breath. However, their disadvantages are also obvious: the equipments are bulky and quite expensive. In addition, most of the measurements and/or subsequent data analyses are time-consuming.

1.2.2 Chemical sensors

To overcome the disadvantages mentioned above, different kinds of chemical sensors have been introduced during the last two decades. These sensors are based on the reactions between the gas molecules and the sensor surfaces.

A quartz crystal microbalance (QCM) measures a mass per unit area by measuring the change in frequency of a quartz crystal resonator. ($\Delta f \propto K\Delta m$) [22]

The resonance is disturbed by the addition or removal of a small mass due to oxide growth/decay or film deposition at the surface of the acoustic resonator. Therefore, by coating a thin film on the quartz which has specific attachment or reaction with target molecules, we can achieve a successful detection on those gas molecules. Huang *et al.* [23] invented a quartz crystal microbalance sensor modified with Ag^{+}-ZSM-5 zeolite for diabetes diagnosis. The Ag^{+}-ZSM-5 zeolite has nanometer cavities whose average diameter (5.0 Å) is very close to the molecular size of acetone (4.4Å). They are able to trap acetone which leads an especially good sensitivity (260 ppb) and selectivity to this VOC. Palaniappan *et al.* reported NO selective detection by coating either hemoprotein/silica hybrid films [24] or phthalocyanine/silica hybrid films [25].

Chemiluminescence (CL) is defined as the emission of electromagnetic radiation (usually in the visible or near-infrared region) produced by a chemical reaction that generally yields one of the reaction products in an electronic excited state producing light on falling to the ground state. A CL sensor is based on the CL resulting from the interaction between gases and solid surfaces. Nakagawa *et al.* observed this phenomenon during the catalytic oxidation of organic vapors on α-Al_2O_3 [26] and Dy^{3+}-activated α-Al_2O_3 [27]. Zhu *et al.* [28] studied CL emission by organic vapors (acetone and ethanol) on several kinds of metal oxide nanosized materials, esp. TiO_2. The different organic vapors can be discriminated from the different CL responses in the presence of the different materials. Recently, Ohira *et al.* [29] applied this method for human breath isoprene determination with high sensitivity, with the limit of detection to 0.6 ppb,

by detecting its CL reaction with ozone.

Another large group of chemical sensors is chemo-resistive sensor, which will be discussed in detail during the next section.

It has been widely believed that chemical sensors are able to provide fast, real-time detection on the analyte. Their sensitivities are also promising. Besides, chemical sensors have great potential to manufacture relatively small devices for daily use. The cost of such devices is also considered not high. However, lack of selectivity becomes their most significant drawback. One solution is to introduce the concept of “electronic nose”, which is composed of a series of nonselective gas sensors coupled with a pattern recognition technique. [30] However, this increases the complexity of the sensing system dramatically. Another possible solution is to discover appropriate materials for selective detection to specific biomarkers, which is the main focus in this dissertation.

1.3 Chemo-resistive gas sensors

The word “sensor” is derived from Latin “sēnsus”, which means the faculty of perceiving. Although sensors are very commonly used in our daily life, the definition is nevertheless ambiguous. Generally speaking, a sensor is a device which receives a signal or stimulus from its surrounding, responds to it and converts it into an electronic signal of some kind in a distinctive manner that can be recognized by human beings.

According to this definition, a sensor is typically composed of three parts: the input, the output and the converting mechanism. Hence, there are several ways to classify sensors. The most common classification is based on the input

signal, including the following different types (shown in Table 1-2).

Table 1-2 Different types of sensors classified by input signals.

Type	Input signals	Examples
Thermal	temperature, heat	thermometer, calorimeter
Electro	resistance, current, voltage, power	multimeter, watt-hour meter
Magnetic	magnetism	compass, metal detector, radar
Mechanical	pressure, gas/liquid flow, strain	barometer, flow meter, strain gauge
Chemical	specific chemicals (e.g. gas, ions)	PH electrode, oxygen sensor
Optical	light wave	photodiode, UV radiation detector
Acoustic	Sound wave	microphone, sonar

In particular, a gas sensor, which belongs to chemical sensors, detects the existence and concentration of a specific gas or a class of gases. One of the most common gas sensors uses resistance as output signals, which is called chemo-resistive gas sensors.

1.3.1 Evaluation of sensors

To evaluate the performance of a sensor, at least four parameters are usually mentioned, namely:

- Sensitivity
- Selectivity
- Stability
- Response and recovery time

Sensitivity can be defined as the magnitude of response of a sensor to a particular target analyte. Depending on different applications, there are mainly two mathematical definitions that can be used. Assuming R_0 and R_g are the intensities of output signals (i.e. resistance for gas sensors) before and after the exposure of input signals respectively, and S represents sensitivity, the first and

most commonly used definition, which is called relative sensitivity, is:

$$S = \frac{\Delta R}{R_0} = \frac{R_g - R_0}{R_0} \tag{1}$$

The other normalized definition is shown below:

$$S = \frac{R_g}{R_0} \text{ when } R_g > R_0 \text{ or } S = \frac{R_0}{R_g} \text{ when } R_g < R_0 \tag{2}$$

This definition is particularly useful when we want to compare the sensitivities of positive and negative responses together and will be adopted in this dissertation.

Selectivity refers to the ability to distinguish one specific input signal among interfering signals, i.e. a particular gas in a mixture of several gases for gas sensors. Selectivity is a fundamental issue in the gas sensor design.

Stability is talking about the long term operation of a sensor without any change of other parameters. For example, an NH_3 sensor should show the same resistance responding to a certain concentration of NH_3 at any time. Stability is of great importance for a sensor in use.

An ideal sensor should respond to the input signal immediately and recover to its base state once the input is withdrawn. However, in practice, it always takes some time for the sensor to go to the final response value or to the baseline, which is defined as response time and recovery time, respectively. To accurately determine these two terms, we can take the length of period in which the output value of the sensor goes from R_0 to $10\%R_0+90\%R_g$ as response time and, similarly, the output value goes from R_g to $10\%R_g+90\%R_0$ as response time.

1.3.2 Working mechanism of resistive gas sensors

Resistive gas sensors based on semiconducting metal oxides are actually one of the most investigated groups of gas sensors. They have attracted the attention of many users and scientists interested in gas sensing under atmospheric conditions due to the: low cost and flexibility, simplicity of their use and large number of detectable gases etc. The first reported work in this area dated back to 1957, in which Bielanski *et al.* [31] showed the electrical conductivity change of several semiconducting metal oxides, including *n*-type ZnO, and *p*-type NiO etc., when they were exposed to ethanol. In 1962, Seiyama *et al.* [32] used ZnO thin films to detect several kinds of gases and VOCs, including toluene, benzene and CO_2 etc. The decisive step was taken when Taguchi brought sensors based on semiconducting metal oxides to an industrial product (Taguchi-type sensors). Nowadays, there are many companies offering this type of sensors, such as Figaro, FIS, MICS, UST, CityTech, Applied-Sensors, NewCosmos, etc. Their applications span from “simple” explosive or toxic gases alarms to air intake control in cars to components in complex chemical sensor systems. On the scientific research side, there have been numerous publications during the half century talking about new detection systems, improved sensing properties, influence of various parameters and so on.

Despite the diversity mentioned above, the basic working mechanism remains the same. Generally speaking, if the sensor is surrounded by a certain kind of oxidizing or reducing gas, the gas tends to extract electrons from the sensor or provide electrons to the sensor, thus changing the density of the charge carriers which finally leads to the resistance change. In detail, let’s

consider an *n*-type semiconductor whose major charge carriers are electrons. When it is exposed to atmosphere, the atmosphere contains O_2 which is a kind of oxidizing gas; it adsorbs electrons from the surface of the material to form O^-. The reaction formula is shown below:

$$O_2 + 2e^- \rightarrow 2O^- \tag{3}$$

Obviously, this reaction consumes electrons, therefore increasing the resistance of the material. If a fraction of H_2 is added into the atmosphere, which belongs to reducing gas, the following reaction occurs:

$$H_2 + O^- \rightarrow H_2O + e^- \tag{4}$$

Hence, the density of electrons increases, accompanied by the decrease of resistance. Otherwise, if some oxidizing gas, such as NO_2, is added, the resistance will increase.

Let's take a further step to consider the energy band change during the interaction between the surrounding gas and the material. As we know, the band structure of a semiconductor is composed of a valence band whose top energy is E_{V0} and a conduction band whose bottom energy is E_{C0} (shown in Figure 1-5). There exists a gap between them in which the Fermi energy level E_{F0} is located. The Fermi energy refers to the highest energy state that electrons can occupy at 0K and also means the energy state in which the probability to be occupied by an electron is ½ above 0K. This probability, called Fermi distribution function, decreases exponentially as the increase of energy level. Both conduction band and valence band are flat before interaction at the surface occurs.

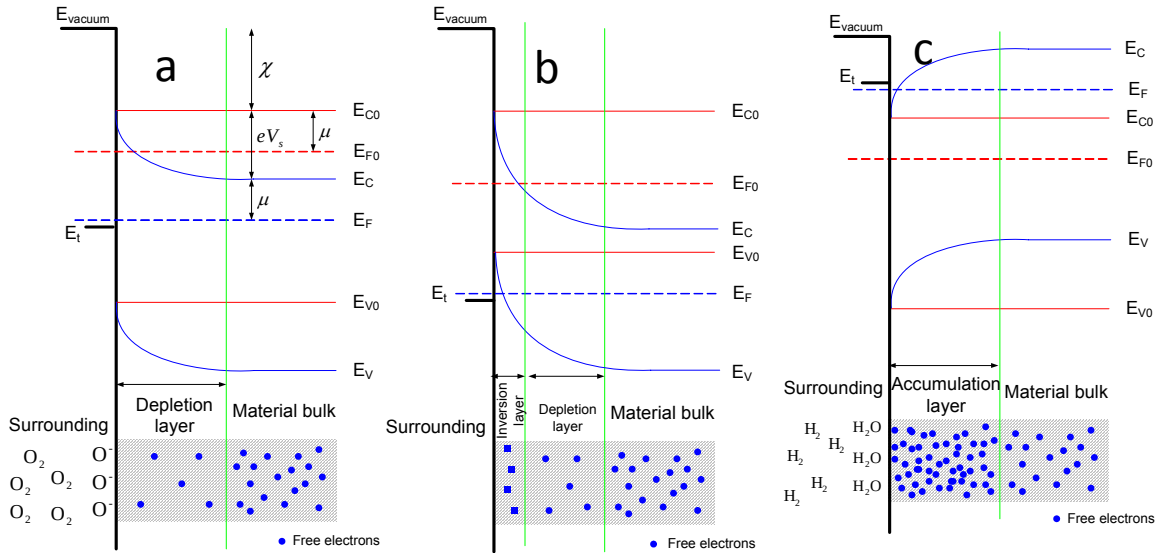

Figure 1-5 A model illustrating the formation of band bending in an n-type sensor surrounded by (a) oxidizing gas; (b) strong oxidizing gas; and (c) reducing gas.

When we place the *n*-type sensor in the air, the surface metal ions will adsorb oxygen atoms and create a surface state. As long as the surface state has a high density, a deep energy level forms, which is E_t in Figure 1-5. Since oxygen is an oxidizing gas, tending to receive electrons from outside, this energy is lower than E_{F0}. Obviously, before charge transfer, E_t level is unoccupied and the system is far from equilibrium. Then the electrons are transferred from the bulk of the material and captured by the surface state to form O^-. As more and more electrons occupy the surface state, the fractional occupancy required for equilibrium becomes lower, shown as E_F and E_t are getting closer. If we designate the energy state of the electrons in the vacuum as the constant reference state, E_t won't vary at all time. Thus, E_F moves downward to E_t. The energy levels far from the surface will move synchronously along with E_F since the Fermi distribution function here is unaffected by the surface interaction. However, the energy levels keep immobilized on the surface due to the

constancy of electron affinity χ in a same material, defined as the required energy to move an electron from surface to vacuum. E_F will finally stop moving at a value a bit larger than E_t once the system becomes equilibrium. As a result, a band bending near the surface occurs, shown in Figure 1-5 (a), implying the occupancy probability of electrons lowers down near the surface. In other words, the density of electrons is becoming much less than the bulk. Considering electrons are major charge carriers in an *n*-type semiconductor, a depletion layer forms near the surface.

If E_t lowers down further, the Fermi level will go close to the valence band, or even intersects it (Figure 1-5 (b)) near the surface. In this region, the density of electrons becomes so dilute that holes serve as major charge carriers. Therefore, this region has changed from *n*-type to *p*-type, which is called inversion layer. Under such circumstance, during the sensing process, an *n*-type sensor may perform as a *p*-type one, vice versa. This phenomenon is called "*n*-*p* type transition", and has been reported several times, including our group [33-35]. In most cases, a strong oxidizing gas, such as NO_2, may result in such transition in an *n*-type sensor because they can create a very high density of surface states which leads to a very low E_t. A strong reducing gas may have the similar effect on a *p*-type sensor. It is worth to mention that the *n*-*p* transition totally originates from surface effect, but the properties of the bulk material hardly change.

Now we consider another situation in which the sensor is surrounded by a reducing gas (Figure 1-5 (c)), such as H_2. Similarly, a surface state E_t will form. However, E_t is much higher than E_F this time since H_2 tends to donate electrons

to the material. Hence, E_F will move upwards to get close to E_t until the system reaches the equilibrium. Band bending will also appear but the curvature is upwards. An accumulation layer (typically ~10 nm) will form because the density of free electrons is much higher near the surface than in the bulk, due to the acceptance of electrons from the surface state.

From the explanation above, we are aware that surface state plays a key role during the sensing process. The movement of E_F towards E_t is called Fermi level pinning. It leads to band bending and results in the sensing property. This also explains why semiconducting metal oxides can serve as good sensors but conventional semiconductors such as Si and Ge can't. Atoms in semiconducting metal oxides are connected by ionic bonds. Both anions (O^{2-}) and cations (M^{n+}) have poor coordination at the surface, making the material very attractive to surrounding redox gas molecules. Therefore, a high density of surface state is created. In contrast, atoms in Si and Ge etc. are connected by valence bonds which are much more rigid. The surface cannot adsorb many small molecules, esp. in single crystals. Hence, the density of surface state is quite low. As a result, the surface state level E_t does not exist or close to E_F, so that the Fermi level pinning and band bending won't occur significantly and the gas sensing is unexpected. Another problem with conventional semiconductors is that they are naturally intrinsic semiconductors in which the density of electrons and holes are the same and their conductivity relies on both charge carriers. Hence, the change of electron density cannot lead to the change of resistance in a linear way. For example, the increase of electrons and increase of holes, which represent the

behaviors of two different gas types, may both cause the resistance to decrease. However, if enough density of surface states can be created, and the material can be modified as *n*-type or *p*-type semiconductors, such conventional materials also can be synthesized as gas sensors. A convincing example is *p*-type porous silicon [36]. Here, the porosity creates many poor coordinated atoms and activates the surface, which as a result increases the density of surface states greatly.

1.3.3 Designing a resistive gas sensor

Now that we have been acquainted with the basic mechanism, we are ready to design a resistive gas sensor. First of all, we need to determine which material we need to use when we want to detect a specific type of gases. In this dissertation, we will focus on different polymorphs of WO_3, which will be fully discussed in Section 1.4.

Secondly, we should consider the effect of grain size. Here, Debye length (L_D) becomes an important criterion. The Debye length is the distance over which significant charge separation can occur. In a metal oxide, Debye length represents the distance over which band bending exists from the surface, as well as the thickness of depletion layer. The value of L_D is determined by the following equation:

$$L_D = \sqrt{\frac{\varepsilon\varepsilon_0 kT}{e^2\rho}} \tag{5}$$

ε: dielectric constant of the material; ρ: density of major charge carriers in the material.

Assuming *d* represents the diameter of a crystal grain, if $d > 2L_D$, the depletion or accumulation layer only appears near the surface of the grain. Hence, the resistance of the grain is composed of two parallel parts. One is called surface resistance (R_S), going through the band bending region; while the other is called bulk resistance (R_B). The total resistance is $R = R_S // R_B$. (Figure 1-6 (a)) On the contrary, for crystal grains having $d < 2L_D$, the depletion or accumulation layer stretches the whole grain. Thus the total resistance is only determined by surface resistance, or we can write $R = R_S$. (Figure 1-6 (b)) It is obvious that the surface resistance is strongly influenced by surface reactions but the bulk resistance has nothing to do with the surrounding gas. Therefore, the latter type of grains ($d < 2L_D$) has a much higher sensitivity to surrounding gases. This is true esp. when the depletion layer forms. In this case, $R_S >> R_B$, hence $R \approx R_B$ if $d > 2L_D$, indicating the material has little response to the surrounding gas.

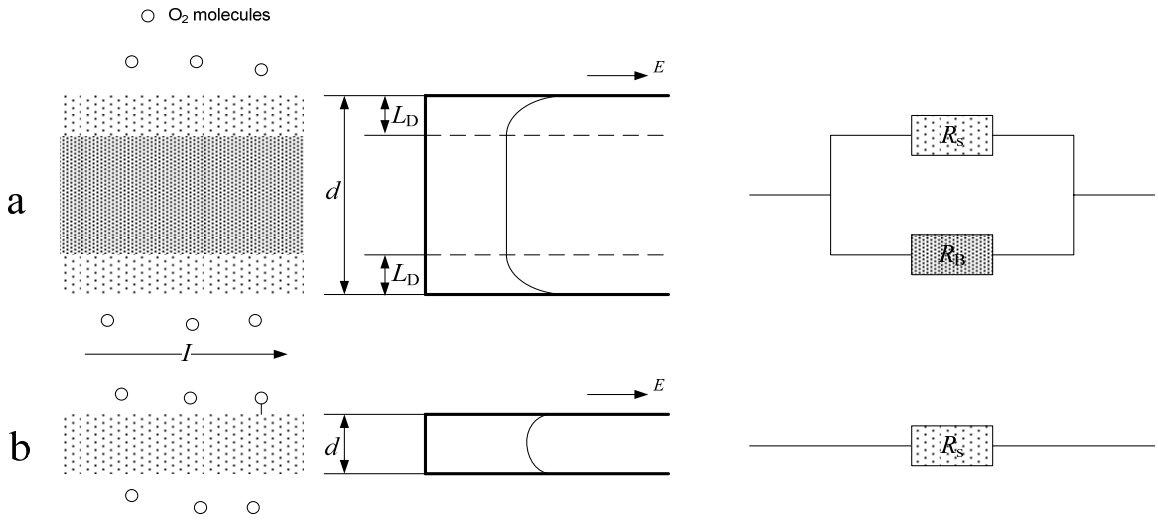

Figure 1-6 The size effect on the sensing system (a) $d>2L_D$; (b) $d<2L_D$.

For γ-WO_3, by using typical values $\varepsilon \approx 10$, $\rho = 4\times10^{22}$ m^{-3} [37] and T=600 K,

we obtain a Debye length of 27 nm, which is quite comparable to the size of nanocrystals. This means nanomaterials may have a much higher sensitivity to detected gases than larger sized materials. From here, we can understand why the term “nano” is so important in the area of gas sensor designs.

After we have synthesized the material, the next step is to integrate them into a device. A typical sensor design will be described in Section 2.3, including an insulating substrate, an electrode connected with the measuring circuit and a sensing film composed of small grains.

To build a hand-held breath analyzer, the sensing element should be very small. In addition, an attached heating element is required. We have developed a functional prototype on purpose whose details will be given in Chapter 5.

1.4 Tungsten trioxides (WO_3)

Tungsten (W), also called wolfram, is the 74^{th} element in the periodical table, which belongs to transition metals. Its atomic weight is 183.84. The word “tungsten” comes from Old Norse “thungr steinn”, in which “thungr” means heavy and “steinn” means stone. Such expression exactly describes its very high density (19.25 g/cm^3). In addition, this element has the highest melting point (3422 °C) and lowest vapor pressure of all metals. The electron configuration of tungsten is $[Xe]4f^{14}5d^4 6s^2$. It has different oxidation states continuously varying from +2 to +6 and therefore a lot of oxides, many of which are non-stoichiometric. WO_3 is the most common kind of tungsten oxides in which tungsten is located in its highest valence state. This section will discuss the structures of WO_3 family members and briefly review their synthesis.

1.4.1 Basic structure of WO_3

All tungsten oxides are based on the [WO_6] octahedron units, one of which is shown in Figure 1-7. In this unit, one tungsten atom and its six neighboring oxygen atoms form a near-perfect regular octahedron. Tungsten is located in the center while oxygen atoms are located in the corners. The average distance between tungsten and oxygen atoms is about 1.90 Å in tungsten oxides; however, this value is alterable according to different structures [38].

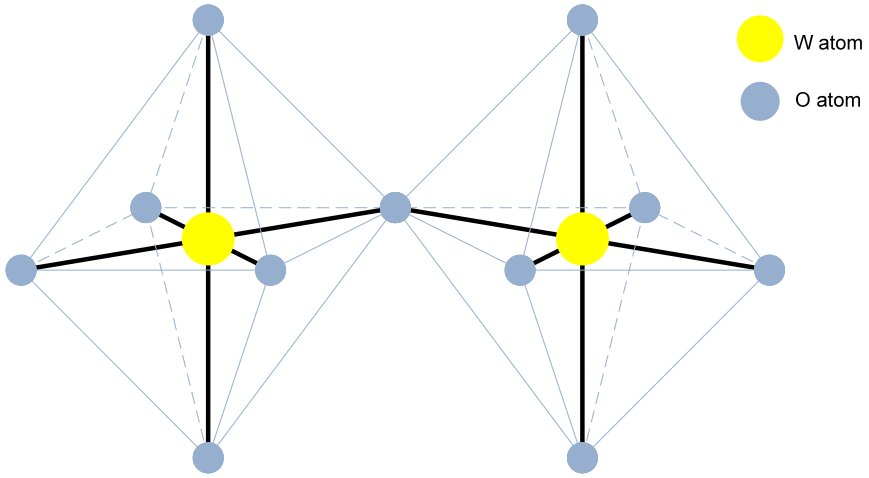

Figure 1-7 Two [WO_6] octahedron units sharing a corner oxygen.

If all the octahedron units connect with each other by sharing corner oxygen atoms (Figure 1-7) and form a three-dimensional (3D) network, they form the compound tungsten trioxide (WO_3). Since these units could connect along different directions, WO_3 has a type of amorphous phase (*a*-WO_3) in which [WO_6] units do not construct a regular pattern, as well as several crystalline phases. Stable crystalline WO_3 phases include: triclinic, monoclinic, orthorhombic and tetragonal ones. Their parameters are shown in Table 1-3.

Table 1-3 Basic parameters of different crystalline WO_3 phases [39].

Structure	Symbol	Temperature	Space Group	Lattice parameters
Monoclinic	*ε*	<-40 °C	*Pc*	*a*=5.278 Å, *b*=5.156 Å, *c*=7.664 Å, *β*=91.762°
Triclinic	*δ*	-40~17 °C	$P\bar{1}$	*a*=7.310 Å, *b*=7.524 Å, *c*=7.685 Å, *α*=88.850°, *β*=90.913°, *γ*=90.935°
Monoclinic	*γ*	17~320 °C	$P2_1/n$	*a*=7.301 Å, *b*=7.538 Å, *c*=7.689 Å, *β*=90.893°
Orthorhombic	*β*	320~720 °C	*Pmnb*	*a*=7.341 Å, *b*=7.570 Å, *c*=7.754 Å
Tetragonal	*α*	720-900 °C	*P*4/*nmm*	*a*=5.250 Å, *c*=3.915 Å
Cubic	*c*	metastable	*I*	*a*=7.521 Å [40]
Hexagonal	*h*	metastable	*P*6/*mmm*	*a*=7.298 Å, *c*=7.798 Å (Type 1)[41] *a*=7.234 Å, *c*=7.662 Å (Type 2)[42]

1.4.2 *α,β,γ,δ*-WO_3

Generally speaking, the stable phases have a similar ReO_3 structure (also a perovskite-like structure). An ideal ReO_3 structure (shown in Figure 1-8) can be treated as the repeat and extension of an octahedron unit along *a*, *b*, *c* axes vertical to each other.

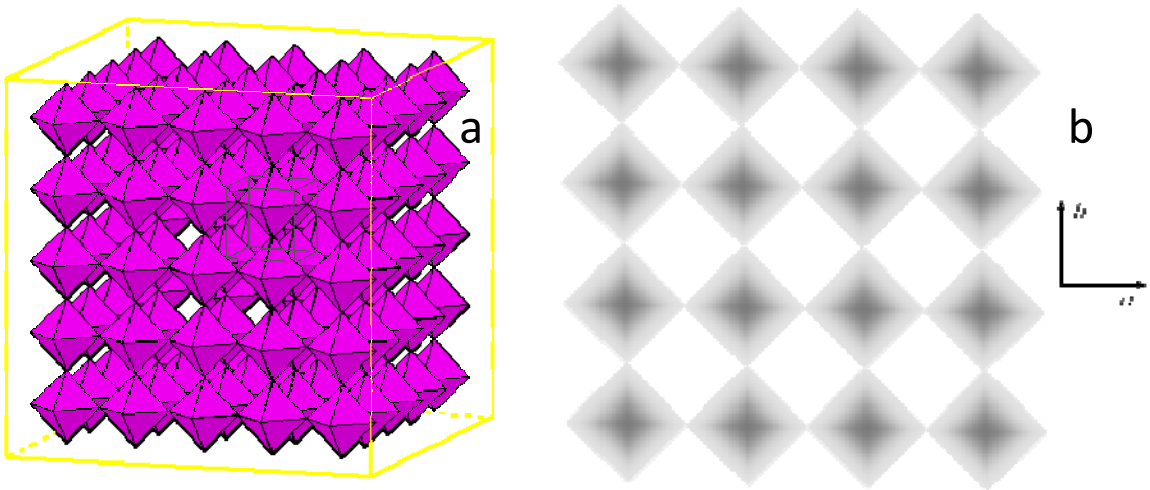

Figure 1-8 A sketch figure of ReO_3 structure: (a) 3D view; (b) Top view.

Every stable WO_3 phase could be recognized as a distortion of the above ReO_3 structure. From *α* phase to *δ* phase, such distortion occurs between two

adjacent [WO_6] units. For example, Figure 1-9 shows the structure difference between *γ*-WO_3 and *δ*-WO_3 [39]. It is clear that both deformation and tilt occurs along every direction in *δ*-WO_3; whereas in *γ*-WO_3 there is only deformation but not tilt along the [010] direction.

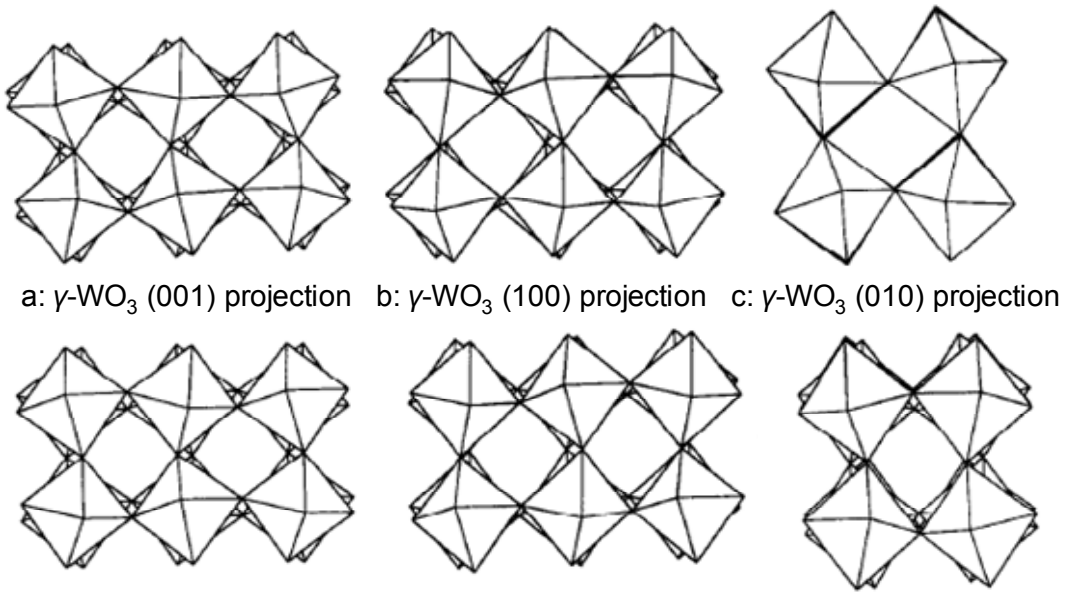

a: *γ*-WO_3 (001) projection b: *γ*-WO_3 (100) projection c: *γ*-WO_3 (010) projection

d: *δ*-WO_3 (001) projection e: *δ*-WO_3 (100) projection f: *δ*-WO_3 (010) projection

Figure 1-9 Structure comparison of *γ*-WO_3 and *δ*-WO_3.*

1.4.3 *ε*-WO_3

It is easy to conclude that the symmetry of WO_3 is lowered from *α* phase to *δ* phase as temperature goes down. Accordingly, its change of physical properties can be observed. However, the most significant property changes occur when WO_3 undergoes a *δ*-*ε* transition at around -40 °C. For example, a remarkable volume contraction occurs upon transformation into the *ε* phase (indicated in Table 1-3). In addition, the resistivity increases 20-30 times, according to Salje *et al.*'s research. The band gap increases from 2.6 eV to an

* Reprinted from Journal of Physics and Chemistry of Solids, 1995, 56(10): p. 1305-1315. Copyright 1995, with permission from Elsevier.

unknown value >2.85 eV, resulting in a color change from pale green to bluish white [43]. They also observed piezoelectricity in that phase. Other studies [44] confirm this phase exhibit a unique ferroelectric characteristic.

The above information suggests that the *ε* phase of WO_3 has a quite different structure from any other stable phase, which is exactly the truth. Like other stable phases, *ε*-WO_3 can also be treated as the distortion of an ideal ReO_3-like structure. However, different from other phases, such distortion does not occur only between adjacent [WO_6] units, but also inside every unit. As shown in Figure 1-10, the rotations of [WO_6] octahedra in two adjacent layers are in the same direction in the *γ* phase, but in opposite directions in the *δ* and *ε* phases. Detailed study reveals that the *γ*-to-*δ* transition involves with the change of the octahedral titling pattern, whereas no change in the tilt pattern occurs at the *δ*-to-*ε* phase transition.

By carefully examining the direction and magnitude of the tungsten shifts in each [WO_6] octahedron of the three phases, one can find that every tungsten atom always has a slight shift from its central position along every direction. Whereas in the *γ* and *δ* phases the magnitude of the shifts in every direction (x, y and z) is all roughly the same, in the *ε*-phase the shifts in the negative z direction are larger than those in the positive z direction. (Sketched in Figure 1-10) [45][46] Because of the inequality of shifts in the z direction, a net spontaneous polarization develops. This is the origination of ferroelectricity in the *ε* phase.

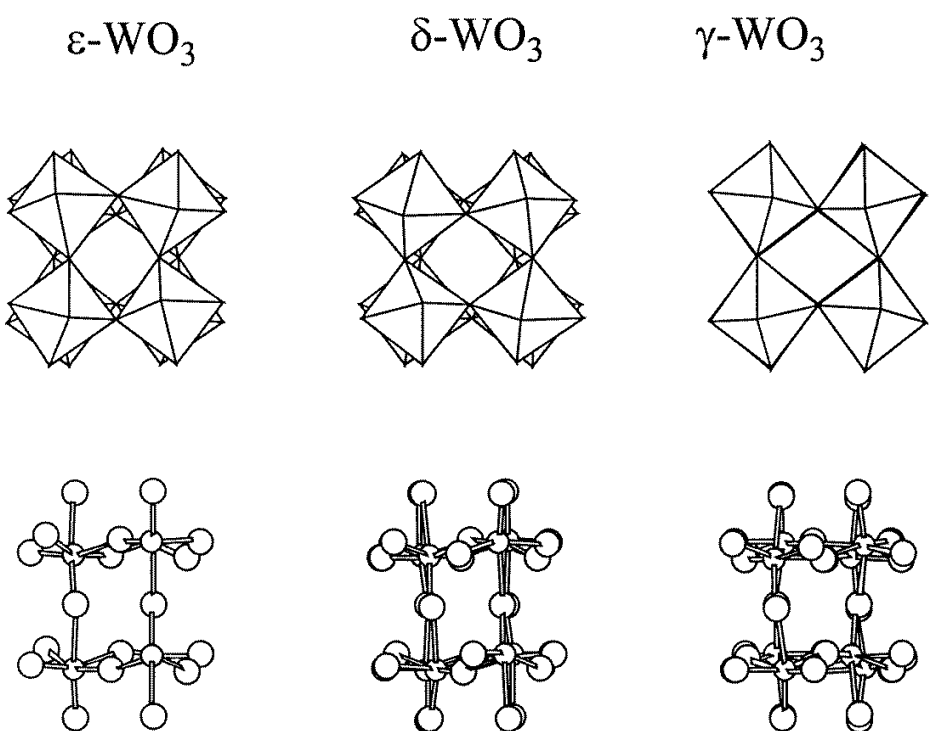

Figure 1-10 Principle features of the structures of *γ*, *δ*, *ε*-WO_3 showing the tilting of the WO_6 octahedra (top) and the W–O bonds (bottom).*

The existence of *ε*-WO_3 at RT was firstly reported by Arai *et al.* in 1990.[47] In this work, 100 nm-sized WO_3 microcrystals were prepared by burning a tungsten wire in a gas mixture of Ar and O_2. The *ε* phase of WO_3 was found to be mixed with *γ*-WO_3 in the final product at RT according to the Raman spectra. In a follow-up research, the same group suggested that larger microcrystals tend to take the *γ* phase and smaller microcrystals tend to take the *ε* phase. [48] Since then, *ε*-WO_3 at RT was occasionally reported in several other works, mixed with *γ*-WO_3. [49-51] However, they did not study the high temperature stability of *ε*-WO_3 nor did they give any explanations why *ε*-WO_3 exists.

* Reprinted from Journal of Physics: Condensed Matter, 1997, 9(31): p. 6563-6577. Copyright 1997, with permission from IOP.

1.4.4 *h*-WO_3

WO_3 also has another metastable hexagonal phase whose structure is totally different from the stable ones (Figure 1-11, [41]). Its basic lattice parameters are also shown in Table 1-3. In this structure, every three adjacent octahedron units connect with each other by sharing corner oxygen atoms in the same layer and such connection extends along [0001], $\frac{1}{3}[2\bar{1}\bar{1}0]$, and $\frac{1}{3}[\bar{1}2\bar{1}0]$ directions (*c*, *a*, *b* axes, respectively) in a hexagonal lattice to form a network. Such construction results in many hexagonal prism channels along the *c* axis, which allows small molecules to travel through it. Hence, compared to all kinds of stable phases, which are closely-packed structures, *h*-WO_3 is much more open.

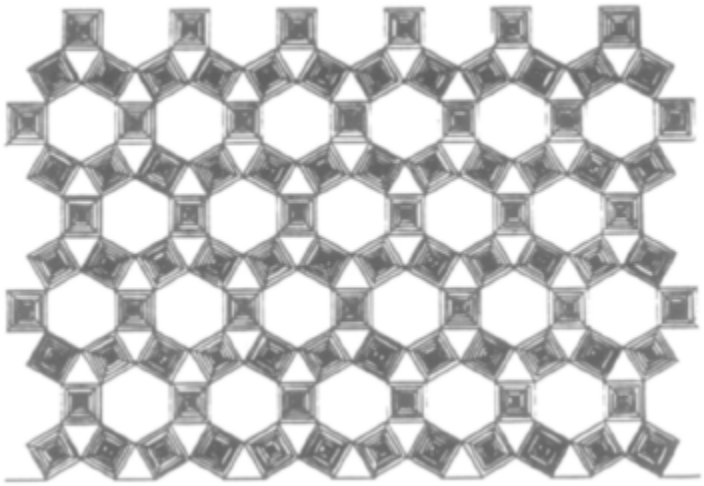

Figure 1-11 A sketch figure of *h*-WO_3 structure: (0001) projection.*

Such open tunnel structure will inevitably influence its behavior. For example, small metal ions (e.g. Li^+ NH_4^+) are able to intercalate into its framework forming M_xWO_3 bronzes. On one side, this enables *h*-WO_3 a

* Reprinted from Journal of Solid State Chemistry, 1979, 29(3): p. 429-434. Copyright 1979, with permission from Elsevier.

promising material for negative electrodes of rechargeable lithium batteries.[52-55]. On the other, trace ions or atoms could always be found in final *h*-WO_3 products. Szilágyi *et al.* [56] observed that when residual NH_4^+ ions and NH_3 molecules in the hexagonal channels were completely released, the hexagonal framework collapsed into *γ*-WO_3. It was proposed that the structure of *h*-WO_3 cannot be maintained without traces of stabilizing ions or molecules in the hexagonal channels, which means the existence of strictly stoichiometric *h*-WO_3 is unlikely to occur.

It should be mentioned that there are two kinds of *h*-WO_3 whose structures are slightly different depending on different synthesis methods, a=7.298 Å, c=7.798 Å for Type-1 *h*-WO_3 (JCPDS No.:75-2187) and a=7.234 Å, c=7.662 Å for Type-2 *h*-WO_3 (JCPDS No.:85-2460). Most reported processes lead to Type-1 products. In 1979, Gerand *et al.* [41] obtained *h*-WO_3 particles for the first time by heating of a hydrate $WO_3 \cdot \frac{1}{3}H_2O$ and studied its crystallographic characteristics. This hydrate was prepared by hydrothermal treatment at 120°C of an aqueous suspension of either tungsten acid gel, which may be obtained from the reaction between tungstates and acids, or crystallized $WO_3 \cdot H_2O$. Only thermal decomposition of ammonium salt leads to Type-2 *h*-WO_3. In 1981, Cheng *et al.* reported the synthesis of this *h*-WO_3 by directly heating ammonium paratungstate for 2 h at 350 °C. [57] Oi *et al.* obtained the similar products by low temperature sintering ammonium peroxo-polytungstate precursor and he calculated the lattice parameters of this structure. [42] In 2001, Solonin *et al.* used $CuWO_4$ (obtained from the reaction between CuO and *γ*-WO_3) as precursor to produce the

hexagonal phase of hydrogen tungsten bronze, H_xWO_3. The oxidation of H_xWO_3 finally formed non-stoichiometric *h*-WO_3. [58]

Besides powders, other shapes of *h*-WO_3 were also reported. In 2006, Oaki *et al.* prepared a $BaWO_4$-PAA nanohybrid in aqueous solution following the reaction between $BaCl_2 \cdot 6H_2O$/PAA and Na_2WO_4 and then converted to *h*-WO_3 nanosheets via desiccation of the colloidal suspension. [59] In 2006, Wu *et al.* heated tungsten wires at around 800 ˚C in a humid argon flow and hexagon-shaped *h*-WO_3 tubes with well faceted end and side surfaces were obtained. [60] In 2007, Gu *et al.* managed to produce single-crystal nanowires of Type-1 *h*-WO_3 in a large scale by a simple hydrothermal method starting from Li_2WO_4 and Li_2SO_4 without any templates and catalysts. [55]

1.5 WO_3 as gas sensors

The first work with respect to the WO_3 gas sensors was reported by Shaver [61] in 1967, in which a Pt-activated *γ*-WO_3 thin film was developed to detect airborne H_2 with enhanced sensitivity. However, during the following 20 years, research on WO_3-based sensors had merely developed. On one hand, TiO_2 and SnO_2 were mainstream chemo-resistive gas sensors, drawing major attentions, and have been commercialized successfully. On the other hand, the research on WO_3 was focused on its outstanding electrochromic property.

This status changed after 1990s when *γ*-WO_3 was found to have an excellent sensitivity to NO_x [62] The author found that the sensitivity of the sensor was as high as 31 and 97 to 200 ppm NO and 80 ppm NO_2, respectively, at 300 °C. Although this value is not very high from today's opinion, the report

created a brand new direction on the WO_3 research. Even today, γ-WO_3 is still described as NO_x sensitive sensor and research on this topic is extensive.

Most of reported WO_3 sensors used small-grained thin/thick films as materials. Different methods were developed to deposit films, e.g. reactive sputtering [63], pulsed laser deposition [64], wet process [65], vacuum thermal deposition [66] and chemical vapor deposition [67] etc. Those methods were dedicated to increase the surface area of the sensor by producing smaller grains and/or creating more pores in the materials. Recently, as one-dimensional (1D) nanostructures have drawn more and more attention, WO_3 1D nanostructures have also been successfully synthesized and applied to gas sensing. [68, 69] Ponzoni *et al.* used three-dimensional WO_3 nanowire networks as a high-surface area material for building ultrasensitive and highly selective gas sensors.[70] The sensitivity went as high as 200 towards 1 ppm NO_2 at 300 °C and it was capable to detect concentration as low as 50 ppb. This is the most sensitive WO_3 sensor for NO_2 detection reported ever.

To modify the sensing properties, other elements or compounds were usually added into the system, forming composite materials or doped/activated materials. Existing doping elements include Cu [71], noble metals [72-74], Ta [75], In [76] and Cr [77] etc. Metal oxides, such as TiO_2 [74, 78-80], MoO_3 [81], and SnO_2 [82] etc. were also reported to add into WO_3 material to form composites. Most recently, a WO_3/carbon nanotubes [83] hybrid sensing layer was developed as a novel sensing system. This sensor has no cross-sensitivity to other hazardous gases. More importantly, it could be operated at room temperature,

which is a great improvement for WO_3 sensor commercialization.

It is known that γ-WO_3 is sensitive to oxidizing gases, not only NO_x. In practice, H_2S and O_3 sensors based on WO_3 were also widely reported. [84, 85] The first WO_3-based H_2S sensor was reported by Barrett *et al.* in 1990 [86]. Generally speaking, the response values to ppm levels of H_2S vary between 3 and 100 depending on manufacturing techniques [87, 88], material morphologies [70, 89, 90], doping elements [91-93] and working temperatures. Reports on ozone sensors include: [94-100]. However, the sensitivities to H_2S and O_3 are comparatively smaller than that to NO_x.

Besides oxidizing gases, WO_3 has also been used to detect some reducing gases. To accomplish selective detection on these gases, activation or modification using other elements were always necessary since pure WO_3 cannot provide a favorable selectivity or sensitivity. For example, Au-doped WO_3 was proved to be selective to NH_3 [101-104]. A highly sensitive gas sensor for the detection of aromatic hydrocarbons has been developed using a WO_3 thick film where Pd and Pt were applied as catalyst. [105] Pt-loaded Al_2O_3 catalytic filters were developed to enhance the sensitivity and selectivity of WO_3 films to benzene [106]. However, generally speaking, research on reducing gas (esp. VOCs) detection based on WO_3 is still underdeveloped.

1.6 Research statement

From the discussion in Section 1.2, current breath analyses are mainly based on bulky instrumentation and skilled operators. Sample collection /preconcentration involving a complicated procedure is required before testing.

Furthermore, some or all of the breath acetone may be lost during these time-consuming procedures. Because of these limitations, these methods are not suitable for use in human disease diagnosis and monitoring applications outside the laboratory. To meet the need for clinic applications, relatively inexpensive, portable instruments capable of providing non-invasive, real-time, sensitive, and selective analysis of breath gases for medical diagnosis is highly desirable.

On the other hand, although various sensors based on WO_3 have been developed during the last twenty years, they are all based on room temperature stable *γ* phase, sometimes its adjacent *β* or *δ* phases or amorphous structure. However, we are already aware that WO_3 exists in a series of stable phases as well as a metastable phase. Among them, more attention should be drawn to the ferroelectric *ε* phase and the open-structured *h* phase due to their unique structures. However, their properties, esp. sensing properties, has not been fully studied at all, partly because it is difficult to produce these materials and maintain their phases at room temperature or higher, which is the typical working temperature for a chemo-resistive sensor.

This dissertation will focus on synthesis and stabilization of *ε*-WO_3 and *h*-WO_3 nanostructures. Their sensing properties will be fully discussed, esp. to those biomarkers. Finally, effort will be taken on manufacturing a portable breath analyzer ready for clinical applications.

CHAPTER 2 Experimental details

The purpose of this chapter is to describe all the experimental details in this dissertation. First of all, two different methods have been used for synthesizing WO_3, with different structures and dopants, including acid-precipitation method and flame-spray pyrolysis method. Furthermore, different characterization methods will be introduced, including X-ray diffraction (XRD), scanning electron microscopy (SEM), transmission electron microscopy (TEM), Raman spectroscopy and BET surface area analysis, etc. Then a gas sensing test setup will be introduced to measure the sensing properties of synthesized samples. Finally, the design of a special sensor prototype for human breath analysis will be discussed.

2.1 Synthesis methods

2.1.1 Acid precipitation

This method is mainly used to synthesize *h*-WO_3, although *γ*-WO_3 can also be produced in this way. It is somewhat similar with the method used by Gerand *et al.* in 1979 [41]. The detailed description is as follows:

1.17 g of $Na_2WO_4 \cdot 2H_2O$ of analytical grade is dissolved in 17ml of water and the solution is cooled to 10 °C. To this 8.4 ml of normal hydrochloric acid solution (analytical grade, 18% in excess of equimolar reaction) cooled to the same temperature is added in one dose. The mixture is put back into the refrigerator and allowed to stay for about 20 h. The following reaction occurs:

$$Na_2WO_4 \cdot 2H_2O + H^+ = H_2WO_4 \cdot 2H_2O + Na^+ \quad (6)$$

After this time the whole mixture turned to a whitish gel. Then 110 ml of water was added to the vessel and the gel and water were lightly stirred manually. After centrifuging the supernatant liquid was removed. Then 130 ml of water was added to the precipitate and the steps of light manual stirring, centrifuging and removal of supernatant liquid were repeated several times to obtain $H_2WO_4 \cdot H_2O$, the precursor of final *h*-WO_3 powders. $H_2WO_4 \cdot H_2O$ suspensions were passed to hydrothermal dehydration, carried out in Parr acid digestion bombs at autogeneous pressure at 125 ºC ± 5 ºC. Dehydration under air: furnace temperature: 300 - 330 ºC, annealing time: 90 min.

$$H_2WO_4 \cdot 2H_2O \rightarrow WO_3 \cdot \frac{1}{3}H_2O \rightarrow h - WO_3 \quad (7)$$

2.1.2 Flame-spray pyrolysis (FSP)

Flame-spray pyrolysis is a very effective method to synthesize nano-sized oxide particles in a large amount and an excellent quality. It has been used for dry, one-step synthesis of catalysts, sensors, biomaterials, phosphors and even nutrional supplements.[107] Furthermore, FSP is a scalable process with proven production rates over 1 kg/h. [108-110] FSP-made TiO_2 nanoparticles show an excellent sensitivity to acetone and other VOCs at low concentration (down to 1 ppm). [111] FSP-made nanoparticles can also be directly deposited onto sensor substrates. Thus, chemo-resistive sensors based on such flame-made materials, are promising candidates for non-invasive and real-time diabetes diagnosis device.[112]

The details of FSP for metal oxide nanoparticle synthesis have been described in detail elsewhere. [113] A typical flame aerosol reactor set-up (Figure

2-1) consists of a precursor unit (bubbler or evaporator), a burner accompanied by a gas delivery system and a filter unit to collect the product particles. Various flame configurations are used for the manufacture of nanoparticles, such as premixed and diffusion flames run in co-flow, or counterflow. In the diffusion flame configuration the fuel and the oxidizer diffuse into each other determining flame reaction and particle formation, while in premixed flames the precursor and the combustible gases are mixed before they enter the reaction zone (flame).

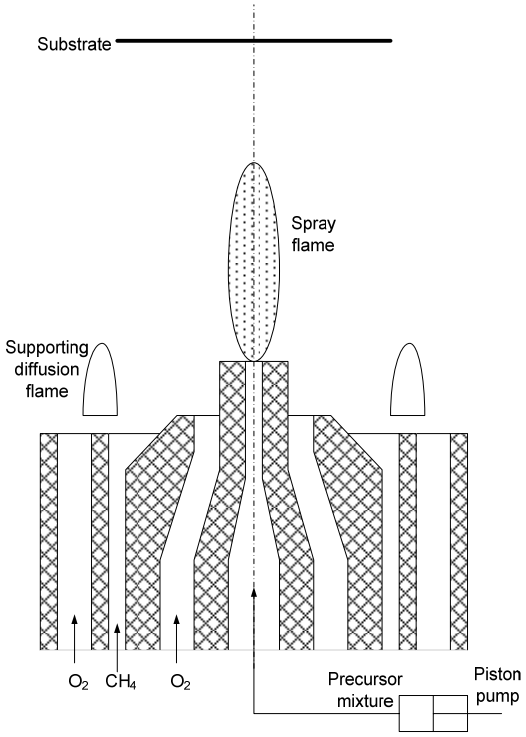

Figure 2-1 A sketch map of the FSP setup.

In this project, precursor solutions are prepared from ammonium tungstate hydrate ($H_{26}N_6O_{41}W_{12}$, Aldrich, purity >97%) diluted (0.4 mol/l of tungsten ions) in a 3:2 (volume ratio) mixture of diethylene glycol monbutyl ether ($C_8H_{18}O_3$ Fluka, >98.5%) and ethanol (C_2H_6O, Fluka, >99.5%).By default, the solution is fed at 5 ml/min through the inner reactor capillary. Through the surrounding

annulus, 5 l/min of oxygen (Pan Gas, purity >99%) are fed dispersing the precursor solution into a combustible spray. The methane and oxygen flow rates in the FSP-supporting premixed flame are 1.5 and 3.2 l/min, respectively. The spray flame could be optionally sheathed with 40 l/min of oxygen gas for quenching or enclosed by a 40 cm long glass tube for thermal insulation. The whole process can be expressed as:

$$H_{26}N_6O_{41}W_{12} \xrightarrow{\text{flame}} W^{6+} \xrightarrow{O_2} WO_3 \quad (8)$$

For doping synthesis, manganese (II) acetyl-acetonate ($(C_5H_8O_2)_2Mn$), is used for Mn doping. Chromium (III) acetyl-acetonate ($(C_5H_7O_2)_3Cr$) is used for Cr, doping respectively. These materials are added into the precursor solution in variable molar ratios to ammonium tungstate hydrate, but keep the total concentration of metal ions constant at 0.4 mol/l.

Table 2-1 lists all the products which have been successfully synthesized and using FSP method. Their structures and properties will be discussed in Chapter 3.

Table 2-1 WO_3 products synthesized by FSP method.

Sample No.	Accessory	Dopant
A	N/A	N/A
B1	5 cm quenching sheath	N/A
B2	10 cm quenching sheath	N/A
C1	10 cm insulation tube	N/A
C2	20 cm insulation tube	N/A
C3	30 cm insulation tube	N/A
D1	N/A	1 at% Cr
D2	N/A	5 at% Cr
D3	N/A	10 at% Cr
E1	N/A	1 at% Mn
E2	N/A	10 at% Mn

2 . 2 Characterization methods

2.2.1 X-Ray diffraction (XRD)

X-ray diffraction is a versatile, non-destructive technique that reveals detailed information about the chemical composition and crystallographic structure of natural and manufactured materials.

When a monochromatic X-ray beam with wavelength λ is projected onto a crystalline material at an angle θ, diffraction occurs only when the distance traveled by the rays reflected from successive planes differs by a complete number n of wavelengths. Assuming that the distance between adjacent crystal planes is d, such diffraction condition can be described in the following equation called Bragg's Law:

$$2d \sin\theta = \lambda \tag{9}$$

By varying the angle θ, the Bragg's Law conditions are satisfied by different d-spacings in polycrystalline materials. Plotting the angular positions and intensities of the resultant diffracted peaks of radiation produces a pattern, which is characteristic of the sample. Where a mixture of different phases is present, the resultant diffractogram is formed by addition of the individual patterns.

In this project, we use XRD to identify the crystal structures of the products, the presence forms of dopants (forming compounds or solid solutions). If the product contains several phases, we will calculate their relative percentages with the assistance of softwares. X-ray diffraction (XRD) patterns are obtained with a Bruker AXS D8 Advance diffractometer (40 kV, 40 mA, Karlsruhe, Germany) operating with Cu K_α radiation. Phase analysis is accomplished using two

softwares, namely DIFFRAC^{plus} EVA and DIFFRAC^{plus} TOPAS.

2.2.2 Scanning Electron Microscopy (SEM)

Scanning electron microscope is a type of electron microscope capable of producing high-resolution images of a sample surface using electrons rather than light. Due to the manner in which the image is created, SEM images have a characteristic three-dimensional appearance and are useful for judging the surface structure of the sample.

In an SEM, a beam of electrons is produced at the top of the microscope by heating of a metallic filament or by field emission. The electron beam follows a vertical path through the column of the microscope. It makes its way through electromagnetic lenses which focus and direct the beam down towards the sample.

When the electron beam strikes the sample, some of the electrons will interact with the nucleus of the atom. The negatively-charged electron will be attracted to the positive nucleus, but if the angle is just right it will circle the nucleus and come back out of the sample without slowing down. These electrons are called backscattered electrons. Sometimes, beam electrons interact with the electrons present in the atom rather than the nucleus. The latter electrons will be repelled since they are both negatively charged. The repulsion may be so great that the specimen electrons are pushed out of the atom, and exit the surface of the sample, these are called secondary electrons. The electron beam scans every region of the sample surface. Detectors synchronously collect the secondary or backscattered electrons, and convert them to a signal that is sent to

a viewing screen similar to the one in an ordinary television, producing an image.

In this project, we use SEM to observe the morphology of the products, including the grain sizes, the grain-grain and grain-electrode contact. SEM images are obtained with SEM, LEO 1550 SFEG Microscope operated at a voltage of 15 kV.

2.2.3 Transmission Electron Microscopy (TEM)

Transmission electron microscope is another type of electron microscope which can produce very high-solution images and electron diffraction patterns of a sample.

The generation of electron beams in TEM is the same as that in SEM. Differently the generated beams then strike a very thin sample. Some beams penetrate the sample directly while some others undergo Bragg diffraction. These transmitted beams are refracted by an objective lens. Beams coming from the same region of the sample converge on the image plane while beams diffracted by the same crystal plane converge on the back focal plane. The image plane contains the morphology information of the sample and the back focal plane contains the diffraction pattern information.

The beams are passed down the column through the intermediate and projector lenses, being enlarged all the way. Then strikes the phosphor image screen and light is generated, allowing the user to see the image. If the above image plane is adjusted as the object plane of the downstream lens, the morphology of the sample will appear on the screen. If the back focal plane is the object plane, the screen will show the diffraction pattern.

In this project, we use TEM to observe the shapes of the grains and measure their sizes. Besides, through the diffraction pattern, we will determine their crystal structures. The instrument information is provided here: CM30ST microscope, FEI (Eindhoven), LaB6 cathode, operated at 300 kV, SuperTwin lens, point resolution ~2 Å.

2.2.4 Raman Spectroscopy

Raman Spectroscopy is a spectroscopic technique used to study vibrational, rotational, and other low-frequency modes in a system. Since vibrational information is very specific for the chemical bonds in molecules, it provides a fingerprint by which the molecule can be identified. Therefore, Raman spectroscopy can be applied to characterize materials and study changes in chemical bonding.

This technique relies on inelastic scattering, or Raman scattering of monochromatic light. The Raman Effect arises when a photon is incident on a molecule and interacts with the electric cloud of the molecule. Scattering of photons occurs consequentially. Most photons are elastically scattered (Rayleigh scattering). The scattered photons have the same energy (frequency) and, therefore, wavelength, as the incident photons. However, a small fraction of light (approximately 1 in 10^7 photons) is scattered at optical frequencies different from, and usually lower than, the frequency of the incident photons. The process leading to this inelastic scatter is the termed the Raman Effect.

In this project, Raman spectroscopy is mainly used to investigate heat treatment effect and doping effect of different concentrations of foreign atoms on

the chemical bonding of the products. Raman scattering spectra were recorded by Renishaw InVia Reflex Raman Spectrophotometer with the excitation laser length of 514.5 nm, laser power of 300 mW and exposure time of 30s at RT.

2.2.5 BET surface area analysis

Brunauer-Emmett-Teller (BET) surface area analysis is a technique widely used to measure the specific surface area of small particles. It is based on BET Theory, named after its three co-founders: Stephen Brunauer, Paul Hugh Emmett, and Edward Teller. “BET” consists of the first initials of their family names.

This theory deals with the physical adsorption of gas molecules on a solid surface and results in the following equation:

$$\frac{1}{V\left(P/P_0 - 1\right)} = \frac{c-1}{V_m c}\left(\frac{P}{P_0}\right) + \frac{1}{V_m c} \tag{10}$$

Here, P and P_0 are the equilibrium and the saturation pressure of adsorbates at the adsorption temperature, V is the adsorbed gas quantity (for example, in volume units), Vm is the monolayer adsorbed gas quantity and c is the BET constant. This equation can be plotted as a straight line with $\frac{1}{V\left(P/P_0 - 1\right)}$ on the y-axis and $\frac{P}{P_0}$ on the x-axis according to experimental results P, P_0 and V. V_m and c can be calculated from the value of the slope and the y-intercept of the line.

A specific surface area SA is evaluated by the following equation:

$$S = \frac{V_m N s}{mV} \tag{11}$$

N: Avogadro's number; s: adsorption cross section, a known constant for an adsorbed gas at a certain temperature; V: molar volume of adsorbent gas; m: weight of sample solid.

In addition, the particle diameters can be calculated from specific surface area through the following equation, assuming those particles have approximately spherical shapes. This diameter is called BET equivalent average diameter (d_{BET})

$$d_{\mathrm{BET}} = \frac{6}{S\rho} \tag{12}$$

ρ: weighted density of studied material. For *γ*-WO_3, ρ=7.16 g/cm^3. This value can be applied to other stable phases of WO_3 since they share very similar structures and lattice parameters.

In this project, we use BET analysis to measure the specific areas and particle diameters of the synthesized WO_3 particles. The measurement is carried on by nitrogen adsorption at 77K (Micromeritics Gemini 2375) after degassing the sample, at least, for 1 h at 150 ˚C in nitrogen.

2.2.6 X-ray photoelectron spectroscopy (XPS)

X-ray photoelectron spectroscopy is a quantitative spectroscopic technique that measures the elemental composition, empirical formula, chemical state and electronic state of the elements that exist within a material. XPS spectra are obtained by irradiating a material with a beam of aluminum or magnesium X-rays while simultaneously measuring the kinetic energy and number of electrons that

escape from the top 1 to 10 nm of the material being analyzed. Accordingly, it is a surface chemical analysis technique that can be used to analyze the surface chemistry of a material.

In this project, we use XPS to determine the surface composition of synthesized products. XPS spectra were collected by a VG Microtech instrument consisting of a XR3E2 X-ray source, a twin anode (Mg Kα and Al Kα), and a CLAM 2 hemispherical analyzer using Mg Kα radiation. The spectrometer was calibrated withthe binding energy of the C1s line (284.5 eV).

2.2.7 Thermal analysis

Thermal analysis generally covers three different experimental techniques: Thermo Gravimetric Analysis (TGA), Differential Thermal Analysis (DTA), and Differential Scanning Calorimetry (DSC).

The basic principle in TGA is to measure the mass of a sample as a function of temperature. The method for example can be used to determine water of crystallization, study oxidation and reduction. Many thermal changes in materials (e.g. phase transitions) do not involve a change of mass. In DTA one instead measures the temperature difference between an inert reference and the sample as a function of temperature. When the sample undergoes a physical or chemical change the temperature increase differs between the inert reference and the sample, and a peak or a dip is detected in the DTA signal. The technique is routinely applied in a wide range of studies such as identification, quantitative composition analysis, phase diagrams, hydration-dehydration, thermal stability, polymerization, purity, and reactivity.

TGA and DTA techniques are used in this project to study the phase stability of produced materials at elevated temperatures. They were accomplished on a Linseis STA PT1000 thermal analyzer under static air. The sample was heated to 800 °C at a rate of 5 °C/min. Calcined alumina was taken as the reference material.

2.3 Gas sensing test setup

To prepare for the WO_3 gas sensor, 0.1 g of the synthesized WO_3 powders are weighed into 3 ml of heptanol and the suspension is ultrasonically stirred for at least 1 h. Two drops of the suspension are then removed to drip on an Au electrode-coated Al_2O_3 substrate (shown in Figure 2-2). The substrate is left at the room temperature (RT) for 1 h until the solution evenly spread on the substrate. Then the substrate was dried at 75 ºC for 10 min to remove the liquid. Such process was repeated for 3 times and then a uniform WO_3 thin film gas sensor was successfully prepared.

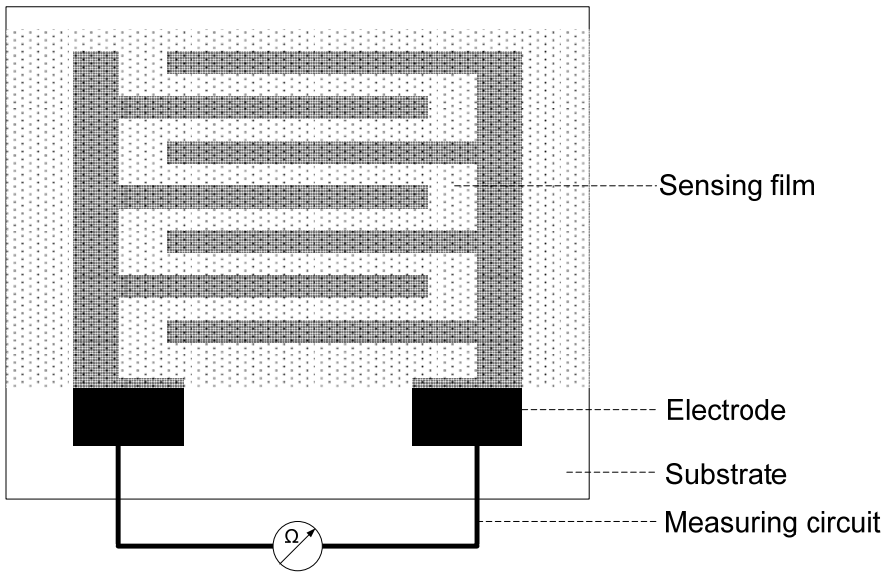

Figure 2-2 A sketch map showing a typical resistive sensor design.

The setup of gas sensing measurement is depicted in Figure 2-3. The as-prepared sensor is then put into a glass tube, connected with the outside measuring circuit and then laid inside a horizontal tube furnace. A heat treatment is usually necessary for the sensor to get stable, e.g., to remove the residual tungsten hydrate by-product. For *h*-WO_3, the heat treatment is done at 350 ˚C for 8 h, and for *γ*, *ε*-WO_3, it is done at 500 ˚C for 8h. After that, a unilateral gas flow containing a mixture of N_2/O_2 (80%/20%; volume ratio) goes through the glass tube which simulates the atmosphere environment. The measured resistance is the base line value. When the gas sensing test starts, a certain kind of redox gases or VOCs will be added into the flow at a controlled concentration and the resistance change will be recorded. The measuring temperature varies from RT to up to 500 ˚C depending on the requirement.

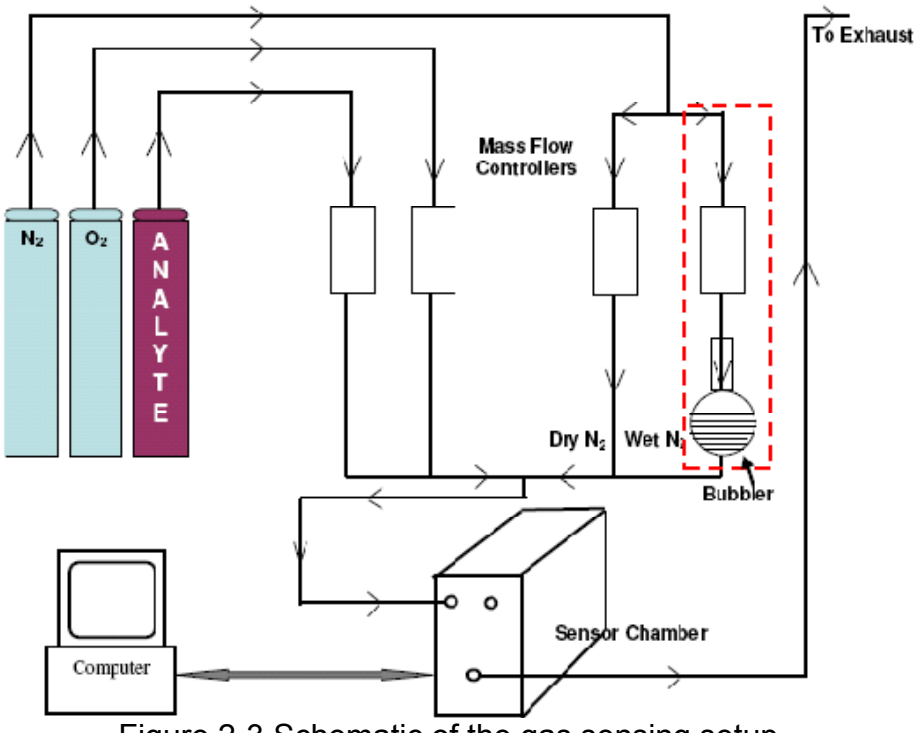

Figure 2-3 Schematic of the gas sensing setup.

CHAPTER 3 ε-WO_3: characterization and sensing properties*

3.1 Morphologies and structures

3.1.1 As-synthesized pure WO_3

By controlling synthesis parameters, pure WO_3 with different grain sizes can be obtained using FSP method. Generally, the as-synthesized products are blue green in color.

When a default setup without any accessories is applied, medium grain-sized WO_3 will be obtained. (Sample A) The average surface area of such products is 63.0 m^2/g, whose according BET particle diameter is 13 nm. Most peaks in the XRD spectrum shown in Figure 3-1 (a) (labeled as "middle grain size") can be indexed in stable-phased WO_3 polymorphs. However, due to the small sizes of the particles, most adjacent peaks overlap a lot. Instead, Raman spectroscopy was used to identify the phase composition of the product, whose result is shown in Figure 3-1 (b). In this spectrum, peaks at 272, 324, 715 and 805 cm^{-1} correspond to monoclinic γ phase whose structural details could be found in Table 1-3 which is the stable form of WO_3 at RT. [114] The band at 942 cm^{-1} can be assigned to the stretching mode of W=O terminal bonds indicating surface tungsten hydrates. [114] Peaks at 203, 272, 303, 370, 425, 642, 688 and 805 cm^{-1} belong to the ε phase of WO_3 (see Table 1-3 for details). [47] Tungsten hydrates are common by-products during the synthesis of WO_3. However, the

* Part of this chapter is reprinted with permission from Chemistry of Materials, 2008. 20(15): p. 4794-4796. Copyright 2008, American Chemical Society.

appearance of ε-WO_3 is surprising here since it was reported as a phase only stable below -40 °C. Although not quantitative, the relative intensity of 642 cm^{-1} and 688cm^{-1} bands compared to 715 cm^{-1} band indicates the content of ε-WO_3 in the products. It is clear that this as-synthesized product contains a fairly high percentage of ε-WO_3. Computer-assisted phase analysis based on the XRD spectrum enables us to quantitatively determine the fraction of either phase, whose result is shown in Table 3-1.

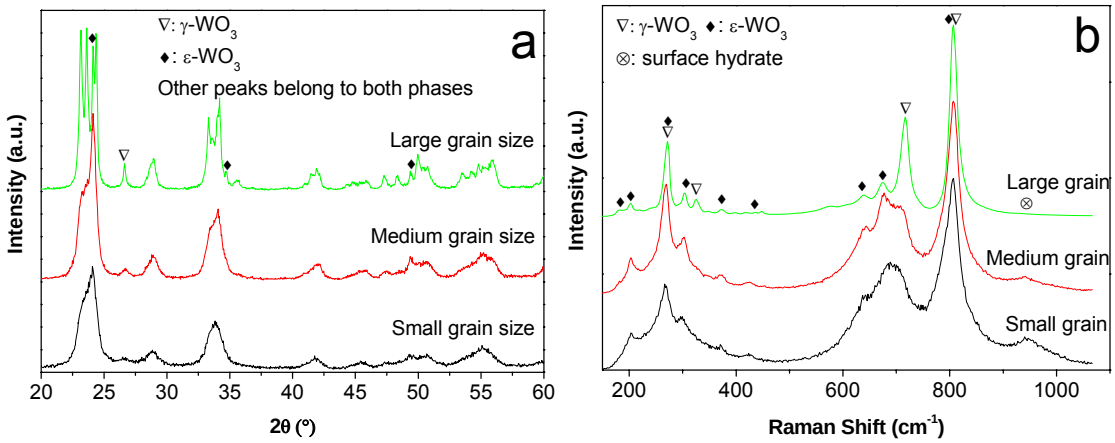

Figure 3-1 (a) XRD and (b) Raman spectra of as-synthesized pure WO_3.

By using a cooling oxygen gas sheath around the flame, smaller grain-sized particles are able to grow. As the quenching sheath diameter shrinks from 10 cm (Sample B2) to 5 cm (Sample B1), the particle diameter decreases from 12 nm (S=66.3 m^2/g) to 9 nm (S=97.0 m^2/g). Figure 3-1 shows the XRD and Raman spectra of Sample B1 (labeled as “small grain size”). The shapes of those spectra are similar to those of medium-sized particles, except that all the peaks in the XRD result are a little bit broader resulting from smaller grain size. Besides, ε-WO_3 becomes a dominant phase in the material, concluded from the enhanced intensity of ε-WO_3 peaks in the Raman result and confirmed by quantitative

analysis in Table 3-1. In addition, the W=O bond peak is also intensified, showing a more active surface in this material, which can be attributed to “nano effect”.

On the contrary, the use of a glass tube on top of the flame enables the growth of particles. The diameters are 16 nm (S=52.5 m^2/g), 20 nm (S=40.5 m^2/g) and 27 nm (S=30.5 m^2/g) when the tube lengths are 10 cm (Sample C1), 20 cm (Sample C2) and 30 cm (Sample C3), respectively. Figure 3-1 shows the structural information of Sample C3 (labeled as “large grain size”). Quite different from those of the other two products, the peaks in both XRD and Raman spectra become very sharp and easy to identify due to the large grain size of the material. The peaks which are unique to ε-WO_3 (JCPDS No.: 872386) become distinguishable from γ-WO_3 (JCPDS No.: 830950) for the first time. Its Raman spectrum reveals a much smaller fraction of ε-WO_3 in this product. Besides, the surface hydrate almost disappears in this product.

It can be concluded that grain size can be controlled during the FSP method. As the grain size increases, a larger fraction of ε phase of WO_3 will appear in the as-synthesized products.

Figure 3-2 shows TEM images illustrating the morphology and crystal structures of different-sized as-synthesized WO_3 products. Most particles share a spherical shape in (a) and (b). Their SAED patterns (d) and (e) are composed of a series of continuous diffraction rings indicating their nanocrystalline character. Those rings can be indexed in stable phases of WO_3. Since γ-WO_3 and ε-WO_3 are structurally similar, it is impossible to distinguish the rings from either phase. Compared to (e), the rings in (d) are more ambiguous due to the smaller size of

the product. In Image (c), we can clear observe two major shapes in “large-grain-size” product. One is small round-shaped particles with an average diameter of 50 nm and the other is huge square mono-crystals whose sizes varying from 60 nm to 300 nm. SAED patterns reveal the small particles are polycrystalline WO_3 (Image (f)) and the huge crystals are single crystalline γ-WO_3 with crystal planes either (100) or (110) (Image (g)).

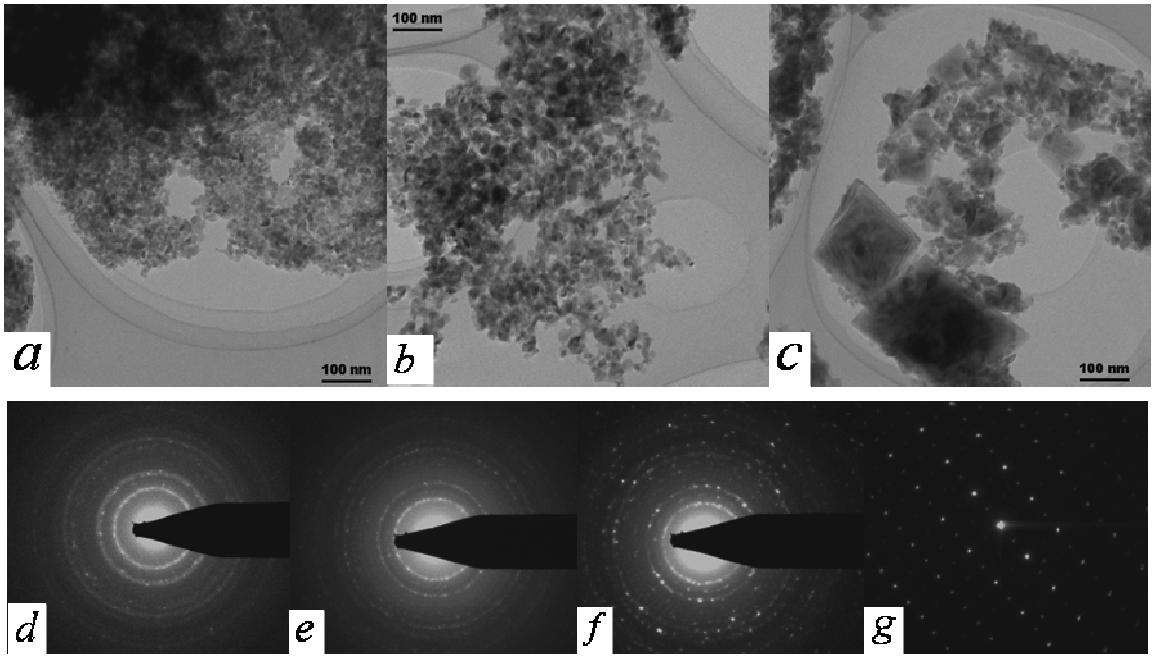

Figure 3-2 (a-c) TEM images of as-synthesized WO_3 nanoparticles and (d-g) their corresponding SAED patterns: (a) & (d) small grain size; (b) & (e) middle grain size; (c) & (f, g) large grain size.

3.1.2 Heat treatment effect

All the synthesized products were heat treated at 500 ˚c for 8 hours to let them be stable. It has been found heat treatment has a great influence on the products.

First of all, the color of the products changes to yellowish green which is the typical color of pure γ-WO_3 powders.

Second, the particles grow up. Table 3-1 shows the heat treatment effect on

the particle sizes of the as-synthesized products. The particles have grown almost twice as as-synthesized products. Such variation is also reflected in the XRD and Raman spectra in Figure 3-3 in which most peaks become much sharper.

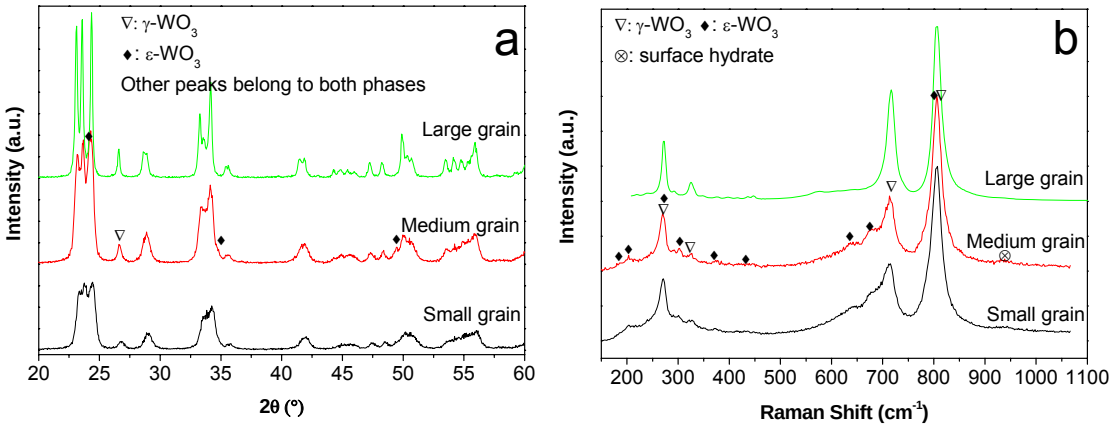

Figure 3-3 (a) XRD and (b) Raman spectra of heat-treated pure WO_3.

Finally and most importantly, after heat treatment, all pure WO_3 experiences a significant phase transition, in which the ε-WO_3 phase mostly transforms to γ phase. This is clearly shown in Figure 3-3. In the Raman spectra, the intensities of ε-WO_3 peaks have lessened a lot. In large-grain-size products, they have even disappeared at all. Table 3-1 gives quantitative results of such phase transformation.

Table 3-1 Particle size comparison of pure WO_3 before and after heat treatment.

Sample No.	SA (m^2/g)		d_{BET} (nm)		ε-WO_3 ratio	
	before	after	before	after	before	after
B1	97.0	40.2	9	21	72.4	31.6
B2	66.3	33.8	12	25		
A	63.0	33.5	13	25	69.3	32.2
C1	52.5	29.8	16	28		
C2	40.6	20.2	20	41		
C3	30.5	13.6	27	61	31.3	2.2

Figure 3-3 also proves that surface hydrates have also diminished after heat treatment. The color change results from the disappearance of both ε-WO_3 and surface hydrates.

It is clearly illustrated in Figure 3-4 that the ε-WO_3 ratio decreases along with the enlargement of particles, whether the particles are before heat treatment or after that. There is more than 70% of ε phase when the particles are around 10 nm in diameter. This percentage drops to only 2.2% when the particles grow to >60 nm. The relationship between particle size and ε-WO_3 ratio, is not linear. As the particles grow larger, the diminishing rate of ε-WO_3 becomes slower.

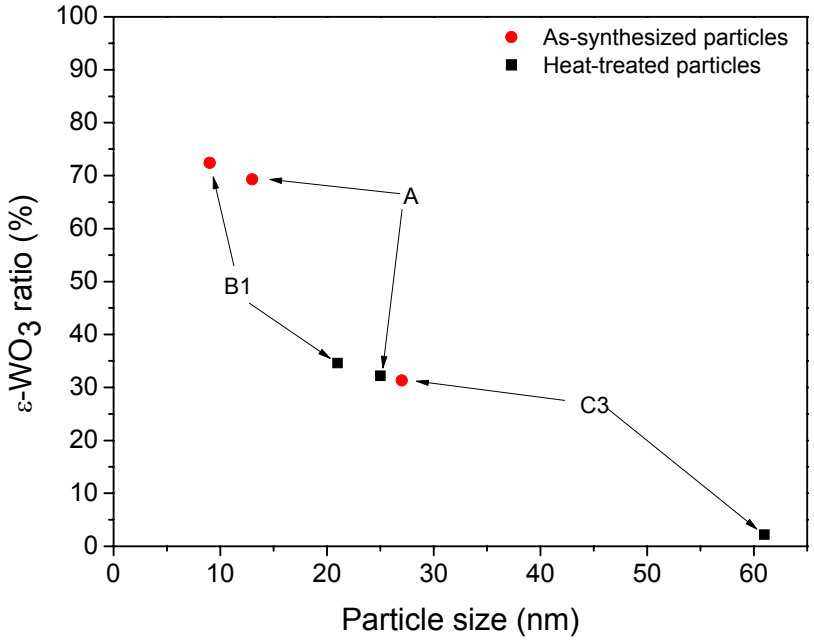

Figure 3-4 Relationship between particle size and ε-WO_3 ratio.

3.1.3 Doping effect

To study the influence of foreign dopants on the WO_3 products, two kinds of metal atoms have been added into the system, Cr and Mn. The synthesis adopts default setup parameters mentioned in Section 3.1.1 for convenience of

comparison. The medium-grain-size pure WO_3 (Sample A) will also be referred to in this section as the undoped WO_3 product during comparison.

The doping contents of Cr are 1 at%, 5 at% and 10 at%, primarily determined by precisely controlling the atomic ratio of tungstic and chromic compound precursors and examined utilizing SEM EDS spectroscopy analysis after synthesis. The comparison is shown in Table 3-2. The detection areas are up to 0.01 mm^2. The Cr content in WO_3:1at%Cr is so low that its EDS result is not very accurate. However, the EDS results of WO_3:5at%Cr and WO_3:10at%Cr products are consistent with the values in their precursors.

Table 3-2 EDS results of different Cr-doped WO_3 products.

Sample No.	Cr/W ratio (at%) in the precursor	Elemental composition by EDS (at%)			Cr/W ratio (at%) in the product
		W	Cr	O	
D1	1	26.74	0.53	72.73	1.94
D2	5	23.71	1.08	73.94	4.35
D3	10	26.56	3.12	70.32	10.5

As-synthesized Cr-doped WO_3 products turn to dark brown in color gradually as the chromium content increases. Upon heat treatment, the color becomes lighter. Figure 3-5 shows particle size comparison of different products before and after heat treatment based on BET analysis. As-synthesized undoped WO_3 has the smallest diameter (13 nm). Chromium doping slightly increases the particle size (~15 nm). After heat treatment, the size of pure WO_3 particles increased significantly (25 nm), indicating recrystallization (or phase transformation-related coarsening) during heating. In contrast, the growth of Cr-doped WO_3 is considerably smaller (~21 nm). It is also worth to mention that all the Cr-doped products have similar particle sizes either before or after heat

treatment, suggesting that chromium doping restricts the growth and change of the WO_3 particles greatly.

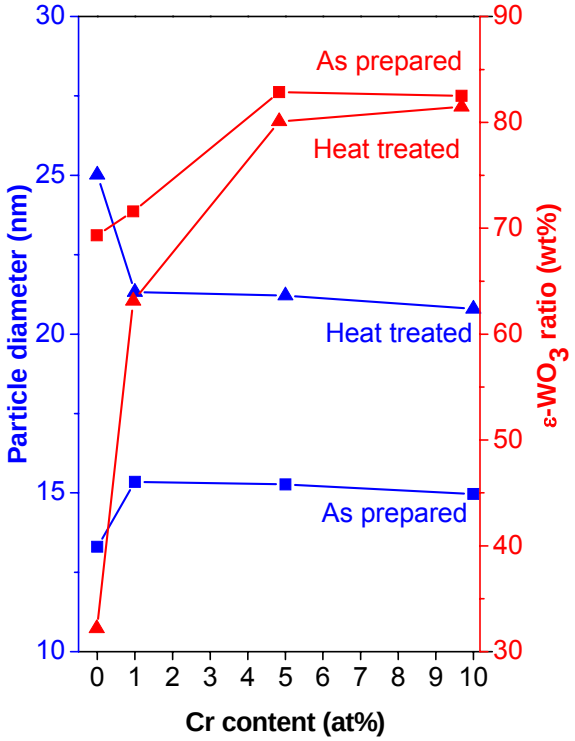

Figure 3-5 Particle diameters and *ε* phase ratios of as-prepared and heat-treated pure and Cr-doped WO_3.

Figure 3-6 shows the Raman spectra of different products before and after heat treatment. Besides *ε*-WO_3 and *γ*-WO_3 peaks as well as a W=O bond peak, an additional peak at 992 cm^{-1} appears at all Cr-doped products. Such peak can be assigned to the stretching mode of Cr=O terminal bond of dehydrated monochromates [115], revealing the existence status of chromium.

It is clear that all as-synthesized products (shown in Figure 3-6 (a)) contain a fairly high percentage of *ε*-WO_3. The *ε*-WO_3 content increases as the Cr concentration increases. In 10at% Cr-doped products, *ε*-WO_3 is the dominant phase. Quantitative results obtained from computer-assisted analysis are shown in Figure 3-5.

As we have already discussed in Section 3.1.2, after heat treatment, pure WO_3 experiences a significant phase transition, in which the *ε*-WO_3 phase mostly transforms to *γ* phase. (Figure 3-5 and Figure 3-6 (b)). The phase evolution in Cr-doped products, however, is totally different. Their Raman spectra shapes are preserved after heat treatment indicating that the *ε* phase does not change to *γ*. Such phenomenon becomes more obvious as the Cr content increases.

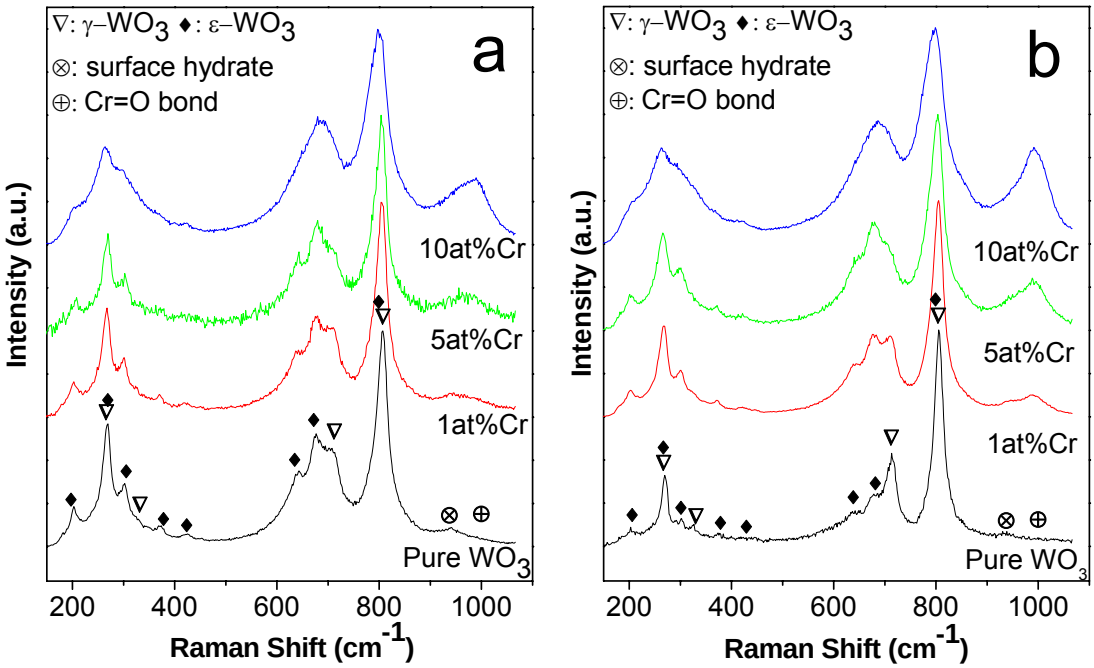

Figure 3-6 Raman spectra of (a) as-synthesized and (b) heat-treated pure and Cr-doped WO_3.

Similarly, after heat treatment, the shape of XRD spectrum of undoped WO_3 changes a lot, witnessed by the intensity rise of the peak at 26.5°, while those of Cr-doped products remain almost the same (Figure 3-7). Hence, it is suggested that the structure of WO_3 nanoparticles are determined by Cr-doping to a great extent. Furthermore, those foreign atoms impede WO_3 matrix from size or phase change. It is also evident that Cr does not form any stable compounds in either as-synthesized or heat-treated products.

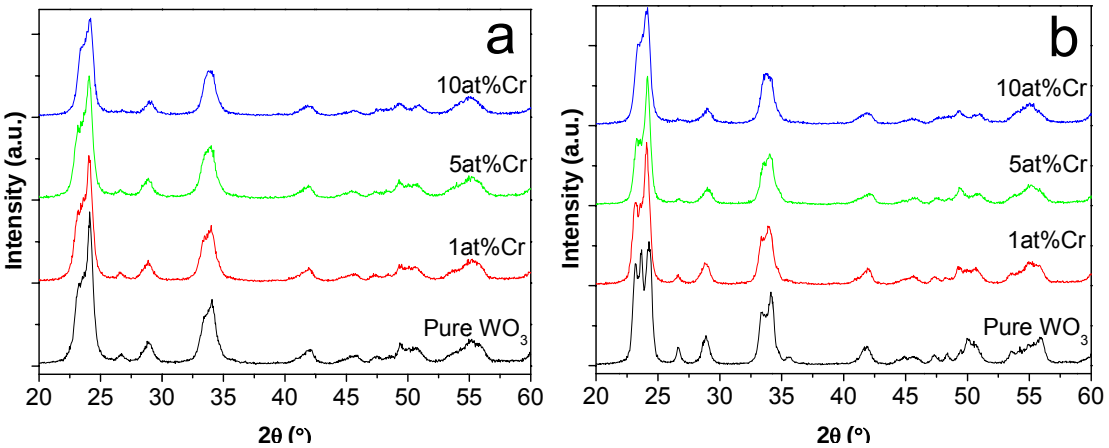

Figure 3-7 XRD spectra of (a) as-synthesized and (b) heat-treated pure and Cr-doped WO_3.

TEM images are included in Figure 3-8 illustrating the crystal structure and morphology of heat-treated 10at% Cr-doped WO_3 particles in detail. Like undoped WO_3, the particles share a spherical shape and the SAED inset is also similar to undoped products (Figure 3-2). The lattice fringes are also clearly visible in the HRTEM image indicating its excellent crystalline character. No Cr-related stoichiometric compounds have been found in the products.

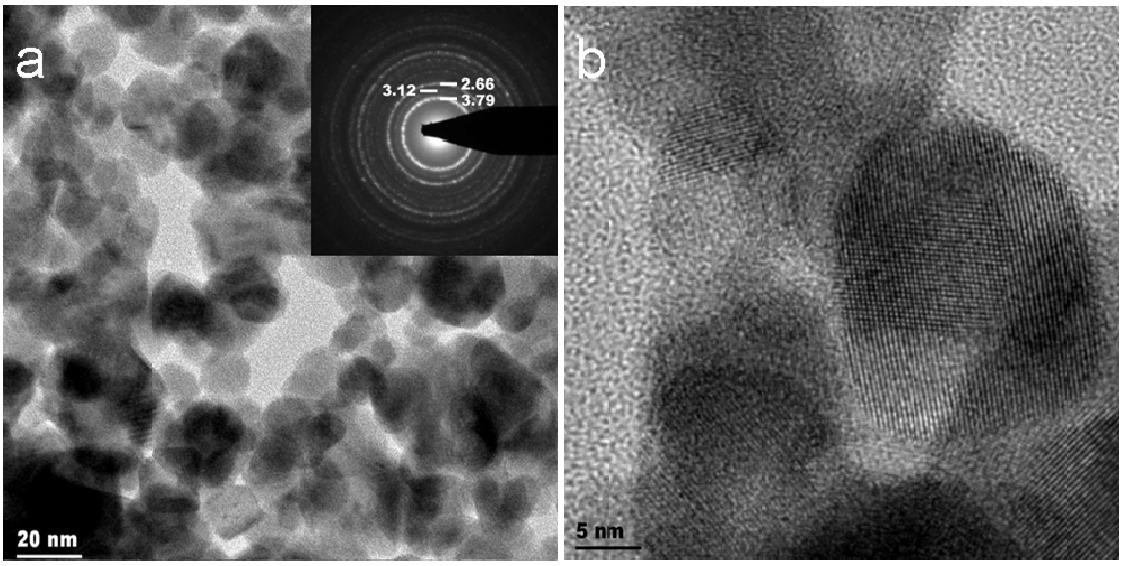

Figure 3-8 (a) TEM (inset: SAED pattern) and (b) HRTEM images of heat-treated 10at% Cr-doped WO_3.

According to the above results, the influence of Cr doping on WO_3 structures is significant. This drives us to study the influence of other dopants. Especially, Mn has been added into the system.

For Mn-doped products, the color changes to grey. (Sample E1 and E2) As the concentration increases, the color gets darker. The XRD spectra (Figure 3-9 (a)) and the Raman spectra (Figure 3-10 (a)) of as-synthesized products are somewhat similar to those of Cr-doped WO_3 (Figure 3-6 (a), Figure 3-7 (a)). *ε*-WO_3 is the dominant phase in every Mn-doped WO_3, whose percentage is larger than that in pure WO_3. (See Table 3-3 for quantitative results) In addition, no obvious Mn-contained compounds are found in as-synthesized materials.

Table 3-3 Particle size and phase composition comparison of Mn-doped WO_3 before and after heat treatment.

Mn	SA (m^2/g)		d_{BET} (nm)		*ε*-WO_3 ratio (%)		$MnWO_4$ ratio (%)	
content	before	after	before	after	before	after	before	After
0	63.0	33.5	13	25	69.3	32.2	0	0
1	68.2	28.0	12	29	80.4	27.3	0.67	0.37
10	68.1	34.3	12	24	77.3	55.0	5.05	10.6

However, after heat treatment, the Mn-doped products have experienced an entirely different phase revolution from Cr-doped products. First of all, *ε*-WO_3 related peaks in Raman spectra weaken dramatically (Figure 3-10 (b)), indicating that the *ε* phase has transformed to the *γ* phase. The sharpening of XRD peaks (Figure 3-9 (b)) also proves the growth and recrystallization of the particles. What is more important, the peaks at 18.4°, 29.9° and 30.3° in XRD spectra clearly reveals the formation of a second phase which can be identified as monoclinic $MnWO_4$ (JCPDS file No.: 74-1497). In consistency, a very sharp $MnWO_4$ peak

appears at 883 cm^{-1} in the Raman spectra. [116, 117]

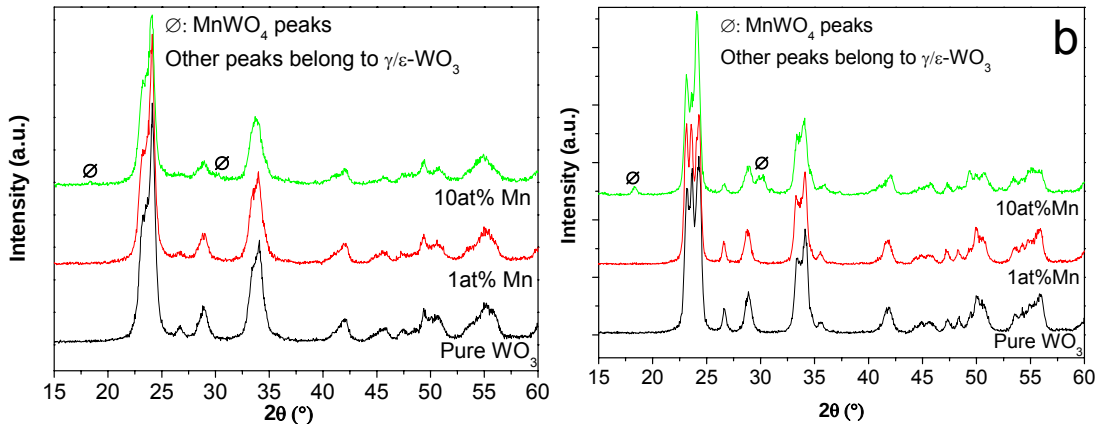

Figure 3-9 XRD spectra of (a) as-synthesized and (b) heat-treated pure and Mn-doped WO_3.

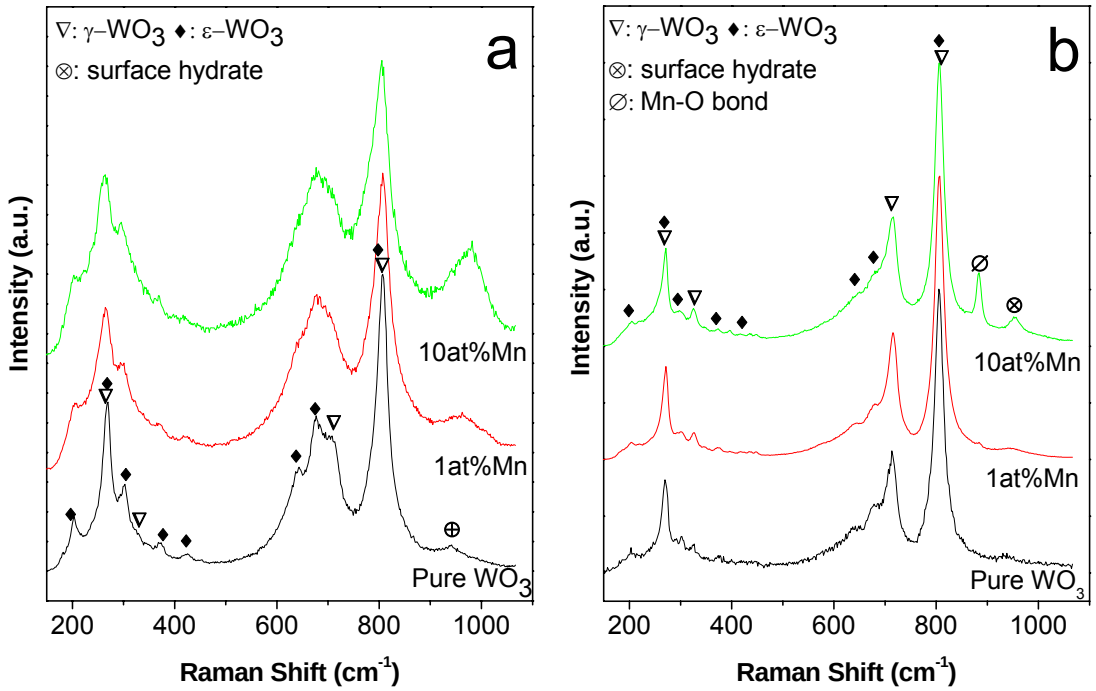

Figure 3-10 Raman spectra of (a) as-synthesized and (b) heat-treated pure and Mn-doped WO_3.

$MnWO_4$ whose mineral name is hübnerite, has a wolframite type of structure (space group *P2/c),* in which edge-sharing [MnO_6] and [WO_6]

octahedron units form zigzag chains along the *c*-axis and tungsten atoms and Mn atoms are arranged in alternating sheets parallel to (100). [118] It is a kind of multiferroic materials which combine magnetism and ferroelectricity [118] and it is found to be highly sensitive to humidity. [119] Quantitative analysis (Table 3-3) reveals that in heat-treated 10 at% Mn-WO_3, the percentage of *ε*-WO_3 reduces to 55 at%. Furthermore, the percentage of $MnWO_4$ is 10.6 at%, indicating that almost all the Mn atoms exist in this compound.

It can be concluded that Mn doping contributes to the formation of *ε*-WO_3. However, after annealing, Mn dopants crystallize and form a second phase, $MnWO_4$ which cannot prevent the growth and phase transition of the nanoparticles.

3.1.4 Mechanism of *ε*-WO_3 formation

Since *ε*-WO_3 is usually stable below -40 °C, its appearance of here is surprising. Possibly captured as a metastable phase during the rapid heating and cooling of the FSP process, [110] the *ε* phase is stabilized by Cr-dopant which prevents formation of symmetric structures in the products.

As we have already mentioned in Section 1.4, WO_3 typically undergoes several phase transitions from *α* to *ε* phase as it cools down. Although these phases share a similar cubic ReO_3 structure, the symmetry is lowered at each phase transition. It seems that monoclinic *ε*-WO_3 might be more symmetric than triclinic *δ*-WO_3; nevertheless, considering that *ε*-WO_3 is acentric, which means W atoms are not located in the centers of [WO_6] octahedron units, it has the lowest symmetry of all other polymorphs. [45]

The reaction and particle formation processes during FSP are so fast that tungsten and oxygen atoms probably do not have enough time to settle in their thermodynamically-dictated positions. As a result, particles tend to grow in the form of the lowest symmetric structure, the *ε* phase. We consider only those methods involving rapid growth of nanoparticles, e.g. the FSP method in this report, and the gas evaporation method in Ref. [47], are able to produce the *ε* phase. The smaller those particles are, the more defects and deformations emerge and the more difficultly the particles form symmetric structures, finally leading to an increasing ratio of *ε* phase in the as-synthesized products. Figure 3-5 clearly demonstrates such relationship. Pure WO_3 particles whose average size is less than 10 nm contain more than 70% *ε*-WO_3. When the particles increase to 60 nm in diameter, the *ε* phase disappears almost completely.

During annealing, the materials have enough time to recrystallize, grow and are able to reform into the more symmetric *γ* phase, the stable phase of WO_3 at RT. Therefore, after heat treatment, the particles become twice larger and the *ε* phase has lost its dominance.

However, the addition of Cr introduces distortion into the WO_3 matrix, repelling tungsten atoms from centric positions in WO_6 octahedra. This could explain why the *ε* phase content increases with increasing amount of Cr-doping. In addition, the majority of Cr atoms exist in the form of Cr=O terminal bond, according to Raman spectroscopy. This implies that Cr atoms favor attachment on the particle surface to form chromates (Figure 3-11). This is in perfect agreement with Weckhuysen *et al.* who studied surface Cr atoms on inorganic

oxides [115] and Jimenez *et al.* who studied Cr-doped *γ*-WO_3 powders [120].

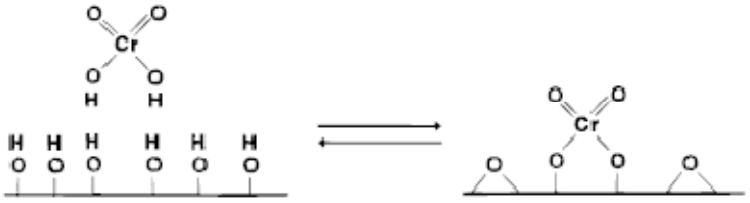

Figure 3-11 Reaction of Cr with the hydroxyl groups and formation of a dehydrated monochromate.*

If there are enough Cr atoms, those chromates form a layer on the surface of each WO_3 nanoparticle. Such layer would prevent particles from changing size or structure even during the annealing process. This is in accordance with Vemury *et al.* who observed Si-doping of TiO_2 via FSP method preventing its transformation from anatase to the more dense rutile phase.[121]

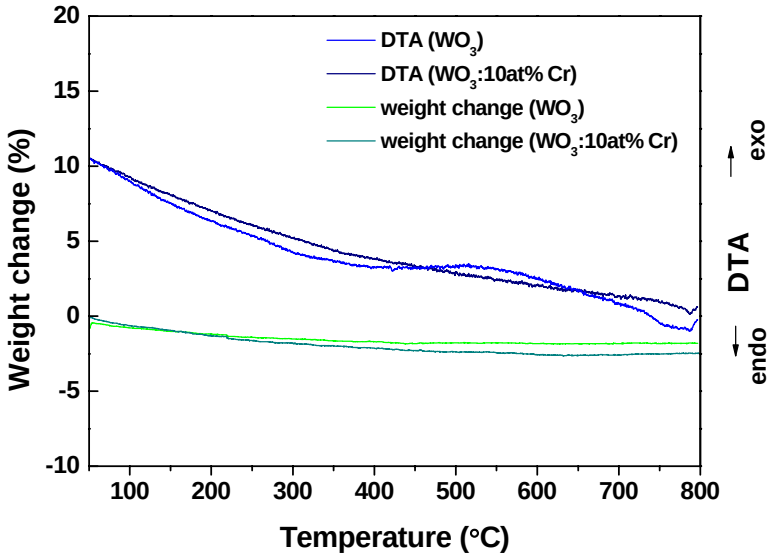

Figure 3-12 TG-DTA curves of heat-treated pure and 10at% Cr-doped WO_3.

Thermal analysis (TG-DTA) has confirmed the high temperature phase stability of Cr-doped WO_3 whose results are shown in Figure 3-12. A small sharp

* Reprinted with permission from Chemical Reviews (Ref. [115]). Copyright 1996, American Chemical Society.

endothermal peak at around 780˚C appears on both DTA curves corresponding to the formation of *α*-WO_3 phase. On the DTA curve of pure WO_3, there is also an endothermal peak around 350˚C most likely corresponding to the phase transition from *γ*-WO_3 to *β*-WO_3. Such results indicate that the Cr-doped sample does not undergo any obvious phase transition up to 700˚C.

Unlike Cr element, Mn atoms favor growing stable compound $MnWO_4$ rather than forming surface layer. Although Mn atoms do not have time to settle down during the ultrafast FSP process, they are able to recrystallize and form new compound during the follow-up heat treatment. In fact, the existence of $MnWO_4$ was already reported by Blo *et al.* [75], in which pure WO_3 powders were prepared through a partially modified sol–gel route and then impregnated with $MnCl_2 \cdot 4H_2O$ in ethanol. The newly formed $MnWO_4$ are mixed with pure WO_3 and does not have a protection effect on the *ε* phase at all.

In summary, when foreign atoms exists, if these atoms tend to form stable secondary compounds upon recrystallization, such as the formation of $MnWO_4$ in Mn-doped WO_3, *ε*-WO_3 will still transform to *γ*-WO_3. However, if those foreign atoms tend to form a surface layer around the material, such as the chromate layer in Cr-doped WO_3, such layer may prevent the above-mentioned transition from occurring. In this way, this *ε*-WO_3 is able to preserve its phase above RT.

3.2 Sensing properties

To investigate the sensing properties of produced *ε*-WO_3, Three representative samples were chosen: pure medium-sized WO_3 (Sample A), 1 at% Cr-doped WO_3 (Sample D1) and 10 at% Cr-doped WO_3 (Sample D3). All the

samples have been heat treated because the gas sensing tests were performed at elevated temperatures: 150 °C and 350 °C. Their particle sizes are in the range of 20-25 nm and their ε-WO_3 percentages are 32%, 63% and 81%, respectively (Figure 3-5).

A total of ten gases/VOCs were tested, including two oxidizing gases: NO_2, and NO, two reducing inorganic gases: NH_3 and CO, three hydrocarbons: ethane, isopentane, and isoprene, and three oxygen-contained VOCs: ethanol, methanol, and acetone. These gases are the most common trace gases in human breath, whose detailed information is shown in Table 1-1.

The gas concentrations in our tests were set at 0.2 ppm, 0.5 ppm and 1 ppm. Generally speaking, the concentrations of those trace gases in human breath are within this range in most cases.

3.2.1 Sensing comparison

When surrounded by oxidizing gases, the resistance of all the three sensors goes up. In contrast, their resistance will increase when the materials are faced to other reducing gases. Such results indicate all the materials are n-type semiconductors. This is in consistence with reported pure γ-WO_3.

Figure 3-13 shows the sensing response comparison of the three different materials at 350 °C. For pure WO_3 (32% ε-WO_3, shown in Figure (a)), the sensor has the highest sensitivity to isoprene, (S=4.8; ; 1 ppm gas, the same hereinafter) then acetone (S=4). The sensitivities to NH_3(S=3.5), NO_2(S=2.9), and isopentane (S=2.9) are also very high. The material is a little less sensitive to two alcohols, ethanol (S=1.5) and methanol (S=2.3) as well as NO (S=1.8). Pure WO_3 has little

response to CO and ethane.

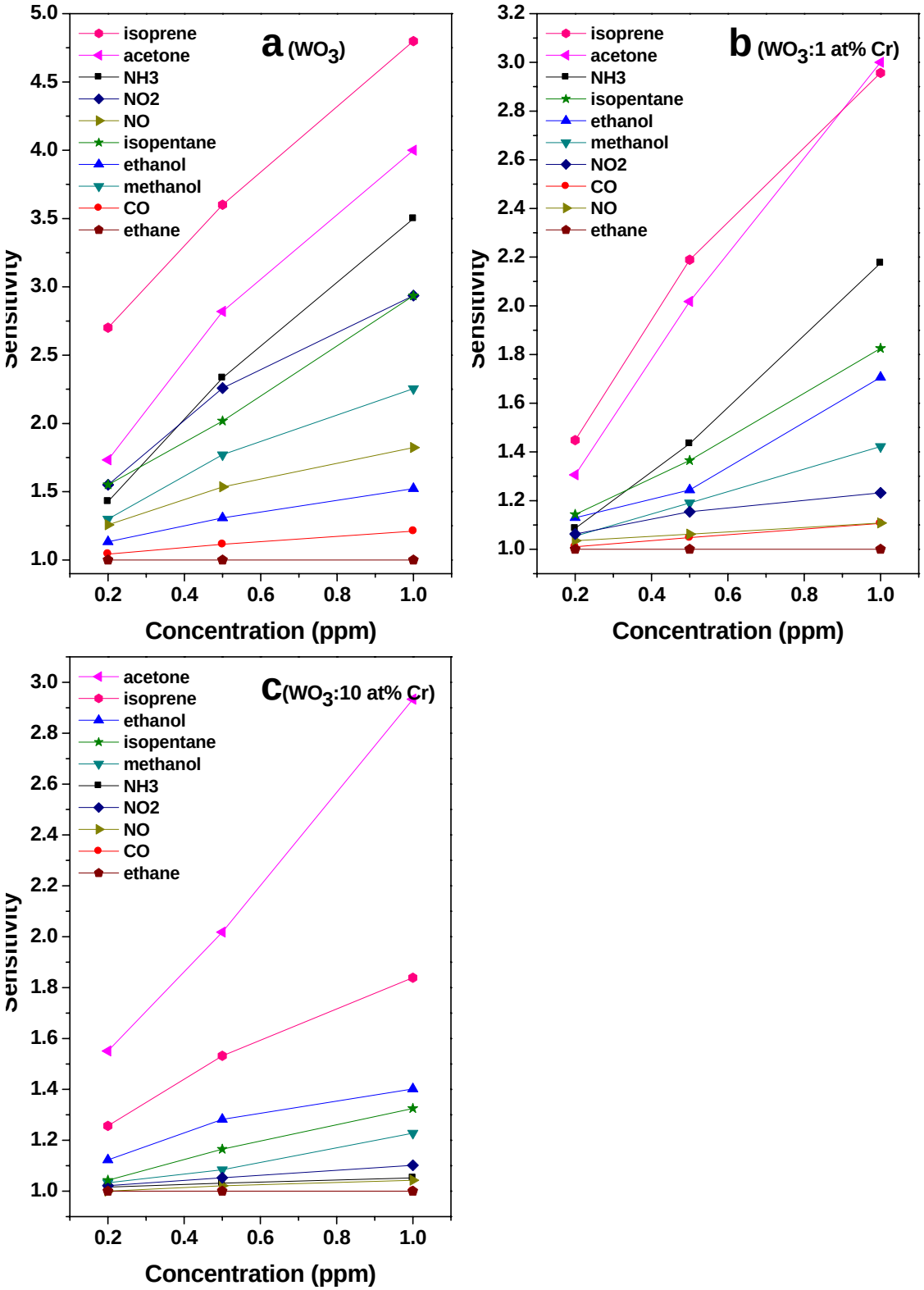

Figure 3-13 Sensing comparison of three samples with different ratios of ε-WO_3. * indicates it is a positive response.

1 at% Cr-doped WO_3 still has the similarly highest relative sensitivity to acetone and isoprene, although the absolute value decreases (*S*=3). The sensitivity to NH_3 also falls down (*S*=2.2). The same thing occurs on isopentane (*S*=1.8) Its responses to two nitrogen oxides, NO_2 (*S*=1.2) and NO (*S*=1.1) decline dramatically. In contrast, the sensitivities to ethanol (*S*=1.7) and methanol (*S*=1.4) do not change very much.

The sensor's response to acetone keeps almost consistent in 10 at% Cr-doped WO_3, with the sensitivity of 2.9. The sensitivity to isoprene falls down to 1.8. The attenuation of response to NH_3 is dramatic, less than most other gases (*S*=1.05). The sensor also shows little response to NO_2, NO, CO and ethane. The most significant phenomenon in this figure is the sensor has a much higher sensitivity to acetone compared to any other gases. The sensor sensitivities to 1 ppm of these gases are even lower than that of 0.2 ppm of acetone.

3.2.2 *ε*-WO_3 as acetone selective sensor

The above results suggest that 10 at% Cr-doped WO_3 has a very good selectivity to acetone at 350 °C and may serve as an excellent acetone sensor. Figure 3-14 shows the change in electrical resistance of that sensor to acetone exposure. The sensitivities are 3, 2 and 1.5 corresponding to 1, 0.5 and 0.2 ppm of acetone. Such sensitivity could be attributed to the relatively small size and covers well the detection requirements of acetone in human breath with concentrations of <0.8 ppm for a healthy person and >1.8 ppm for a diabetic patient. When consecutive cycles of acetone gas flows were introduced, the sensitivity did not change indicating good stability of the sensor. In addition, the

sensor responds to acetone exposure very fast, in less than 30 seconds. The recovery time, however, is longer, up to 150 seconds.

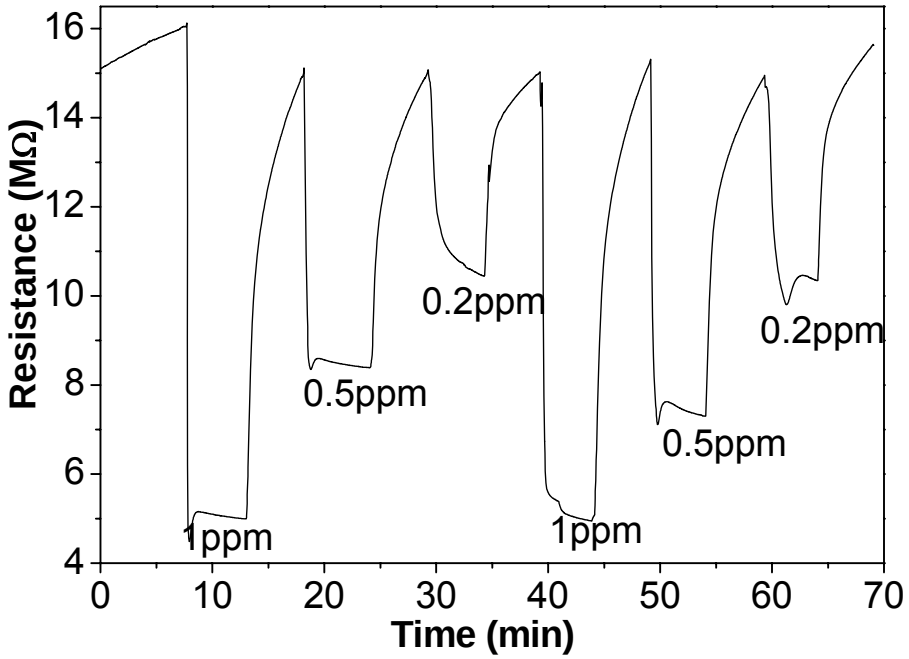

Figure 3-14 Resistance change of 10at% Cr-doped WO_3 with exposure to acetone at 350 °C.

Figure 3-15 shows the relationship between acetone concentration and ε-WO_3 from 0.2 ppm to 2.0 ppm. The concentration of acetone in most human breath falls into this range. In particular, at 1.8 ppm, which is set as diabetes diagnosis threshold, the sensitivity is 4.3. This value will be used in future breath analyzer design.

There is an approximately linear relationship between *C* and *S* in this diagram, which can be expressed as:

$$S = 1.19 + 1.68C \tag{13}$$

The unit of *C* is ppm and *S* is normalized sensitivity (R_0/R_g). This equation could be used to estimate the concentration of acetone according to the

resistance change of the sensor. However, it is only an empirical formula and could only be used within the range of 0.2 ppm to 2 ppm.

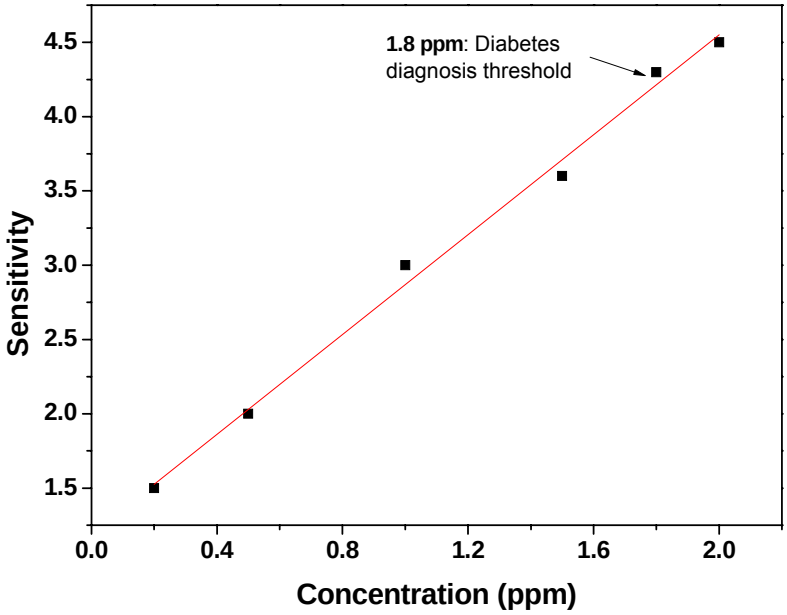

Figure 3-15 Relationship between acetone concentration and sensitivity.

3.2.3 Discussion on acetone detection

As we introduced in Section 1.1.1, acetone is the biomarker for diabetes diagnosis. It is convenient to conclude from the above results that ε-WO_3 nanoparticles show selective detection on acetone. Such detection is sensitive, fast and repeatable. Therefore, it has great potential to serve as non-invasive diabetes monitors.

Acetone detection using chemi-resistive sensors was reported before. For example, Ryabtsev *et al.*'s Fe_2O_3, SnO_2 CdO sensors [122] showed sensitivities less than 5.2 to 10 ppm acetone and they didn't test the selectivity. The sensitivity of Li *et al.*'s WO_3 hollow-sphere gas sensors was only 3.53 to 50 ppm acetone. [123] Zhu's *et al.*'s TiO_2-doped ZnO thick film had cross sensitivity to many other VOCs. [124] Teleki *et al.*'s TiO_2 nanoparticles had cross sensitivity to

isoprene. [111] Khadayate *et al.*'s WO_3 thick film had the sensitivity as low as 4.5 to 50 ppm acetone and they didn't test other gases [125]. Similarly, metal oxide sensors reported in other works [126-129] either lacked satisfying sensitivity to low concentrations of acetone or had cross sensitivity to other gases. Compared to those materials, our *ε*-WO_3 has the advantage of both high sensitivity and good selectivity, which is a breakthrough in acetone detection.

Acetone is a reducing gas. Its sensing mechanism involves with physisorption, chemisorption, and electron transfer processes. Since W^{6+} and Cr^{6+} ions are strong Lewis acids, they tend to easily adsorb acetone molecules which is Lewis base:

$$(CH_3)_2C=O\,(g) + W^{6+}(s) \longrightarrow (CH_3)_2C=O \cdots W^{6+}(a) \tag{14}$$

In this and the following equations, g means gas molecules; s means surface state; a means adsorbate species.

Surface acetone reversibly transfers to its isomer, enolate, which can react further with another acetone molecule to yield mesityl oxide:[130, 131]

$$(CH_3)_2C=O \cdots W^{6+}(a) \rightleftharpoons CH_2=C(CH_3)OH \cdots W^{6+}(a) \tag{15}$$

$$\begin{gathered} CH_2=C(CH_3)OH \cdots W^{6+}(a) + (CH_3)_2C=O\,(g) \\ \longrightarrow (CH_3)_2C=CH-C(CH_3)=O \cdots W^{6+}(a) + H_2O \end{gathered} \tag{16}$$

Chemisorption and accompanying electron transfer occur afterwards: [132]

$$(CH_3)_2C=O \cdots W^{6+} + W-O^-(s) \rightarrow (CH_3)_2C\begin{matrix}\nearrow^{O-W}\\ \searrow_{O-W}\end{matrix}(a) + e^- \tag{17}$$

$$\begin{gathered} CH_2=C(CH_3)OH \cdots W^{6+}(a) + W-O^-(s) \\ \rightarrow CH_2=C(CH_3)-OW\,(a) + HO-W(a) + e^- \end{gathered} \tag{18}$$

The above reaction processes still cannot explain the selectivity to acetone. Recently, attention has been paid on the surface chemistry of ferroelectric

materials. Although conclusive theories have not been established, research based on $LiNbO_3$ and some other materials has shown strong evidence that the dipole moment of a polar molecule may interact with the electric polarization of some ferroelectric domains on the surface [133-135]. This interaction would then increase the strength of molecular adsorption on the material surface.

Here, it is suggested that the acentric structure of ε-WO_3 plays an important role on the selective detection of acetone. The ε-WO_3 is a type of ferroelectric material which has a spontaneous electric dipole moment. The polarity comes from the displacement of tungsten atoms from the center of each [WO_6] octahedra. On the other hand, acetone has a much larger dipole moment than any other gas (Table 3-4). As a consequence, the interaction between the ε-WO_3 surface dipole and acetone molecules could be much stronger than any other gas, leading to the observed selectivity to acetone detection.

Table 3-4 Dipole moments and sensitivities of 10 at% Cr-doped WO_3 to different gases and VOCs.

Gas	Dipole moment	Sensitivity		
		0.2ppm	0.5ppm	1ppm
Acetone	2.88D	1.55	2.05	2.90
Ethanol	1.69D	1.08	1.15	1.32
Methanol	1.70D	1.03	1.10	1.23
NO	0.159D	1	1.05	1.09
NO_2	0.316D	1	1.04	1.07
NH_3	1.471D	1.02	1.03	1.05
CO	0.112D	1	1	1
Ethane	0	1	1	1
Isoprene	0.25D	1.26	1.53	1.84
Isopentane	0.105D	1.04	1.16	1.33

Ethanol and methanol gases have lesser dipole moments than acetone and the sensitivities to these two gases are lower than acetone but higher than most

other gases. NO, NO_2, CO and ethane have very small dipole moments and *ε*-WO_3 is inert with these gases.

Exceptions occur on NH_3, isoprene and isopentane gases. The dipole moment of NH_3 is comparable to ethanol and methanol, but *ε*-WO_3 is not sensitive to this gas at all. In contrast, isoprene and isopentane exhibit rather weak dipole moments, but ε-WO_3 has a strong interaction with these two gases, esp. isoprene. Actually, both *γ*-WO_3 and *ε*-WO_3 are quite sensitive to isoprene and *γ*-WO_3 is more although is has a cross sensitivity to acetone. In the next chapter, we will observe another metastable phase of WO_3, the hexagonal phase, is more sensitive and also selective to isoprene. Such result has not been reported by other research groups. It is predictable that there is a unique mechanism underlying the sensitive reaction between isoprene WO_3 materials. Unfortunately, the adsorption of isoprene on metal oxide surfaces has been rarely studied before and such mechanism still remains unclear yet. Therefore, the study of adsorption and sensing process between isoprene and WO_3 is highly recommended in the future work.

CHAPTER 4 *h*-WO_3: Characterization and sensing properties

4.1 Morphology and structure

The color of the synthesized *h*-WO_3 is grey, different from that of *γ*/*ε*-WO_3, which is yellow-green. The morphology of the products is shown in Figure 4-1.

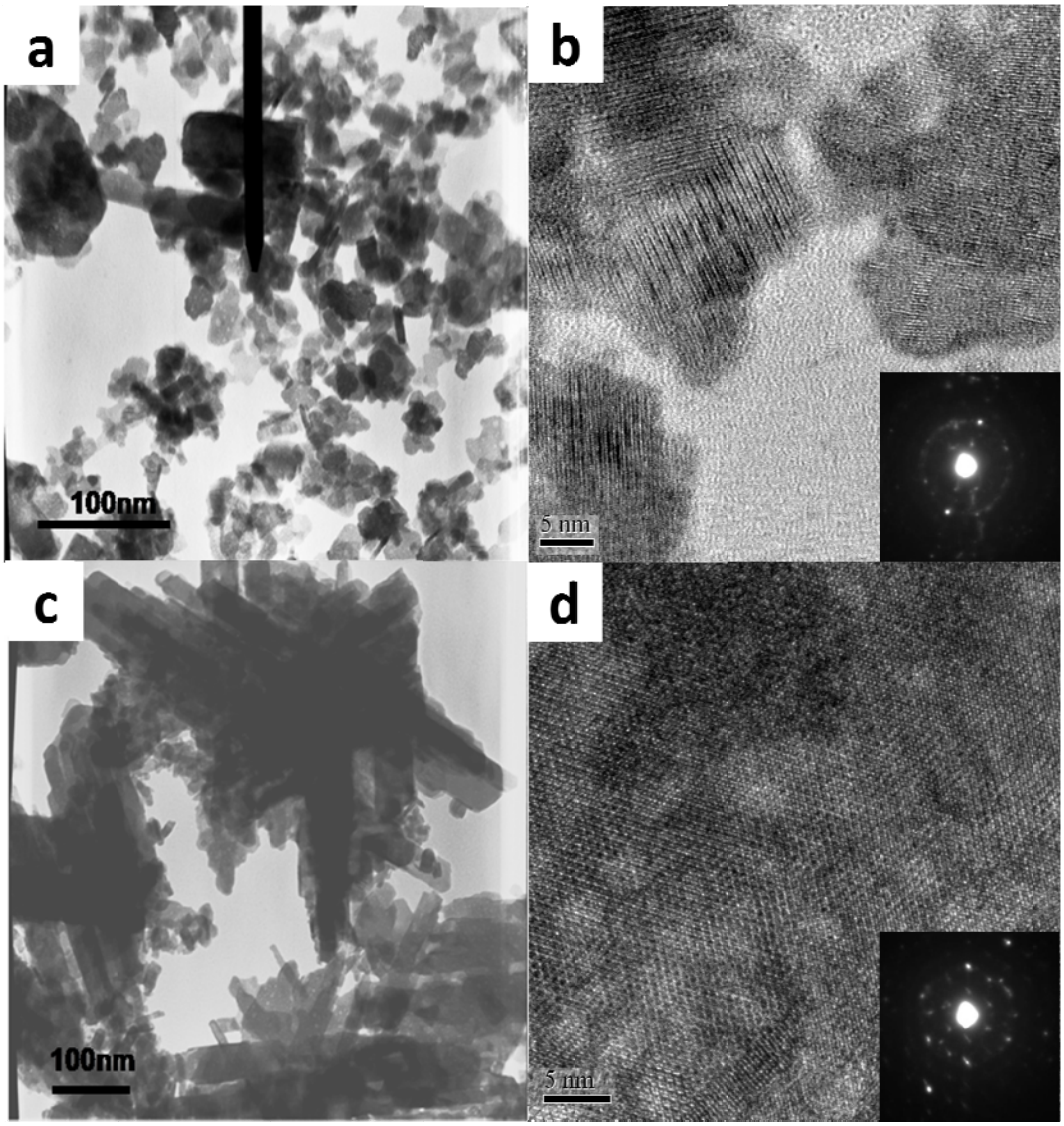

Figure 4-1 Morphology and structure of *h*-WO_3 powders: (a) TEM image, (b) HRTEM image (inset: SAED) of nanoparticles, (c) TEM image and (d) HRTEM image (inset: SAED) of nanorods.

There are typically two shapes of grains; one is equiaxed particles and rod-shaped particles. These two shapes are mixed together and the rods are in the majority. The morphology of equiaxed particles is shown in Figure 4-1 (a). There is a certain diversity of the diameter distribution, from 20-50 nm, with an average value of 35 nm. The HRTEM image (b) and the SAED pattern indicate those particles are polycrystalline which can be indexed in *h*-WO_3 structure. The sizes of the rod-shaped particle shown in Figure 4-1 (c), however, are much larger. The diameters of the rods are 30-100 nm with the average value of 50 nm and their lengths are up to 100-300 nm, with the average value of 200 nm. The HRTEM image clearly records the lattice of *h*-WO_3 (001) planes with an interplanar spacing of about 0.39 nm, indicating the WO_3 rods are single crystalline in most regions and grow along the [001] direction, which is in accordance with SAED pattern.

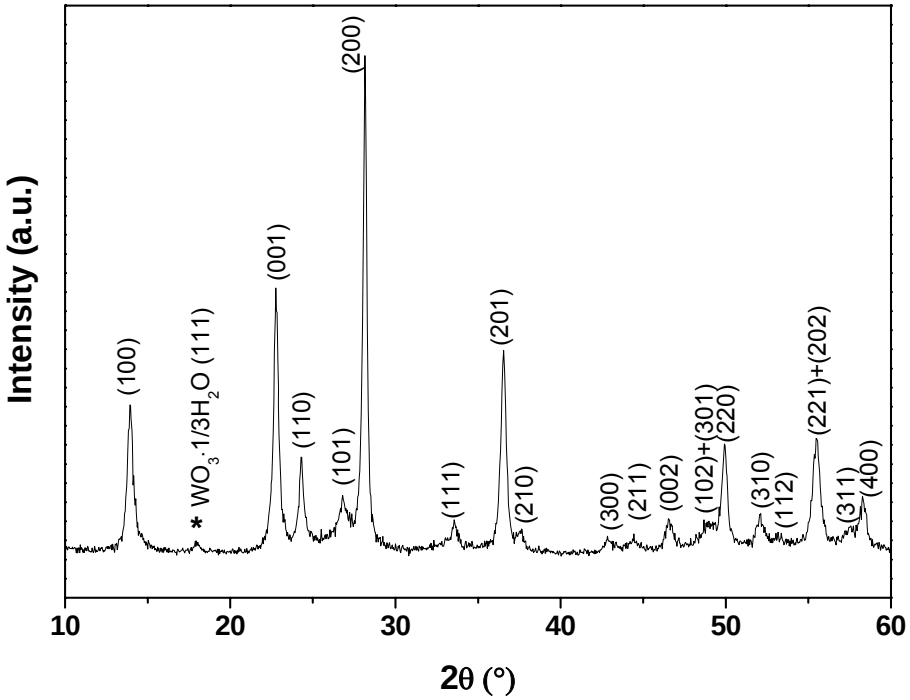

Figure 4-2 XRD result of synthesized *h*-WO_3 powders.

The structure of synthesized products has been further determined by XRD, whose result is shown in Figure 4-2. Most peaks can be indexed to a hexagonal WO_3 structure (JCPDS No.: 75-2187) except a small peak around 18˚ indicating the existence of $WO_3 \cdot \frac{1}{3}H_2O$ residuals. The calculated lattice parameters are a=7.301 Å, c=3.897 Å and the grain size is 27.1 nm. As mentioned in Section 1.4.4, there are two types of *h*-WO_3 with slightly different lattice parameters, characterized by Gerand *et al.* (JCPDS No.: 75-2187) and Oi *et al.* (JCPDS No.: 85-2460), respectively. Our result is in good accordance with Gerand's.

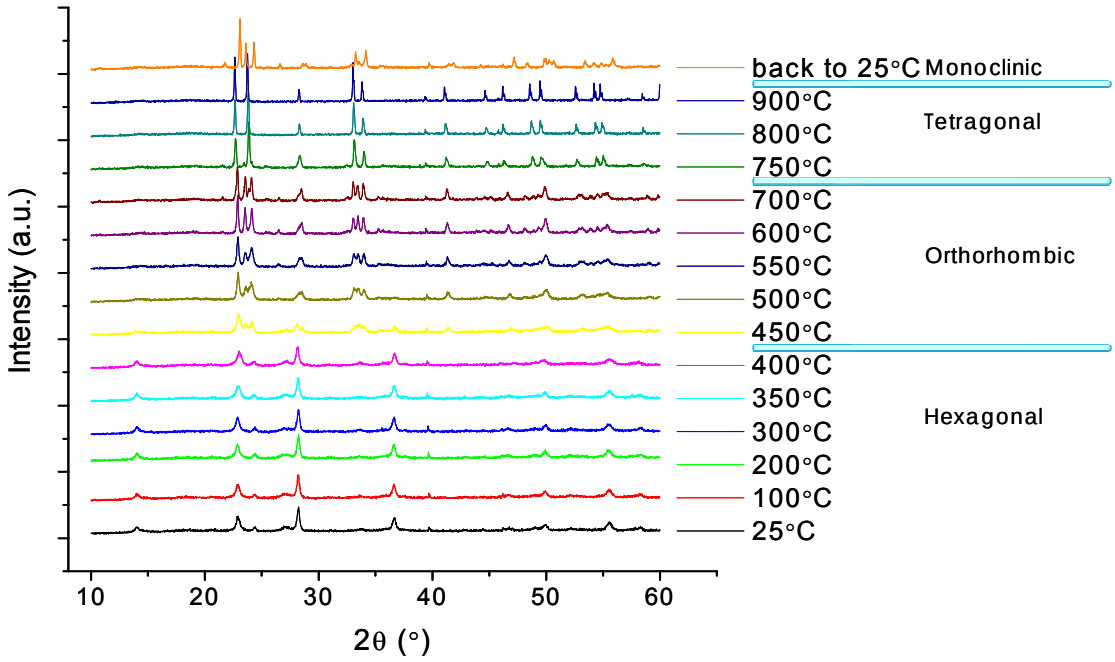

Figure 4-3 In-situ XRD measurement of *h*-WO_3 from RT to 900 ˚C.

If we heat the product from RT to 900 ˚C and then cool it down to RT, the powders will experience phase transformations for several times (Figure 4-3), from hexagonal to orthorhombic between 400-450 ˚C, then tetragonal between 700-750 ˚C. However, if the temperature cools down to RT again, the powders won't go back to hexagonal phase but monoclinic phase. This result shows the

metastable character of *h*-WO_3.

Figure 4-4 shows the Raman spectrum of the synthesized *h*-WO_3. As reported by Daniel *et al.*[114], the Raman shifts at 813 cm^{-1} and 688 cm^{-1} belong to the W–O stretching modes while 249 cm^{-1} and 318 cm^{-1} belong to W-O-W bending modes in *h*-WO_3. The peak at 942 cm^{-1} belongs to W=O stretching modes which is due to the existence of $WO_3 \cdot \frac{1}{3}H_2O$.

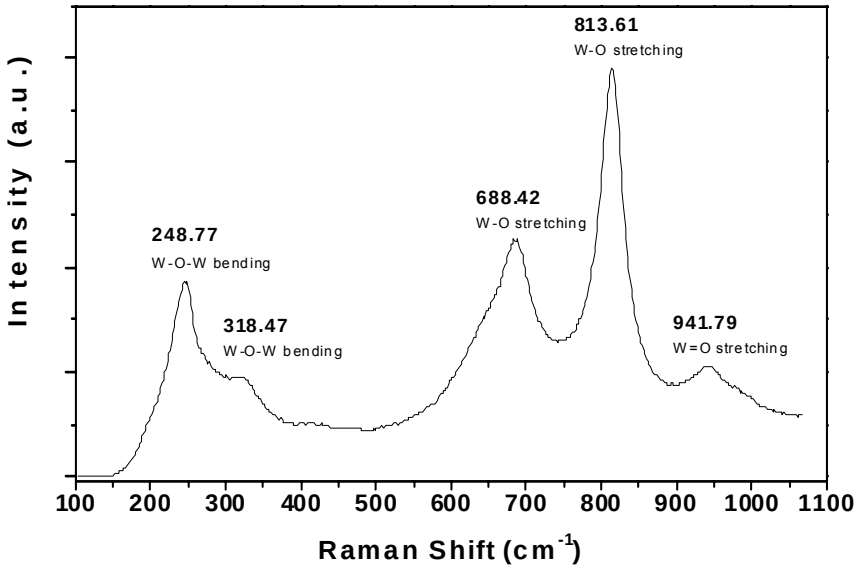

Figure 4-4 Raman spectrum of *h*-WO_3.

To determine surface oxidation states of W atoms, XPS analysis was performed on this sample. Besides O atoms (O1s = 530.7 eV), W atoms were detected in three oxidation states (shown in Figure 4-5). Besides the most prominent W^{VI} atoms ($W4f_{7/2}$=36.9 eV and $W4f_{5/2}$=34.8 eV), a certain fraction of W^{V} ($W4f_{7/2}$=35.9 eV and$W4f_{5/2}$=33.5 eV) and WIV ($W4f_{7/2}$=35.2 eV and $W4f_{5/2}$=33.2 eV) atoms also exists. [136] Quantitative analysis shows the percentage of the three oxidation states is W^{VI}:W^{V}:W^{IV}=97.1:1.6:1.3. A very small fraction of Na atoms (Na1*S*=1076 eV) also appears. The atomic percentage of

these three elements is Na:W:O=5.4:21.4:73.2.

Since the method followed in this paper starts from Na_2WO_4, it is very normal to detect residual Na atoms in the final products. These atoms are believed to go into the interstitial sites like sodium tungsten bronzes (Na_xWO_3) and won't influence the structure very much due to their low density.

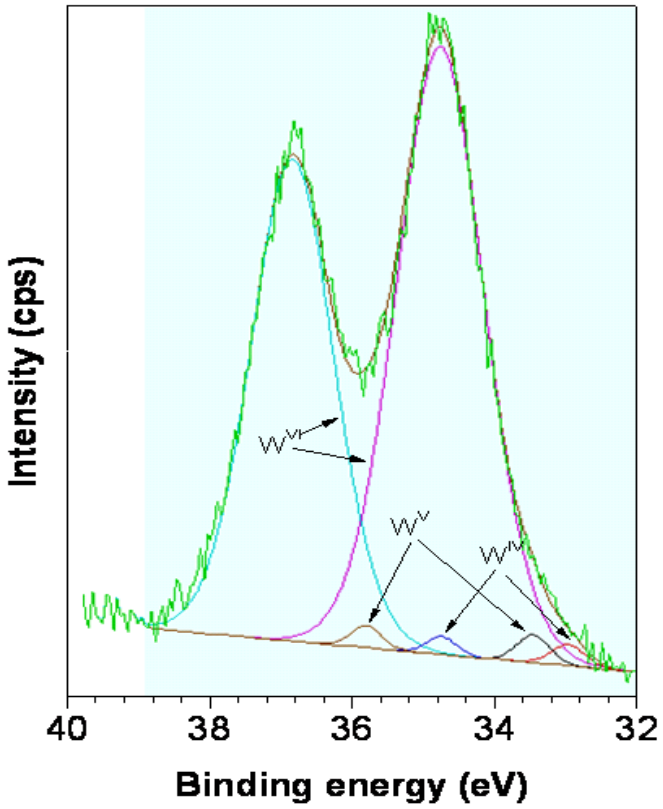

Figure 4-5 XPS spectrum of *h*-WO_3 showing the oxidation states of W.

It should be paid attention to that the W:O ratio on the surface is 1:3.42, far less than the required ratio of 1:3 to form stoichiometric compounds. This result indicates excessive oxygen atoms have been attached on the surface of *h*-WO_3, which may have influence on its sensing behaviors.

4.2 Sensing properties

The responses of *h*-WO_3 to 1 ppm of different gases at 150 °C, and 350 °C were investigated. It is observed that this material shows different sensing behaviors to different gases and at different temperatures.

4.2.1 Sensing comparison at 150 °C

At 150 °C (Figure 4-6), the responses to methanol, ethane, isopentane, NH_3, and CO are quite small. More importantly, when the material meets those reducing gases, the resistance goes up sharply first, at most 1.5 times as high as the baseline, then slowly goes down to its baseline. This implies there is an n-p transition in this material. After those gases are removed, the sensor's resistance almost keeps constant at baseline. The overall variation of the sensor's resistance from response period to recovery period is very small, indicating that the sensor is quite inert to those gases.

Acetone, ethanol and isoprene lead to higher responses. When the sensor encounters these gases, its resistance also rises first, but the amplitude is much smaller. Then the resistance keeps decreasing to a value lower than baseline. The sensitivities to ethanol, acetone, and isoprene are 1.6, 2, and 2.5 respectively. The response times are ~20 min in each case. After we switch the surrounding gas to air, the sensor slowly goes back to its baseline, another ~20 min taken.

Compared to other gases, the sensor shows positive responses to oxidizing NO_2 and NO gases. The responses are much stronger. Even when the gas concentration is only 1 ppm, the sensitivity has already gone up to 30 and 14,

much larger than any other gas. Such result proves that *h*-WO_3 is very sensitive and selective to NO_x. In addition, the response to these two gases is faster than other gases.

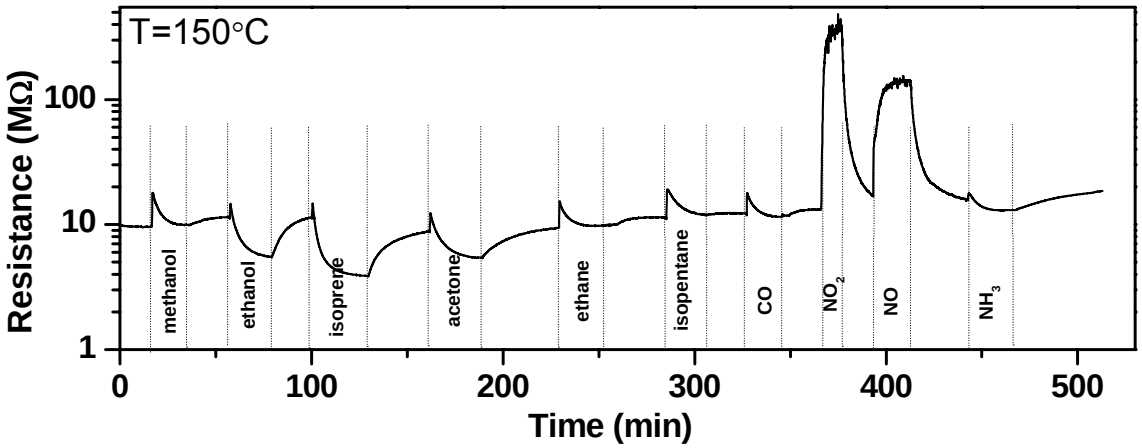

Figure 4-6 Responses of *h*-WO_3 to 1 ppm of different gases at 150 °C.

Detailed measurement was performed on NO_2, whose result is shown in Figure 4-7. With exposure to 1 ppm NO_2, the sensor resistance increased from baseline 10 MΩ to 300 MΩ (*S*=30) in about 20 min. This value changed rapidly to 2 GΩ (*S*=200) and 4 GΩ (*S*=400) respectively when we increased the NO_2 concentration to 2 ppm and 5 ppm step by step. The response times were faster when the NO_2 concentration went higher. As the NO_2 concentration lowered down afterwards, the sensor resistance decreased gradually accordingly. It is clear to see that the sensor had almost the same resistance value at the same NO_2 level as the first half part of the test, respectively. This means the sensor performance is reversible and recoverable, which is important for its application. At the end of the test, the sensor went to its baseline value when we stopped the NO_2 gas flow.

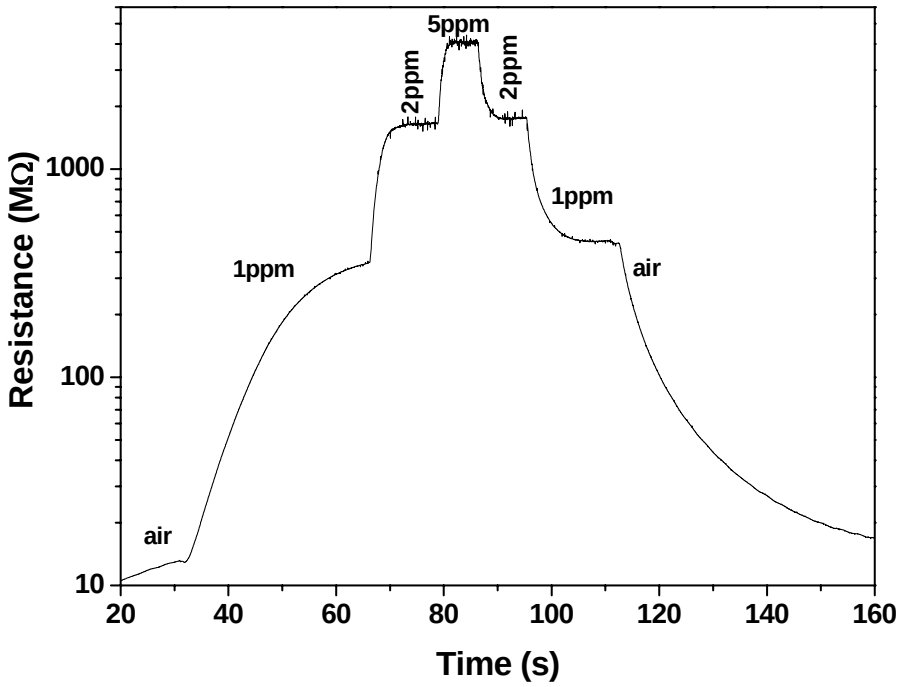

Figure 4-7 Resistance change of *h*-WO_3 with exposure to NO_2 at 150 °C

4.2.2 Sensing comparison at 350 °C

The sensing properties of *h*-WO_3 at 350 °C are quite different (Figure 4-8) from that at 150 °C (Figure 4-6) which can be described in the following aspects.

First of all, the response time and recovery time become at least three times faster. In most cases it only takes less than 2 min for the sensor to reach the equilibrium with its surrounding gases. This improvement should be contributed to enhanced activity of molecules resulting from rising temperature.

Second, the initial sharp increase of resistance at 150 °C disappears, evidenced by the shape change of acetone and ethanol response curves. In other word, the material becomes a pure n-type semiconductor.

Finally, the selective detection of NO_x gases is lost. Although the material is still sensitive to these two gases, the absolute sensitivities drops a lot to only 2.4 for NO and 3.7 for NO_2. Another striking sensitivity change occurs on isoprene

detection. The sensitivity goes up to 7, which is higher than any other gas. The sensitivities to three oxygen-containing gases, methanol, ethanol and acetone go as high as 1.8, 2 and 4, which is totally comparable with NO_x gases. The sensor is almost inert with the other gases, including ethane, isoprene, CO and NH_3. The above results imply *h*-WO_3 has a sensitive and selective detection on isoprene at 350 °C.

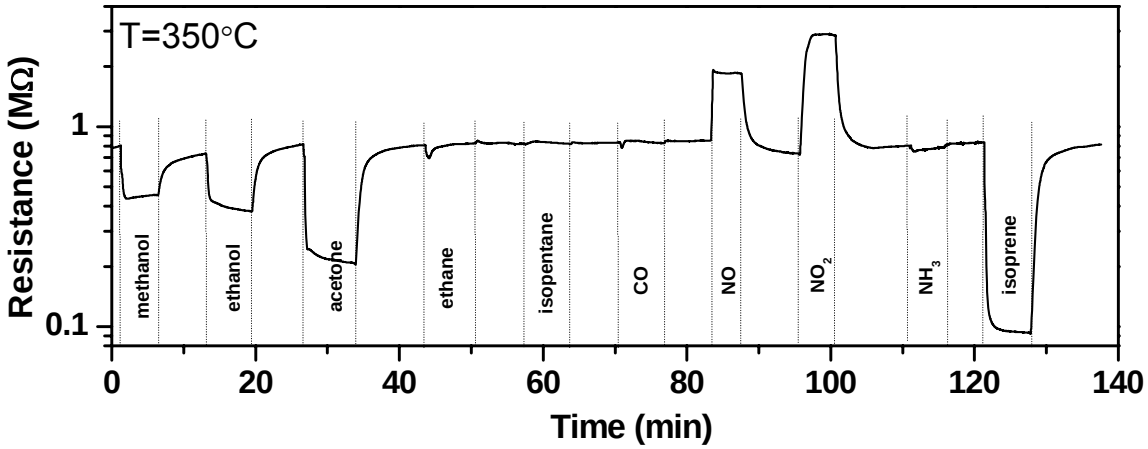

Figure 4-8 Responses of *h*-WO_3 to 1 ppm of different gases at 350 °C.

Figure 4-9 shows the detailed sensing test results of NO, NO_2, methanol, and isoprene. The sensor responded to any of the three gases fairly well. The resistance variations are steady and repeatable. Quantitative results are listed in Table 4-1.

Table 4-1 Sensing property comparison of h-WO_3 with exposure to NO, NO_2 and methanol at 350 °C

	Sensitivity			Response time (s)			Recovery time (s)		
Conc.(ppm)	**1**	**2**	**5**	**1**	**2**	**5**	**1**	**2**	**5**
NO	2.66	4.08	9.36	24	40	59	98	68	49
NO_2	2.98	6.26	11.52	82	26	43	77	39	49
methanol	2	3.23	5.92	112	125	89	380	270	170
isoprene	7.34	14.1	23.7	65	41	45	145	84	70

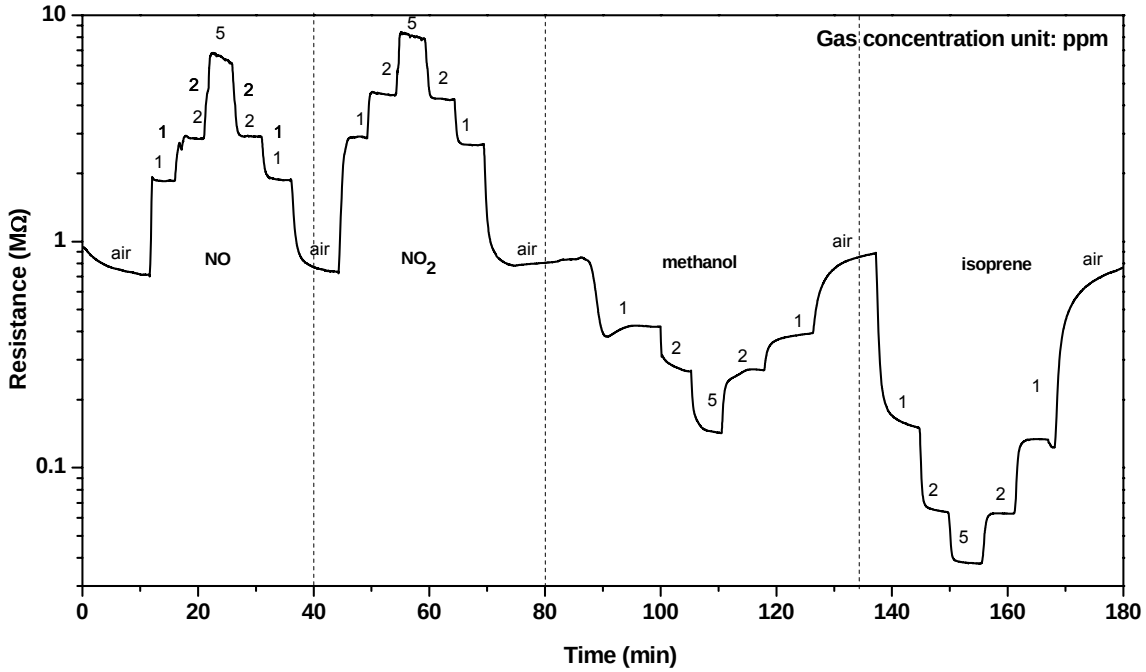

Figure 4-9 Resistance change of *h*-WO_3 with exposure to NO, NO_2, methanol, and isoprene at 350 °C

4.2.3 Discussion on NO_x detection

From the above results, we see a very high sensitivity of *h*-WO_3 to NO_x gases (*S*=30 for 1 ppm NO_2; *S*=14 for 1 ppm NO) at 150 °C. When exposed to oxygen, NO is easily converted into NO_2. Therefore, it is difficult to separate NO from NO_2. An expression of NO_x may better describe such mixture. As mentioned in Section 1.1.3, NO is the biomarker of lung diseases. In addition, NO_x is a well known air pollutant generated from automobiles and combustion facilities. It will cause acid rain and also damage our human respiratory system. The recommended exposure limits of NO_2 and NO are 1 ppm and 25 ppm respectively, set by National Institute for Occupational Safety and Health. The above results prove that our *h*-WO_3 sensor could be a promising candidate for highly sensitive and selective detection of low concentrations of NO_x gas.

As an *n*-type chemi-resistive sensor, the sensing mechanism between NO_x and *h*-WO_3 is primarily based on the electron transfer process described in Section 1.3.2. Both NO (N=O) and NO_2 (O=N=O) have unpaired electrons and they are strong oxidizers. Upon NO_2 adsorption, electron transfer occurs from WO_3 to NO_2. The reversible chemisorption reaction is:

$$NO_2 + e^- \rightleftharpoons ONO^- \quad (19)$$

ONO^- is called nitrito type adsorbates and it will dissociate into nitrosyl type adsorbates (NO^+, NO^-) along with the increase of temperature [137]. It has been proved by other groups that nitrosyl type adsorbates may be more stable than nitrito type adsorbates [138]. They occupy the active sites on tungsten oxide film surface for NO_2 adsorption. Consequently, the sensitivity of tungsten oxide to NO_2 operated decreases as temperature increases, which is consistent with our observed results.

As we already know, stable phases of WO_3 used to detect NO_x gases have been extensively studied. Thorough comparison shows that our *h*-WO_3 is more sensitive than most reported WO_3 sensors with regard to NO_x detection, which includes nanofibers (*S*=16, 1.1 ppm [68]), thin films (S=10, 2 ppm [66]) and porous structures(*S*=4, 550 ppb [138]). Although some sensors are equally or more sensitive, they either had unique morphology, such as 3D nanowire networks (*S*=200, 1 ppm [70]) and mesoporous thin films, etc. (*S*=225, 3 ppm [139]), or were prepared by specific technology to decrease their particle diameters. Considering our *h*-WO_3 material has neither very small sizes nor unique morphologies, such sensitivity enhancement is surprising. We consider

the open structure of *h*-WO_3 plays an important role on the sensitivity promotion. *H*-WO_3 has a large density of empty hexagonal tunnels along the c axis, which allows small gas molecules to go inside the material bulk. This is equal to increasing the surface area of the material and is able to absorb a large amount of NO_x atoms onto its surface, creating much more chemisorption reaction sites, which finally leads to the great enhancement of NO_x sensitivity.

4.2.4 Discussion on isoprene detection

Selective detection on isoprene at 350 °C is clearly proved in Section 4.2.2. Such detection is fast, sensitive, stable and repeatable. As we know, isoprene is one of the most common trace gases in human breath. Extensive studies have identified it as biomarker of cholesterol metabolic disorders such as hypercholesterolemia. In addition, very large amounts of isoprene are emitted from vegetation, especially from mosses, ferns, and trees. It is a greenhouse gas and has a large effect on the oxidizing potential of the atmosphere, roughly equal to methane[140]. Surprisingly, "Approximately 80% of our air pollution stems from hydrocarbons released by vegetation."* Therefore, the sensitive detection of isoprene demonstrated in this dissertation has promising applications on non-invasive disease diagnosis and environmental pollution monitoring.

Previous reports or commercially available device for isoprene detection are always based on spectrometry/spectroscopy methods, which has been described in Section 1.2. Ohira *et al.* reported an O_3-CL approach to the measurement of breath isoprene. [29] However, it requires breath sample collection and

* R. Reagan, quoted in Sierra, 65: 17 (1980).

preconcentration, making the detection not portable at all. The only work involved with isoprene detection using chemo-resistive sensors was reported by Teleki *et al.* in 2006. [111] However, their sensors based on FSP-made TiO_2 nanoparticles were neither sensitive (S=2, 1ppm) nor selective (lower sensitivity than acetone) to isoprene. We can also compare *h*-WO_3 to previously reported *γ*-WO_3 (shown in Figure 3-13 (a)). Although *γ*-WO_3 is also sensitive to isoprene (*S*=4.8), it has a cross sensitivity to acetone (*S*=4). Therefore, to our best of knowledge, our *h*-WO_3 might be the first isoprene-selective chemical sensor which has the potential to be used in non-invasive portable device for hypercholesterolemia diagnosis.

As we have already mentioned in the previous chapter, the whole WO_3 family has a sensitive detection on isoprene, whose underlying mechanism is still unclear. More work is needed to be done in this topic.

4.2.5 Temperature-dependent n-p transition

The initial increase of resistance when *h*-WO_3 is surrounded by reducing gases at 150 °C is abnormal for an n-type material. This drives us to study the temperature influence on the sensor for more details. Figure 4-10 shows the responses to high-concentration (more than 50 ppm) NH_3 at 100 °C, 200 °C, and 300 °C respectively. Such high concentrations are able to amplify the sensing signals for more accurate investigation.

At 100 ˚C, the resistance of the sensor will increase when NH_3 is introduced (Figure 4-10 (a)), which is exactly the behavior of typical *p*-type sensors. If the temperature goes to 200 ˚C, the resistance will increase first as a *p*-type sensor,

but suddenly decreases sharply (Figure 4-10 (b)), as an *n*-type sensor. When the temperature increases to 300 ˚C (Figure 4-10 (c)), as the resistance drops along with each pulse of NH_3 invasion, the sensor behaves as a typical n-type material from beginning to end.

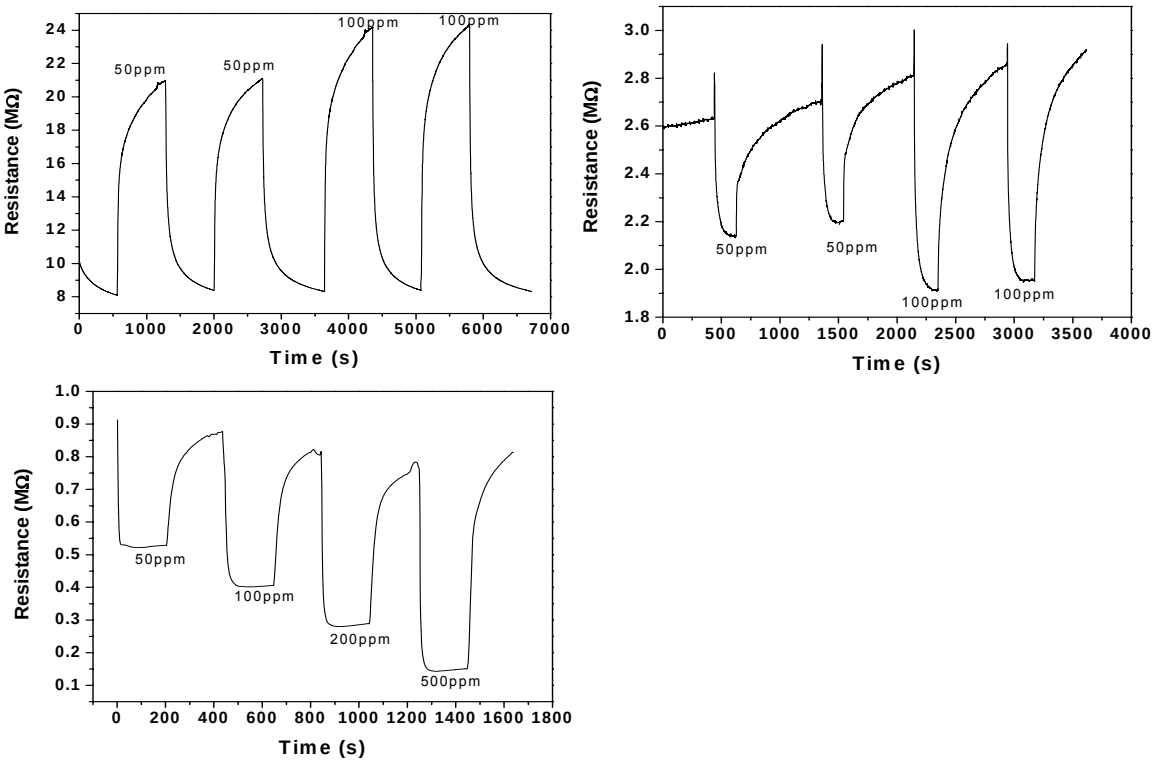

Figure 4-10 Response of *h*-WO_3 to NH_3 at different temperatrures: (a) 100 °C, (b) 200 °C, and (c) 300 °C.

Such contradictory results clearly prove that the material may experience an n-p transition, which has been described in Section 1.3.2. This phenomenon results from surface effect whereas the properties of the bulk material hardly change. Different from reported work in which strong oxidizing gases result in the transition, temperature becomes the driving force here.

We consider large numbers of tunnels in h-WO_3 are able to absorb oxygen atoms onto its surface. The existence of excessive oxygen atoms near the

surface at RT has been proved by XPS measurement (see Section 4.1 for details).The consequential lack of tungsten atoms may create tungsten vacancies near the surface which obviously provide holes.

At a lower temperature, tungsten vacancies become dominating point defects near the surface. Thus, holes are major charge carriers here and a *p*-type inversion layer forms. However, in the bulk oxygen vacancies are still major point defects and the whole material is still *n*-type. There is a depletion layer between them. When the material is surrounded by the reducing gas (e.g. NH_3), it will donate free electrons into the material which consume near-surface holes. In this way, inversion layer becomes depletion layer and the surface resistance is increased which finally causes the resistance of the whole material to increase. Hence, we observe a *p*-type sensing response during detection of reducing gas at a lower temperature (Figure 4-10 (a)).

When the temperature increases, as mentioned before, surface and bulk oxygen atoms tend to break the bonds and evaporate into the atmosphere with the thermal excitation, leaving oxygen vacancies. More free electrons are created afterwards. Hence, the inversion layer becomes thinner. When the material is exposed to reducing gases, the inversion layer turns into depletion layer quickly, resulting in the increase of resistance at the first moment. As more free electrons go into the material, the depletion layer is becoming thinner or even disappears. This process leads to the succeeding resistance drop (Figure 4-10 (b)).

If the temperature is high enough, the near-surface inversion layer disappears completely and only a depletion layer forms near the surface, which

behaves as a typical *n*-type sensor. Once NH_3 reacts with the surface, the depletion layer vanishes quickly, replaced by an accumulation layer. The resistance keeps falling down until the system reaches equilibrium (Figure 4-10 (c)).

CHAPTER 5 Handheld breath analyzer development

5.1 Prototype design

From the results discussed in Chapters 3 and 4, we have found appropriate materials for acetone and NO_x selective detections. These sensor materials must be integrated into a sensing device to realize their functions. The schematic diagram of the circuit is presented in Figure 5-1.

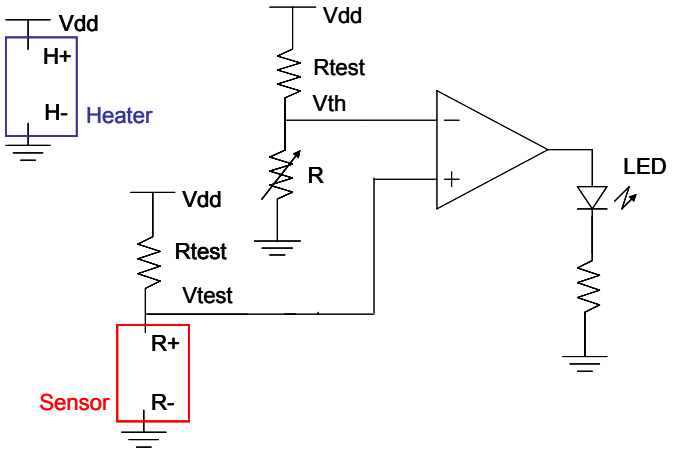

Figure 5-1 Schematic diagram of the readout circuitry.

The basic concept of the sensing device is to compare the resistance of the sensor material to a comparative resistor. The resistance of this comparator is determined by a pre-assumed biomarker concentration threshold in the human breath for certain disease diagnosis as well as the behavior of the sensing material. The sensing material's resistance is determined by the actual biomarker concentration. Assuming the biomarker is a reducing gas, if this resistance is lower than that of the resistor, the actual concentration of the biomarker is then higher than the threshold, which implies the testee has a high probability to be afflicted with this disease.

The comparison result can be reflected by the lightening of an LED indicator. In addition, since our sensors work at elevated temperatures, a heating component should be attached with the sensor substrate.

In practice, the sensor materials are deposited onto a tiny home-made Pt-electrode coated alumina substrate (3 mm × 3 mm). One sensor or two parallel connected sensors are adhered to a commercial heater (M1020, Heraeus Sensor Tech.). The heater, whose temperature is controlled by the voltage applied on it, is able to heat the sensor up to 500 °C. This sensor/heater pair is the key component of breath analyzer. It is connected with a transistor outline (TO-8) header (SCHOTT North America Inc.), which is ready to be integrated into the device. Figure 5-2 records the assembly of the sensor/heater pair.

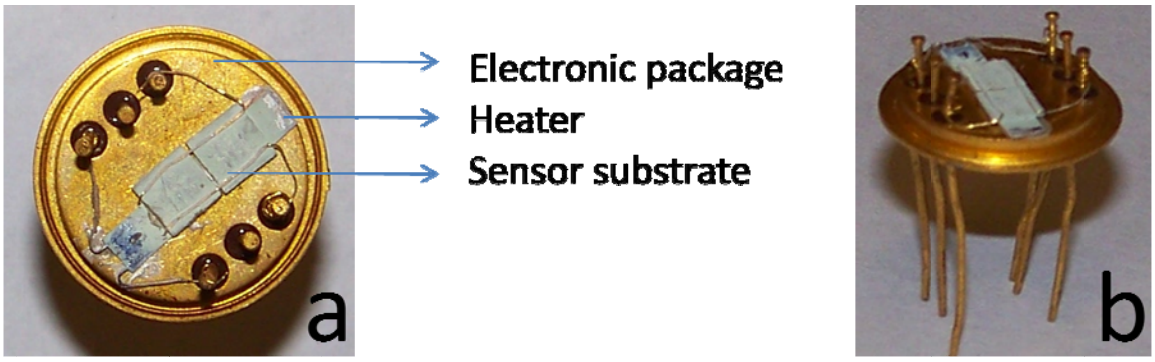

Figure 5-2 Key component of the breath analyzer: sensor and heater assembly: (a) top view; (b) side view.

Figure 5-3 shows the photograph of the manufactured prototype. I appreciate Prof. M. Stanacevic and his student X. Yun very much, who took great and successful effort to make this delicate device for us. The dimension of the prototype is 15 cm (L) × 7.5 cm (W) which meets the requirement of “portable”. The bottom-left part is the sensor. It is isolated from the environment by a specially designed chamber made of Teflon. A channel with a mouthpiece allows

the human breath flow or controlled gas flow to go through the chamber and interact with the sensor (not shown in the photograph).

Although there is only one comparator, this device is designed to set up two threshold values, upper threshold and lower threshold. When the sensor resistance is larger than upper threshold, a red LED turns on. In contrast, if it is smaller than lower threshold, a green LED turns on. If this value falls between these two limits, neither LED lights up. This makes this device a universal analyzer for breath analysis, whether the biomarker has an oxidizing or reducing characteristic.

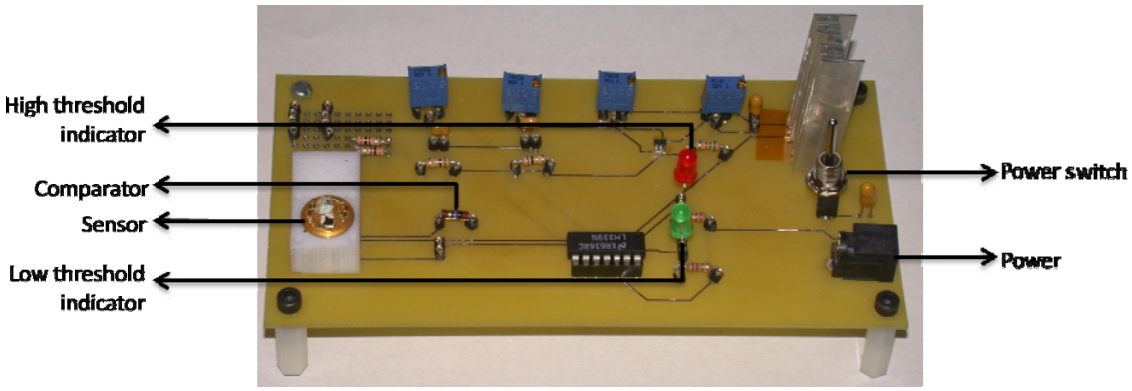

Figure 5-3 Photograph of designed portable device for disease diagnosis.

Two concerns for the reliability of this breath analyzer are the influence of humidity and CO_2. They are major components in human breath and their concentrations are thousand times higher than any trace gases. Therefore, they will inevitably influence the behavior of the sensing elements, even though our *ε*-WO_3 and *h*-WO_3 sensors are insensitive to them. A solution to this problem is to introduce CO_2 and humidity filters between the mouthpiece and the sensor. Both filters are commercially available.

5.2 Preliminary test

Before used for medical examinations, the device was pre-tested in the laboratory. The following paragraph describes the whole procedure of test for an acetone selective ε-WO_3 sensor.

Acetone is the biomarker for diabetes. A concentration of 1.8 ppm acetone can be regarded as the threshold value of diabetes diagnosis. As discussed in Section 3.2, 10 at% Cr-doped WO_3 nanoparticles, whose ε-WO_3 is up to 80%, is selective to acetone gas. A sensor based on this material was prepared. The baseline of the sensor resistance is around 15 MΩ. At 1.8 ppm acetone exposure, the resistance lowers down to around 3.5 MΩ which was set as the lower threshold value of the analyzer. The upper threshold was set to 20 MΩ a little higher than the sensor's baseline value.

When we switched on the powder, a 9 V voltage was applied on the heater which heats the sensor up to 350 °C in the isolated environment. Meanwhile, a gas flow of 80% N_2 mixed with 20 % O_2 passed through the channel and entered the chamber as a background gas. At the very beginning, the red LED lit on because at low temperatures semiconducting oxide particles have a very high resistance. As the temperature arrived at 350 °C in a few seconds, the red light turned off, indicating the sensor reached its baseline.

We waited a few minutes for the sensor to become stable. Then we introduced increasing concentrations of acetone into the chamber by adjusting the gas flow coming from each gas cylinder. From, 0.5 ppm to 1 ppm, then 1.5 ppm, we didn't see any change on the device. The green light turned on when we

further raised the concentration to 1.8 ppm. This means our device only responds 1.8 ppm or higher concentrations of acetone gas, good for diabetes diagnosis.

To validate the selectivity of the gas analyzer, we also introduced several types of other gases which are common in human breath, including NO, NH_3, CO, ethanol, methanol, and ethane. The sensor did not have any response to NO, NH_3, CO, ethane up to 10 ppm, which is much higher than their concentrations in the human breath (Table 1-1). The device did not show response to ethanol and methanol up to 3 ppm. However, higher concentrations turned on the green LED. We are aware that elevated levels of ethanol and methanol levels usually come from alcohol ingestion and fruit consumption [141]. Therefore we highly suggest the testees not to consume alcohol beverages or fruits before operating this device to avoid confusion or misdiagnosis.

The device responded acetone quite fast, in less than 20 seconds. We also testified its long-term stability by keeping switching on the power for one hour. During this period, we randomly introduced different concentrations of acetone into the sensor-enclosed chamber. The device could successfully identify 1.8 ppm acetone in most cases, exhibiting its good stability. We also proved that this prototype could work repeatedly by carrying out the above tests in different days.

5.3 Necessary improvements in the future

Although it shows good stability and repeatability, this simple device cannot withstand multiple thermal shocks. When experiencing repeating heating-cooling cycles, the leads connecting the sensor element with the TO-8 header were easy to peel off, resulting in malfunction of the whole device. This problem could be

resolved by improving the manufacturing technique of the sensing element.

Another problem for this device is its high working temperature (350 °C). The isolating chamber becomes very hot after a long-time run, which not only has the chance to hurt users, but also aggravate aging of the Teflon plastic. A better thermal insulation system is necessary for design of the next generation of the breath analyzer.

Finally, as we know, temperature plays a great role on sensor behaviors. Our existing device, however, cannot change the work temperature because its working voltage is fixed at 9V.A variable/multiple-voltage power transformer is highly recommended to make this device more flexible and universal.

CHAPTER 6 Conclusions and future work

6.1 Conclusions

This dissertation has discussed the development of several selective biomarker sensors based on RT stable *ε*-WO_3 and *h*-WO_3 nanostructured materials.

Ferroelectric *ε*-WO_3 nanoparticles were synthesized using the flame spray pyrolysis method. The percentage of *ε*-WO_3 is directly related to the particle size of the product. Smaller particles contain more *ε*-WO_3. The *ε*-WO_3 polymorph vanishes during heat treatment in pure WO_3 products, but chromium dopants are able to stabilize this phase by forming a chromate surface layer, whereas manganese dopants form $MnWO_4$ compounds which cannnot prevent the *ε*-to-*γ* transition. The resistive sensor based on 10at%Cr doped *ε*-WO_3 nanoparticles was found to be very sensitive and selective to low concentrations of acetone (0.2-1 ppm) compared to a series of interfering gases at 400°C. The proposed explanation for the materials selectivity to acetone is the likely interaction between the surface dipole of ferroelectric *ε*-WO_3 nanoparticles and the highly polar acetone gas molecules.

Open structured *h*-WO_3 nanoparticles were produced by acid precipitation method. The product was characterized by different techniques. It was found that *h*-WO_3 is much more sensitive to NO_x than other gases at 150 °C but such selectivity disappears at 350 °C. Instead, the material shows a good sensitivity and satisfactory selectivity to isoprene gas. We consider its open structure leads

to increased sensitivity compared to γ-WO_3. A p-n transition was found when the working temperature of the sensor increased from RT to 350 °C which could be related to the excessive surface oxygen of the product.

Finally, a handheld exhaled breath analyzer prototype has been developed for non-invasive disease diagnosis. Preliminary tests have been performed in the laboratory environment. It was proved ε-WO_3 nanoparticle-based analyzer only shows response to 1.8 ppm or higher concentrations of acetone. The response is selective, real-time and repeatable, making this invention a revolutionary, non-invasive, diabetes diagnostic tool.

6.2 Future work

Based on the results obtained from this dissertation, future work of this project could be focused on the following aspects.

1. Breath analyzer device modification and practical use. The breath analyzer device needs to be utilized in actual disease diagnosis to verify its validity. Without the proof of medical tests, we cannot declare the success of this device. In addition, as partly described in Section 5.3, this specially designed device needs a lot of modifications to make it more universal and more stable, e.g., new manufacturing techniques to prevent thermal shock, new materials or improved designs for isolation chamber, a variable-voltage power. If possible, a numerical display, for displaying the exact concentration of the analyte is highly recommended, which could be used for daily monitoring of biomarker level variations, making the device much more practical.

2. Sensing mechanism investigation. This dissertation involves with several

selective sensing processes, including *ε*-WO_3 nanoparticles for acetone selective detection, *h*-WO_3 material for NO_x selective detection at 150 °C and for isoprene selective detection at 350. °C. It is believed that surface adsorption, including both physisorptions and chemisorptions, of target gas molecules onto the material determines sensing processes. Unfortunately, their details are still unclear. We proposed the ferroelectricity of *ε*-WO_3 leads to a strong interaction with high-dipole-moment species such as acetone. This is a new sensing mechanism. Although it sounds reasonable, it is still a hypothesis whose validity needs experimental data to demonstrate. For example, the affinity between solid surface and gas molecules with different dipole moments is worth to measure. With regard to h-WO_3 as an isoprene sensor, there is a lack of sufficient data for metal oxide surface in the catalysis literature for isoprene. Detailed analysis of the evolution of the surface reactions with respect to temperature and the polymorph needs to be carried out, in order to exactly understand the reaction products from the surface interaction. In-situ surface chemistry analysis techniques, including XPS, FTIR, and EELS, etc., will be particularly useful.

3. ε-WO_3 study. RT stable ε-WO_3 polymorph is a novel system in the WO_3 family, waiting for extensive studies on its properties and potential applications. The unique gas sensing property exhibited in this dissertation is only the tip of the iceberg. More exciting results are expected. As an example, we can investigate the ferroelectricity characteristics of the material, including the hysteresis loop and the Curie temperature. Furthermore, WO_3 is famous for its electrochromic applications. It is worthwhile to study the electrochromic

properties of ε-WO_3 with different sizes and dopants and compare the results with other phases of WO_3.

4. Metastable phase control. Metastable polymorphs of materials always draw people's great attention because of their unique and excellent properties that stable phases do not exhibit. However, the synthesis and preservation of metastable phases are quite difficult which limits its applications. This dissertation invented a method to preserve *ε*-WO_3 above RT by introducing a surface chromate protection layer. This method may be adopted by other materials which have different crystal forms, e.g. TiO_2 with rutile, and anatase allotropes. The *h*-WO_3 metastable phase, which only exists below 425 °C, may also be stabilized based on the similar concept. Future research on this focus may have the opportunity to establish a general approach to control solid-state phase evolutions.

Bibliography

1. M. Phillips, *Breath tests in medicine.* Sci. Am., 1992. 267(1): p. 74-79.

2. L. Pauling, et al., *Quantitative analysis of urine vapor and breath by gas-liquid partition chromatography.* Proc. Natl. Acad. Sci. U. S. A., 1971. 68(10): p. 2374-2376.

3. W. Miekisch, J.K. Schubert, and G.F.E. Noeldge-Schomburg, *Diagnostic potential of breath analysis - focus on volatile organic compounds.* Clin. Chim. Acta, 2004. 347(1-2): p. 25-39.

4. W.Q. Cao and Y.X. Duan, *Breath analysis: Potential for clinical diagnosis and exposure assessment.* Clin. Chem., 2006. 52(5): p. 800-811.

5. B. Buszewski, et al., *Human exhaled air analytics: Biomarkers of diseases.* Biomed. Chromatogr., 2007. 21(6): p. 553-566.

6. G.E. Umpierrez, et al., *Differences in metabolic and hormonal milieu in diabetic- and alcohol-induced ketoacidosis.* J. Crit. Care, 2000. 15(2): p. 52-59.

7. C.H. Deng, et al., *Determination of acetone in human breath by gas chromatography-mass spectrometry and solid-phase microextraction with on-fiber derivatization.* J. Chromatogr. B, 2004. 810(2): p. 269-275.

8. D.H. Yates, *Role of exhaled nitric oxide in asthma.* Immunol. Cell Biol., 2001. 79(2): p. 178-190.

9. R. Katial and L. Stewart, *Exhaled nitric oxide: A test for diagnosis and control of asthma?* Curr. Allergy Asthma Rep., 2007. 7(6): p. 459-463.

10. L.J. Dupont, M.G. Demedts, and G.M. Verleden, *Prospective evaluation of the validity of exhaled nitric oxide for the diagnosis of asthma.* Chest, 2003. 123(3): p. 751-756.

11. W.Q. Cao and Y.X. Duan, *Current status of methods and techniques for breath analysis.* Crit. Rev. Anal. Chem., 2007. 37(1): p. 3-13.

12. A.M. Leone, et al., *Nitric oxide is present in exhaled breath in humans: direct GC-MS confirmation.* Biochem. Biophys. Res. Commun., 1994. 201(2): p. 883-887.

13. D. Smith and P. Spanel, *Selected ion flow tube mass spectrometry (SIFT-MS) for on-line trace gas analysis.* Mass Spectrom. Rev., 2005. 24(5): p. 661-700.

14. P. Spanel, S. Davies, and D. Smith, *Quantification of breath isoprene using the selected ion flow tube mass spectrometric analytical method.* Rapid Commun. Mass Spectrom., 1999. 13(17): p. 1733-1738.

15. A.M. Diskin, P. Spanel, and D. Smith, *Time variation of ammonia, acetone, isoprene and ethanol in breath: a quantitative SIFT-MS study over 30 days.* Physiol. Meas., 2003. 24(1): p. 107-119.

16. J.A. Silver, *Frequency-modulation spectroscopy for trace species detection - theory and comparison among experimental methods.* Appl. Opt., 1992. 31(6): p. 707-717.

17. C. Roller, et al., *Simultaneous NO and CO_2 measurement in human breath with a single IV-VI mid-infrared laser.* Opt. Lett., 2002. 27(2): p. 107-109.

18. C. Roller, et al., *Nitric oxide breath testing by tunable-diode laser absorption spectroscopy: application in monitoring respiratory inflammation.* Appl. Opt., 2002. 41(28): p. 6018-6029.

19. J. Taucher, et al., *Detection of isoprene in expired air from human subjects using proton-transfer-reaction mass spectrometry.* Rapid Commun. Mass Spectrom., 1997. 11(11): p. 1230-1234.

20. H. Lord, et al., *Breath analysis and monitoring by membrane extraction with sorbent interface.* Anal. Chem., 2002. 74(21): p. 5650-5657.

21. C.J. Wang and A. Mbi, *A new acetone detection device using cavity ringdown spectroscopy at 266 nm: evaluation of the instrument performance using acetone sample solutions.* Meas. Sci. Technol., 2007. 18(8): p. 2731-2741.

22. C.K. O'Sullivan and G.G. Guilbault, *Commercial quartz crystal microbalances - theory and applications.* Biosens. Bioelectron., 1999. 14(8-9): p. 663-670.

23. H.H. Huang, et al., *A highly sensitive QCM sensor coated with Ag^+-ZSM-5 film for medical diagnosis.* Sens. Actuators, B, 2004. 101(3): p. 316-321.

24. A. Palaniappan, et al., *Selective and enhanced nitric oxide detection using hemoprotein/silica hybrids.* Sens. Actuators, B, 2008. 133(1): p. 241-243.

25. A. Palaniappan, et al., *Phthalocyanine/silica hybrid films on QCM for enhanced nitric oxide sensing.* Sens. Actuators, B, 2008. 129(1): p. 184-187.

26. M. Nakagawa, et al., *Analytical detection system of mixed odor vapors using chemiluminescence-based gas sensor.* Sens. Actuators, B, 1996. 34(1-3): p. 334-338.

27. T. Okabayashi, et al., *High sensitive hydrocarbon gas sensor utilizing cataluminescence of γ-Al_2O_3 activated with Dy^{3+}.* Sens. Actuators, B, 2000. 64(1-3): p. 54-58.

28. Y.F. Zhu, et al., *Development of a gas sensor utilizing chemiluminescence on nanosized titanium dioxide.* Anal. Chem., 2002. 74(1): p. 120-124.

29. S.I. Ohira, et al., *Can breath isoprene be measured by ozone chemiluminescence?* Anal. Chem., 2007. 79(7): p. 2641-2649.

30. F. Rock, N. Barsan, and U. Weimar, *Electronic nose: Current status and future trends.* Chem. Rev., 2008. 108(2): p. 705-725.

31. A. Bielanski, J. Deren, and J. Haber, *Electric conductivity and catalytic activity of semiconducting oxide catalysts.* Nature, 1957. 179(4561): p. 668-679.

32. T. Seiyama, et al., *A new detector for gaseous components using semiconductive thin films.* Anal. Chem., 1962. 34(11): p. 1502-1503.

33. A.K. Prasad, D.J. Kubinski, and P.I. Gouma, *Comparison of sol-gel and ion beam deposited MoO_3 thin film gas sensors for selective ammonia detection.* Sens. Actuators, B, 2003. 93(1-3): p. 25-30.

34. A. Gurlo, et al., *A p- to n-transition on α-Fe_2O_3-based thick film sensors studied by conductance and work function change measurements.* Sens. Actuators, B, 2004. 102(2): p. 291-298.

35. I.D. Kim, et al., *Ultrasensitive chemiresistors based on electrospun TiO_2 nanofibers.* Nano Lett., 2006. 6(9): p. 2009-2013.

36. I. Schechter, M. Benchorin, and A. Kux, *Gas-sensing properties of porous silicon.* Anal. Chem., 1995. 67(20): p. 3727-3732.

37. D. Manno, et al., *Physical and structural characterization of tungsten oxide thin films for NO gas detection.* Thin Solid Films, 1998. 324(1-2): p. 44-51.

38. R. Chatten, et al., *The oxygen vacancy in crystal phases of WO_3.* J. Phys. Chem. B, 2005. 109(8): p. 3146-3156.

39. P.M. Woodward, A.W. Sleight, and T. Vogt, *Structure Refinement of Triclinic Tungsten Trioxide.* J. Phys. Chem. Solids, 1995. 56(10): p. 1305-1315.

40. A.R. Siedle, et al., *Solid-state polymerization of molecular-metal oxide clusters: aluminum 12-tungstophosphate.* J. Am. Chem. Soc., 1989. 111(5): p. 1665-1669.

41. B. Gerand, et al., *Structural study of a new hexagonal form of tungsten trioxide.* J. Solid State Chem., 1979. 29(3): p. 429-434.

42. J. Oi, A. Kishimoto, and T. Kudo, *Hexagonal tungsten trioxide obtained from peroxo-polytungstate and reversible lithium electro-intercalation into its framework.* J. Solid State Chem., 1992. 96(1): p. 13-19.

43. E. Salje and K. Viswanathan, *Physical properties and phase transitions in WO_3.* Acta Crystallogr., Sect. A: Found. Crystallogr., 1975. A 31(May1): p. 356-359.

44. B.T. Matthias and E.A. Wood, *Low temperature polymorphic transformation in WO_3.* Phys. Rev., 1951. 84(6): p. 1255-1255.

45. P.M. Woodward, A.W. Sleight, and T. Vogt, *Ferroelectric tungsten trioxide.* J. Solid State Chem., 1997. 131(1): p. 9-17.

46. E.K.H. Salje, et al., *Crystal structure and paramagnetic behaviour of ε-WO_{3-x}.* J. Phys.: Condens. Matter, 1997. 9(31): p. 6563-6577.

47. M. Arai, et al., *Raman studies of phase transitions in gas-evaporated WO_3 microcrystals.* Solid State Commun., 1990. 75(7): p. 613-616.

48. S. Hayashi, et al., *Phase transitions in gas evaporated WO_3 microcrystals: a Raman study.* J. Phys. Soc. Jpn., 1992. 61(3): p. 916-923.

49. E. Cazzanelli, et al., *Low-temperature polymorphism in tungsten trioxide powders and its dependence on mechanical treatments.* J. Solid State Chem., 1999. 143(1): p. 24-32.

50. A.G. Souza, et al., *Phase transition in WO_3 in microcrystals obtained by sintering process.* J. Raman Spectrosc., 2001. 32(8): p. 695-699.

51. V. Khatko, et al., *X-ray investigations of nanopowder WO_3 thick films.* Phys. Status Solidi A-Appl. Mat., 2005. 202(10): p. 1973-1979.

52. N. Kumagai, et al., *Synthesis of hexagonal form of tungsten trioxide and electrochemical lithium insertion into the trioxide.* Solid State Ion., 1996. 86-8: p. 1443-1449.

53. M. Hibino, W.C. Han, and T. Kudo, *Electrochemical lithium intercalation into a hexagonal WO_3 framework and its structural change.* Solid State Ion., 2000. 135(1-4): p. 61-69.

54. S. Komaba, et al., *Hydrothermal synthesis of hexagonal tungsten trioxide from Li_2WO_4 solution and electrochemical lithium intercalation into the oxide.* Solid State Ion., 2000. 135(1-4): p. 193-197.

55. Z.J. Gu, et al., *Large-scale synthesis of single-crystal hexagonal tungsten trioxide nanowires and electrochemical lithium intercalation into the nanocrystals.* J. Solid State Chem., 2007. 180(1): p. 98-105.

56. I.M. Szilagyi, et al., *Stability and controlled composition of hexagonal WO_3.* Chem. Mater., 2008. 20(12): p. 4116-4125.

57. K.H. Cheng, A.J. Jacobson, and M.S. Whittingham, *Hexagonal tungsten trioxide and its intercalation chemistry.* Solid State Ion., 1981. 5(Oct): p. 355-358.

58. Y.M. Solonin, O.Y. Khyzhun, and E.A. Graivoronskaya, *Nonstoichiometric tungsten oxide based on hexagonal WO_3.* Cryst. Growth Des., 2001. 1(6): p. 473-477.

59. Y. Oaki and H. Imai, *Room-temperature aqueous synthesis of highly luminescent $BaWO_4$-polymer nanohybrids and their spontaneous conversion to hexagonal WO_3 nanosheets.* Adv. Mater., 2006. 18(14): p. 1807-1811.

60. Y. Wu, et al., *Growth of hexagonal tungsten trioxide tubes.* J. Cryst. Growth, 2006. 292(1): p. 143-148.

61. P.J. Shaver, *Activated tungsten oxide gas detectors.* Appl. Phys. Lett., 1967. 11(8): p. 255-257.

62. M. Akiyama, et al., *Tungsten oxide-based semiconductor sensor highly sensitive to NO and NO_2.* Chem. Lett., 1991. 20(9): p. 1611-1614.

63. G. Sberveglieri, et al., *WO_3 sputtered thin-films for NO_x monitoring.* Sens. Actuators, B, 1995. 26(1-3): p. 89-92.

64. Y. Zhao, Z.C. Feng, and Y. Liang, *Pulsed laser deposition of WO_3-base film for NO_2 gas sensor application.* Sens. Actuators, B, 2000. 66(1-3): p. 171-173.

65. Y.G. Choi, et al., *Wet process-prepared thick films of WO_3 for NO_2 sensing.* Sens. Actuators, B, 2003. 95(1-3): p. 258-265.

66. G.Z. Xie, et al., *Gas sensing characteristics of WO_3 vacuum deposited thin films.* Sens. Actuators, B, 2007. 123(2): p. 909-914.

67. S. Ashraf, et al., *Aerosol assisted chemical vapour deposition of WO_3 thin films from tungsten hexacarbonyl and their gas sensing properties.* J. Mater. Chem., 2007. 17(35): p. 3708-3713.

68. S. Piperno, et al., *WO_3 nanofibers for gas sensing applications.* J. Appl. Phys., 2007. 101(12): p. 124504.

69. B. Deb, et al., *Gas sensing behaviour of mat-like networked tungsten oxide nanowire thin films.* Nanotechnology, 2007. 18(28): p. 7.

70. A. Ponzoni, et al., *Ultrasensitive and highly selective gas sensors using three-dimensional tungsten oxide nanowire networks.* Appl. Phys. Lett., 2006. 88(20): p. 203101.

71. E. Rossinyol, et al., *Mesostructured pure and copper-catalyzed tungsten oxide for NO_2 detection.* Sens. Actuators, B, 2007. 126(1): p. 18-23.

72. M. Penza, C. Martucci, and G. Cassano, *NO_x gas sensing characteristics of WO_3 thin films activated by noble metals (Pd, Pt, Au) layers.* Sens. Actuators, B, 1998. 50(1): p. 52-59.

73. P. Ivanov, et al., *On the effects of the materials and the noble metal additives to NO_2 detection.* Sens. Actuators, B, 2006. 118(1-2): p. 311-317.

74. P.G. Su, R.J. Wu, and F.P. Nieh, *Detection of nitrogen dioxide using mixed tungsten oxide-based thick film semiconductor sensor.* Talanta, 2003. 59(4): p. 667-672.

75. M. Blo, et al., *Synthesis of pure and loaded powders of WO_3 for NO_2 detection through thick film technology.* Sens. Actuators, B, 2004. 103(1-2): p. 213-218.

76. V. Khatko, et al., *Gas sensing properties of nanoparticle indium-doped WO_3 thick films.* Sens. Actuators, B, 2005. 111: p. 45-51.

77. E. Rossinyol, et al., *Synthesis and characterization of chromium-doped mesoporous tungsten oxide for gas-sensing applications.* Adv. Funct. Mater., 2007. 17(11): p. 1801-1806.

78. L.E. Depero, et al., *Preparation and micro-structural characterization of nanosized thin film of TiO_2-WO_3 as a novel material with high sensitivity towards NO_2.* Sens. Actuators, B, 1996. 36(1-3): p. 381-383.

79. D.S. Lee, et al., *Nitrogen oxides-sensing characteristics of WO_3-based nanocrystalline thick film gas sensor.* Sens. Actuators, B, 1999. 60(1): p. 57-63.

80. D.S. Lee, et al., *The TiO_2-adding effects in WO_3-based NO_2 sensors prepared by coprecipitation and precipitation method.* Sens. Actuators, B, 2000. 65(1-3): p. 331-335.

81. K. Galatsis, et al., *Comparison of single and binary oxide MoO_3, TiO_2 and WO_3 sol-gel gas sensors.* Sens. Actuators, B, 2002. 83(1-3): p. 276-280.

82. Z. Ling, C. Leach, and R. Freer, *NO_2 sensitivity of a heterojunction sensor based on WO_3 and doped SnO_2.* J. Eur. Ceram. Soc., 2003. 23(11): p. 1881-1891.

83. E.H. Espinosa, et al., *Highly selective NO_2 gas sensors made of MWCNTs and WO_3 hybrid layers.* J. Electrochem. Soc., 2007. 154(5): p. J141-J149.

84. O. Berger, W.J. Fischer, and V. Melev, *Tungsten-oxide thin films as novel materials with high sensitivity and selectivity to NO_2, O_3 and H_2S - Part I: Preparation and microstructural characterization of the tungsten-oxide thin films.* J. Mater. Sci. - Mater. Med., 2004. 15(7): p. 463-482.

85. O. Berger, et al., *Tungsten-oxide thin films as novel materials with high sensitivity and selectivity to NO_2, O_3, and H_2S - Part II: Application as gas sensors.* J. Mater. Sci. - Mater. Med., 2004. 15(7): p. 483-493.

86. E.P.S. Barrett, G.C. Georgiades, and P.A. Sermon, *The mechanism of operation of WO_3-based H_2S sensors.* Sens. Actuators, B, 1990. 1(1-6): p. 116-120.

87. R. Ionescu, et al., *Low-level detection of ethanol and H_2S with temperature-modulated WO_3 nanoparticle gas sensors.* Sens. Actuators, B, 2005. 104(1): p. 132-139.

88. I. Ruokamo, et al., *H_2S response of WO_3 thin-film sensors manufactured by silicon processing technology.* Sens. Actuators, B, 1994. 19(1-3): p. 486-488.

89. H.M. Lin, et al., *Nanocrystalline WO_3-based H_2S sensors.* Sens. Actuators, B, 1994. 22(1): p. 63-68.

90. C.S. Rout, M. Hegde, and C.N.R. Rao, *H_2S sensors based on tungsten oxide nanostructures.* Sens. Actuators, B, 2008. 128(2): p. 488-493.

91. M. Ando, et al., *H_2S and CH_3SH sensor using a thick-film of gold-loaded tungsten-oxide.* Chem. Lett., 1994. 23(2): p. 335-338.

92. L.N. Geng, et al., *H2S sensitivity study of polypyrrole/WO3 materials.* Solid-State Electronics, 2006. 50(5): p. 723-726.

93. W.H. Tao and C.H. Tsai, *H_2S sensing properties of noble metal doped WO_3 thin film sensor fabricated by micromachining.* Sens. Actuators, B, 2002. 81(2-3): p. 237-247.

94. S.R. Aliwell, et al., *Ozone sensors based on WO_3: a model for sensor drift and a measurement correction method.* Meas. Sci. Technol., 2001. 12(6): p. 684-690.

95. M. Bendahan, et al., *Characterization of ozone sensors based on WO_3 reactively sputtered films: influence O_2 concentration in the sputtering gas and working temperature.* Sens. Actuators, B, 2004. 100(3): p. 320-324.

96. C. Cantalini, et al., *Investigation on the O_3 sensitivity properties of WO_3 thin films prepared by sol-gel, thermal evaporation and r.f. sputtering techniques.* Sens. Actuators, B, 2000. 64(1-3): p. 182-188.

97. M. Gillet, et al., *Grain size effect in sputtered tungsten trioxide thin films on the sensitivity to ozone.* Thin Solid Films, 2005. 484(1-2): p. 358-363.

98. G. Korotcenkov, et al., *Ozone sensors on the base of SnO_2 films deposited by spray pyrolysis.* Sens. Actuators, B, 2007. 120(2): p. 679-686.

99. A. Labidi, et al., *Ethanol and ozone sensing characteristics of WO_3 based sensors activated by Au and Pd.* Sens. Actuators, B, 2006. 120(1): p. 338-345.

100. S. Vallejos, et al., *Ozone monitoring by micro-machined sensors with WO_3 sensing films.* Sens. Actuators, B, 2007. 126(2): p. 573-578.

101. T. Maekawa, et al., *Gold-loaded tungsten-oxide sensor for detection of ammonia in air.* Chem. Lett., 1992. 21(4): p. 639-642.

102. M. Ando, et al., *Ammonia gas sensor using thick film of Au-loaded tungsten trioxide.* J. Ceram. Soc. Jpn., 1996. 104(12): p. 1112-1116.

103. E. Llobet, et al., *Fabrication of highly selective tungsten oxide ammonia sensors.* J. Electrochem. Soc., 2000. 147(2): p. 776-779.

104. C.N. Xu, et al., *Selective detection of NH_3 over NO in combustion exhausts by using Au and MoO_3 doubly promoted WO_3 element.* Sens. Actuators, B, 2000. 65(1-3): p. 163-165.

105. K. Kanda and T. Maekawa, *Development of a WO_3 thick-film-based sensor for the detection of VOC.* Sens. Actuators, B, 2005. 108(1-2): p. 97-101.

106. J. Hubalek, et al., *Pt-loaded Al_2O_3 catalytic filters for screen-printed WO_3 sensors highly selective to benzene.* Sens. Actuators, B, 2004. 101(3): p. 277-283.

107. R. Strobel and S.E. Pratsinis, *Flame aerosol synthesis of smart nanostructured materials.* J. Mater. Chem., 2007. 17(45): p. 4743-4756.

108. R. Jossen, et al., *Morphology and composition of spray-flame-made yttria-stabilized zirconia nanoparticles.* Nanotechnology, 2005. 16(7): p. S609-S617.

109. R. Mueller, et al., *Zirconia nanoparticles made in spray flames at high production rates.* J. Am. Ceram. Soc., 2004. 87(2): p. 197-202.

110. R. Mueller, L. Madler, and S.E. Pratsinis, *Nanoparticle synthesis at high production rates by flame spray pyrolysis.* Chem. Eng. Sci., 2003. 58(10): p. 1969-1976.

111. A. Teleki, et al., *Sensing of organic vapors by flame-made TiO_2 nanoparticles.* Sens. Actuators, B, 2006. 119(2): p. 683-690.

112. L. Madler, et al., *Direct formation of highly porous gas-sensing films by in situ thermophoretic deposition of flame-made Pt/SnO_2 nanoparticles.* Sens. Actuators, B, 2006. 114(1): p. 283-295.

113. L. Madler, W.J. Stark, and S.E. Pratsinis, *Flame-made ceria nanoparticles.* J. Mater. Res., 2002. 17(6): p. 1356-1362.

114. M.F. Daniel, et al., *Infrared and Raman study of WO_3 tungsten trioxides and $WO_3.xH_2O$ tungsten trioxide hydrates.* J. Solid State Chem., 1987. 67(2): p. 235-247.

115. B.M. Weckhuysen, I.E. Wachs, and R.A. Schoonheydt, *Surface chemistry and spectroscopy of chromium in inorganic oxides.* Chem. Rev., 1996. 96(8): p. 3327-3349.

116. R.L. Frost, L. Duong, and M. Weier, *Raman microscopy of selected tungstate minerals.* Spectrochim. Acta, Part A, 2004. 60(8-9): p. 1853-1859.

117. J.T. Kloprogge, et al., *Microwave-assisted synthesis and characterisation of divalent metal tungstate nanocrystalline minerals: ferberite, hubnerite, sanmartinite, scheelite and stolzite.* Mater. Chem. Phys., 2004. 88(2-3): p. 438-443.

118. O. Heyer, et al., *A new multiferroic material: $MnWO_4$.* J. Phys.: Condens. Matter, 2006. 18(39): p. L471-L475.

119. W.M. Qu, W. Wlodarski, and J.U. Meyer, *Comparative study on micromorphology and humidity sensitive properties of thin-film and thick-film humidity sensors based on semiconducting $MnWO_4$.* Sens. Actuators, B, 2000. 64(1-3): p. 76-82.

120. I. Jimenez, et al., *NH_3 interaction with chromium-doped WO_3 nanocrystalline powders for gas sensing applications.* J. Mater. Chem., 2004. 14(15): p. 2412-2420.

121. S. Vemury and S.E. Pratsinis, *Dopants in flame synthesis of titania.* J. Am. Ceram. Soc., 1995. 78(11): p. 2984-2992.

122. S.V. Ryabtsev, et al., *Application of semiconductor gas sensors for medical diagnostics.* Sens. Actuators, B, 1999. 59(1): p. 26-29.

123. X.L. Li, et al., *Highly sensitive WO_3 hollow-sphere gas sensors.* Inorg. Chem., 2004. 43(17): p. 5442-5449.

124. B.L. Zhu, et al., *Improvement in gas sensitivity of ZnO thick film to volatile organic compounds (VOCs) by adding TiO_2.* Mater. Lett., 2004. 58(5): p. 624-629.

125. R.S. Khadayate, V. Sali, and P.P. Patil, *Acetone vapor sensing properties of screen printed WO_3 thick films.* Talanta, 2007. 72(3): p. 1077-1081.

126. R. Rella, et al., *Acetone and ethanol solid-state gas sensors based on TiO_2 nanoparticles thin film deposited by matrix assisted pulsed laser evaporation.* Sens. Actuators, B, 2007. 127(2): p. 426-431.

127. A. Vorniero, et al., *In_2O_3 nanowires for gas sensors: morphology and sensing characterisation.* Thin Solid Films, 2007. 515(23): p. 8356-8359.

128. Z. Guo, et al., *Template synthesis, organic gas-sensing and optical properties of hollow and porous In_2O_3 nanospheres.* Nanotechnology, 2008. 19(34): p. 9.

129. L.P. Qin, et al., *The template-free synthesis of square-shaped SnO_2 nanowires: the temperature effect and acetone gas sensors.* Nanotechnology, 2008. 19(18): p. 185705.

130. D.M. Griffiths and C.H. Rochester, *Infrared study of adsorption of acetone on rutile.* Journal of the Chemical Society-Faraday Transactions I, 1978. 74: p. 403-417.

131. M. El-Maazawi, et al., *Adsorption and photocatalytic oxidation of acetone on TiO_2: An in situ transmission FT-IR study.* J. Catal., 2000. 191(1): p. 138-146.

132. W.S. Sim and D.A. King, *Mechanism of acetone oxidation on Ag{111}-p(4x4)-O.* Journal of Physical Chemistry, 1996. 100(35): p. 14794-14802.

133. Y. Yun, et al., *Effect of ferroelectric poling on the adsorption of 2-propanol on $LiNbO_3$(0001).* J. Phys. Chem. C, 2007. 111(37): p. 13951-13956.

134. E. Ramos-Moore, J.A. Baier-Saip, and A.L. Cabrera, *Desorption of carbon dioxide from small potassium niobate particles induced by the particles' ferroelectric transition.* Surf. Sci., 2006. 600(17): p. 3472-3476.

135. Y. Inoue and Y. Watanabe, *Use of $LiNbO_3$ for design of device-type catalysts with activity controllable function.* Catal. Today, 1993. 16(3-4): p. 487-494.

136. I.M. Szilagyi, et al., *In situ HT-XRD study on the formation of hexagonal ammonium tungsten bronze by partial reduction of ammonium paratungstate tetrahydrate.* Eur. J. Inorg. Chem., 2006(17): p. 3413-3418.

137. H. Arai and H. Tominaga, *Infrared study of nitric-oxide adsorbed on rhodium-alumina catalyst.* J. Catal., 1976. 43(1-3): p. 131-142.

138. S.H. Wang, T.C. Chou, and C.C. Liu, *Nano-crystalline tungsten oxide NO_2 sensor.* Sens. Actuators, B, 2003. 94(3): p. 343-351.

139. L.G. Teoh, et al., *Sensitivity properties of a novel NO_2 gas sensor based on mesoporous WO_3 thin film.* Sens. Actuators, B, 2003. 96(1-2): p. 219-225.

140. T.D. Sharkey and S. Yeh, *Isoprene emission from plants.* Annu. Rev. Plant Physiol. Plant Mol. Biol., 2001. 52(1): p. 407-436.

141. J. Taucher, et al., *Methanol in human breath.* Alcohol Clin Exp Res,, 1995. 19(5): p. 1147-1150.